

Electrode and Electrolyte Design for High Energy Density Batteries

Jingru Luo

A dissertation
submitted to the Faculty of
the department of Chemistry
in partial fulfillment
of the requirements for the degree of
Doctor of Philosophy

Boston College
Morrissey College of Arts and Sciences
Graduate School

May, 2020

Electrode and Electrolyte Design for High Energy Density Batteries

Jingru Luo

Advisor: Prof. Dunwei Wang

With the fast development of society, the demand for batteries has been increasing dramatically over the years. To satisfy the ever-increasing demand for high energy density, different chemistries were explored. From the first-generation lead–acid batteries to the state-of-the-art LIBs (lithium ion batteries), the energy density has been improved from 40 to over 200 Wh kg⁻¹. However, the development of LIBs has approached the upper limit. Electrode materials based on insertion chemistry generally deliver a low capacity of no more than 400 mAh/g. To break the bottleneck of current battery technologies, new chemistries are needed. Moving from the intercalation chemistry to conversion chemistry is a trend. The conversion electrode materials feature much higher capacity than the conventional intercalation-type materials, especially for the O₂ cathode and Li metal anode. The combination of these two can bring about a ten-folds of energy density increase to the current LIBs. Moreover, to satisfy the safety requirements, either using non-flammable electrolytes to reduce the safety risk of Li metal anode or switch to dendrite-free Mg anode is a good strategy toward high energy density batteries.

First, to enable the conversion-type O₂ cathode, a wood-derived, free-standing porous carbon electrode was demonstrated and successfully be applied as a cathode in Li-O₂ batteries. The spontaneously formed hierarchical porous structure exhibits good performance in facilitating the mass transport and hosting the discharge products of Li₂O₂. Heteroatom (N) doping further improves the catalytic activity of the carbon cathode with lower overpotential and higher capacity.

Next, to solve the irreversible Li plating/stripping and safety issues related with Li metal anode, we introduced O₂ as additives to enable Li metal anode operation in non-flammable triethyl phosphate (TEP) electrolyte. The electrochemically induced chemical reaction between O₂-derived species and TEP solvent molecules facilitated the beneficial SEI components formation and effectively suppressed the TEP decomposition. The promise of safe TEP electrolyte was also demonstrated in Li-O₂ battery and Li-LFP battery.

If we think beyond Li chemistries, Mg anode with dendrite-free property can be a promising candidate to further reduce the safety concerns while remaining the high energy density advantage. Toward the end of this thesis, we developed a thin film metal–organic framework (MOF) for selective Mg²⁺ transport to solve the incompatibility issues between the anode and the cathode chemistry for Mg batteries.

Table of Contents

Table of Contents	i
Acknowledgments	iii
List of publications.....	v
Chapter 1. Introduction.....	1
1.1 Promises and challenges of Li-O₂ batteries.....	2
1.1.1 Challenges with the Li anode	4
1.1.2 Challenges with the electrolyte	5
1.1.3 Challenges with the cathode.....	7
1.2 Toward practical lithium-metal anode.....	10
1.2.1 Anode engineering of the lithium metal batteries	13
1.2.2 Electrolyte design of the lithium metal batteries.....	14
1.3 Mg batteries: High energy density with high safety.....	16
1.3.1 From intercalation cathodes to conversion cathodes	19
1.3.2 Toward electrolyte with wide electrochemical window	20
1.4 References	23
Chapter 2. Wood derived porous carbon electrodes for Li-O₂ batteries.....	27
2.1 Experimental.....	30
2.1.1 Material characterization	31
2.1.2 Electrochemical characterization	31
2.2 Results and discussion.....	32
2.3 Conclusion.....	44
2.4 References	45
Chapter 3. Enabling lithium metal anode in nonflammable phosphate electrolyte	48

3.1	Experimental.....	51
3.1.1	Materials preparation.....	51
3.1.2	Materials characterization	51
3.1.3	Electrochemical characterization	52
3.2	Results and discussion.....	53
3.3	Conclusion.....	68
3.4	References	69
	Chapter 4. Metal-Organic Framework thin film for selective Mg²⁺ transport	71
4.1	Experimental procedures	74
4.2	Results and discussion.....	78
4.3	Conclusion.....	94
4.4	References	94
	Chapter 5. Summary	97

Acknowledgments

My sincere and deepest gratitude goes first to my advisor Prof. Dunwei Wang, for his guidance and constant support throughout my PhD study. His insightful suggestions and great patience guide me through the research difficulties. I really appreciate his timely praise and warm encouragement to me for my every little progress. I learned a lot from him, not only the research skills, but also the scientific thinking. He is always encouraging students to identify critical scientific questions and turn the initial inspiration into a mature design after several rounds of discussion or debate with him. This unique training benefited me in the past five years and will also benefit me in my future life and career.

I would like to acknowledge my committee: Prof. Udayan Mohanty, Prof. Chia-Kuang (Frank) Tsung, and Prof. Matthias Waegele. I would like to thank Prof. Mohanty and Prof. Tsung for their valuable suggestions on my research. The frequent and insightful discussions on our collaborative project have greatly deepened my understanding and broaden my knowledge in chemistry. I would like to thank Prof. Waegele for teaching me *Physical Chemistry*. The fundamental knowledge I gained from the course benefited me a lot during my research studies.

I would like to acknowledge my mentor Dr. Xiahui Yao for instructing me when I stepped into the research journey. His rigorous attitude to research has always inspiring me. I would like to thank Dr. Qi Dong and Dr. Da He for giving me expert research advices. I am also thankful to Haochuan Zhang, Dr. Haoyi Li, Nicholas Wong, Christopher Povinelli and Tongtong Luo, who made enormous contribution to the projects. I would like to convey my special thanks to all my lab mates, who have always been there to help me.

I would like to acknowledge my collaborators: Prof. Fan Wei Prof. Stephanie Wunder and Prof. Hongli Zhu for their generous exchange of ideas and technical support for the projects. Same gratitude goes to my other colleagues: Yang Li and Ailun Wang for their great contribution to the projects.

I would like to acknowledge all the administrative and technical staffs in the Chemistry Department, Physics Department, and the Integrated Sciences Cleanroom and

Nanofabrication Facility of Boston College; also the staffs at the shared facilities in the Center for Nanoscale Systems of Harvard University, and the Center for Material Science and Engineering of MIT.

I express my deep sense of gratitude to my beloved parents for giving me life and raising me into who I am today. I am proud to be your daughter. Especially, I would like to thank my fiancé Yumin He for his love and support. I love you to the moon and back.

Jingru Luo

May 2020

List of publications

1. Haochuan Zhang,[†] Jingru Luo,[†] Miao Qi, Qi Dong, Nicholas Dulock, Christopher Povinelli, Nicholas Wong, Dunwei Wang, “Enabling Lithium Metal Anode in Nonflammable Phosphate Electrolyte with Electrochemically-Induced Chemical Reactions” *in preparation*.
2. Jingru Luo[†], Yang Li[†], Haochuan Zhang, Ailun Wang, Wei-Shang Lo, Qi Dong, Nicholas Wong, Christopher Povinelli, Yucai Shao, Sumanth Chereddy, Stephanie Wunder, Udayan Mohanty, Chia-Kuang Tsung, Dunwei Wang, “Metal-Organic-Framework Thin Film for Selective Mg²⁺ Transport,” *Angew. Chem. Int. Ed.* **2019**, *58*, 15313-15317
3. Steven D. Lacey, Qi Dong, Zhennan Huang, Jingru Luo, Hua Xie, Zhiwei Lin, Vivek Vattipalli, Christopher Povinelli, Wei Fan, Reza Shahbazian-Yassar, Dunwei Wang, Liangbing Hu, “Stable Multimetallic Nanoparticles for Oxygen Electrocatalysis,” *Nano Lett.* **2019**, *19*, 5149
4. Jingru Luo[†], Xiahui Yao[†], Lei Yang[†], Yang Han, Liao Chen, Xiumei Geng, Vivek Vattipalli, Qi Dong, Wei Fan, Hongli Zhu, Dunwei Wang, “Free-Standing Porous Carbon Electrodes Derived from Wood for High-Performance Li-O₂ Battery Applications,” *Nano Res.* **2017**, *12*, 4318-4326
5. Qi Dong, Xiahui Yao, Jingru Luo, Xizi Zhang, Hajin Hwang, Dunwei Wang, “Enabling Rechargeable Non-Aqueous Mg-O₂ Battery Operations with Dual Redox Mediators,” *Chem. Commun.* **2016**, *52*, 13753-13756
6. Xiahui Yao, Jingru Luo, Qi Dong, Dunwei Wang, “A Rechargeable Non-Aqueous Mg-Br₂ Battery,” *Nano Energy* **2016**, *28*, 440-446

Chapter 1. Introduction

Energy storage is an important part of the modern society. Various energy storage systems such as thermal, mechanical and pumped hydropower have created well-organized power supply networks and brought an incredible amount of convenience in our daily lives. However, with the development of the society, the current systems are not efficient enough to manage today's ever-evolving energy grid. Batteries, as fast-growing energy storage technologies with rapid response, low cost, long lifetime and high power advantages, are showing great potential to solve the problem. In the past two centuries, different types of batteries have been commercialized such as lead–acid, nickel–cadmium, nickel–metal hydride and lithium ion batteries (LIBs), etc. Among them, LIBs, are the most promising one for the use of portable devices and even electric vehicles. The LIBs have improved the energy density from 40 Wh kg⁻¹ of the first-generation lead–acid batteries to 240 Wh kg⁻¹ and 640 Wh L⁻¹ in the past 150 years¹. Nevertheless, the fast growth rates of energy densities of LIBs have approached the upper limit in the recent years, with only 7–8% per year². The major limiting factor is the energy densities of electrode materials, typically graphite as anode material (capacity 372mAh g⁻¹) and metal oxide as intercalation cathode materials (capacity < 200 mAh g⁻¹)³.

To satisfy the ever-increasing demand for high energy density batteries, new chemistries and materials are under explored. For the cathode materials, switching from low capacity intercalation cathodes to high capacity conversion cathodes (sulfur and O₂) is an efficient and attractive method. For the anode materials, Li metal is always regarded as

the “Holy Grail” electrode with an ultra-high capacity of 3860 mAh g^{-1} and the lowest negative electrochemical potential of -3.040 V vs the standard hydrogen electrode¹. The combination of the lithium metal anode and conversion cathode can bring about a ten-folds of energy density increase to the current LIBs³.

Besides high energy density, safety is also a pursuit for future battery development. However, there always been compromises between energy and safety, i.e. materials with higher energy density generally features higher safety risk, especially the anode materials for lithium ion/metal batteries. The dendrite formation issue is much more severe when the graphite anode is substituted with the lithium metal, which greatly inhibited the commercialization of the new batteries⁴. To solve the problem, either using non-flammable electrolyte or looking for anode features non-dendritic growth feathers is a feasible method. Mg metal, exactly fits in the gap of this area and features both high energy density and safety advantages, showing promising potentials as the anode material for the next generation battery technologies.

1.1 Promises and challenges of Li-O₂ batteries

With the ever-increasing demand of the energy, replacing the current electrode materials of LIBs with higher energy density ones attracts more and more attention. Numerous prior researches have done on the conversion-type cathode materials, especially on O₂ which features an ultra-high theoretical energy density of $3,505 \text{ Wh kg}^{-1}$ (ten times higher than the LIBs) and also low price since it is highly abundant in the air⁵.

The aprotic Li-O₂ battery is operated based on the reversible formation and decomposition of Li₂O₂. Schematic representation of the aprotic Li-O₂ batteries is shown in **Figure. 1-1**. During the discharge process, O₂ diffuses into the porous electrolyte and get reduced at the cathode surface to O₂²⁻, combining with the Li⁺ (oxidized from lithium metal at the anode side) in liquid electrolyte to form the discharge product: $2\text{Li}^+ + \text{O}_2 + 2\text{e}^- \leftrightarrow \text{Li}_2\text{O}_2$. The reversed process happens during the charge process, when the Li₂O₂ is decomposed at the cathode surface, releasing O₂ and Li⁺ to the electrolyte: $\text{Li}_2\text{O}_2 \leftrightarrow 2\text{Li}^+ + \text{O}_2 + 2\text{e}^-$. Over the past twenty years, researchers have put a lot of effort in enabling practical Li-O₂ batteries. However, it is revealed that the challenges come from all components of the cells, including parasitic reactions happening at anode, electrolyte and cathode. These critical issues have greatly limited the further development of Li-O₂ batteries into commercialization.

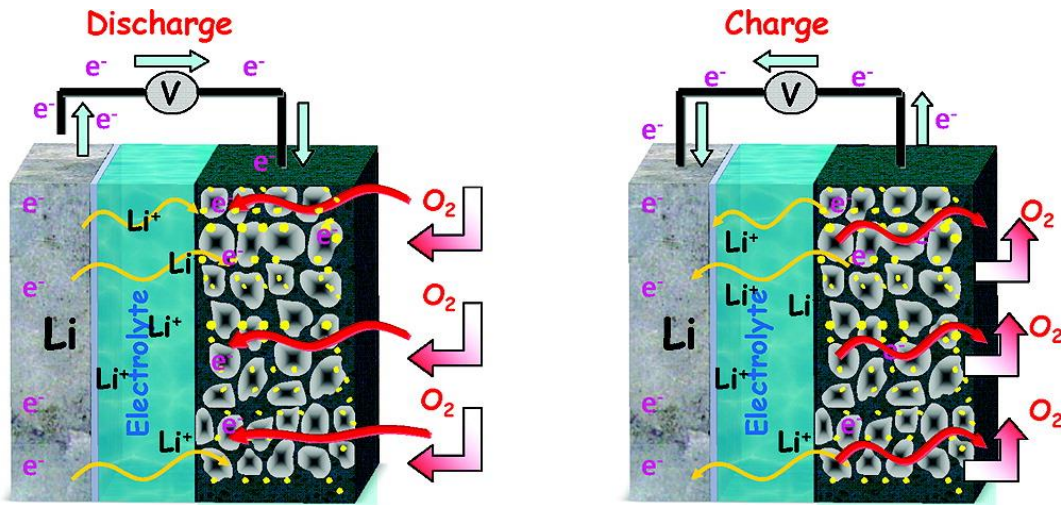


Figure 1-1. Schematic operation of the rechargeable Li-O₂ batteries. Reprinted with permission from Ref [6] . Copyright (2010) American Chemical Society.

1.1.1 Challenges with the Li anode

The anode material commonly used for the Li-O₂ batteries is the lithium metal instead of the graphite. The high capacity Li metal featured (3860 mA h g⁻¹) perfectly matches the high O₂ cathode capacity, so as to fully achieve the battery capacities. However, the use of such high reactive anode with low redox potential can easily lead to side reactions with electrolyte and O₂. Here the interfacial reactions between anode and electrolyte is the key. In the state-of-the-art LIBs, carbonate electrolytes are typically used, with compact solid electrolyte interface (SEI) formed from initial reactions of electrolyte/anode to prohibit further parasitic reaction at the interface and enable long time cycling. Nevertheless, things are quite different when switching to Li metal anode. The SEI formed at the Li/carbonate electrolytes interface is poor, which leads to the continuous parasitic reactions and battery failure eventually. That is the reason why ether based electrolyte such as DME (dimethoxyethane) and TEGDME (tetraethylene glyco dimethyl ether) are usually used in the Li-O₂ batteries for laboratory-level tests because of the high stability against nucleophiles. However, the improvement is limited. The SEI formed on Li surface is still much poorer than that on graphite in LIBs. The overall battery performance is far from practical targets.

Another issue related to the Li anode comes from the parasitic reaction with O₂. As the batteries need to be operated in an O₂ saturated environment, the direct contact between Li and O₂ can easily happen, which leads to redox reactions that produce reduced oxygen species such as superoxide (e.g., O₂⁻). The reactive superoxide species will extract H from the organic electrolyte molecules and attack the Li anode⁷. Generally, the initial reactions

happened at the anode/electrolyte interface tend to be self-limiting so to form a stable SEI. However, in Li-O₂ batteries, the above reactions turn out to be continuous during the repeated battery cycling process due to the poor quality of the SEI layer and also due to the dendritic growth of Li. Previous researches preliminarily proved that the abundant surface LiOH/Li₂O species on Li metal resulted in the anode failures⁸. However, recent years there were different opinions coming out on this topic and new evidence showing the benefited role of O₂ in terms of the Li protection⁹. The detailed failure mechanism of the Li anode in Li-O₂ battery system needs to be further explored.

Besides the parasitic reactions induced by either electrolyte or O₂, there is also intrinsic problem with Li metal anode which is the dendrite formation. The non-uniform deposition of Li during plating brings about safety concerns and could possibly lead to the thermal runaway and even battery explosion. More will be discussed later in Section 1.2.

1.1.2 Challenges with the electrolyte

The commonly used electrolyte in aprotic Li-O₂ batteries are ether-based electrolytes. There are also some reports on DMSO (dimethyl sulfoxide), amide and ionic liquid ones. However, none of these existing electrolyte are stable enough for long-time Li-O₂ battery cycling. The electrolytes decomposition comes from both the cathode side and anode side: 1) The ORR (oxygen reduction reaction) and OER (oxygen evolution reaction) at the cathode will generate reactive oxygen species (e.g., O₂⁻, Li₂O₂, and Li_{2-x}O₂), which will attack the solvent molecules. 2) Solvent continuously decomposed on the Li anode surface. The reactive oxygen species induced electrolyte decomposition can be further divided into four categories: (1) nucleophilic attacks, (2) auto-oxidation, (3) acid–base reactions, (4)

proton-mediated reactions⁷, as shown in **Figure 1-2**. The nucleophilic attacks by $O_2^{\cdot-}$ to the C=O group in carbonate electrolyte were proved to be the major reason for the battery failure in the early studies. Even for ethers and DMSO electrolytes that show better stability against nucleophilic attacks than carbonates, the decomposition still cannot be fully eliminated. The auto-oxidation decomposition usually happens in the ether-based electrolytes. Both $O_2^{\cdot-}$ and O_2 can promote the α -H abstraction of the ether molecules, releasing protons and accelerating the electrolyte decomposition process. The acid-base reactions were proved to happen in the DMSO and $PYR_{14}TFSI$ ionic liquid electrolytes. The α -H in DMSO can be easily deprotonated by superoxides and peroxides. Also, the β -H elimination decomposition pathway was found in $PYR_{14}TFSI$ ionic liquid though the acid-base reactions. The proton-mediated degradation can easily happen when H_2O impurity exists, which acts as the proton source to participate in the electrolyte decomposition through different reactions, accelerating the battery failure process⁷.

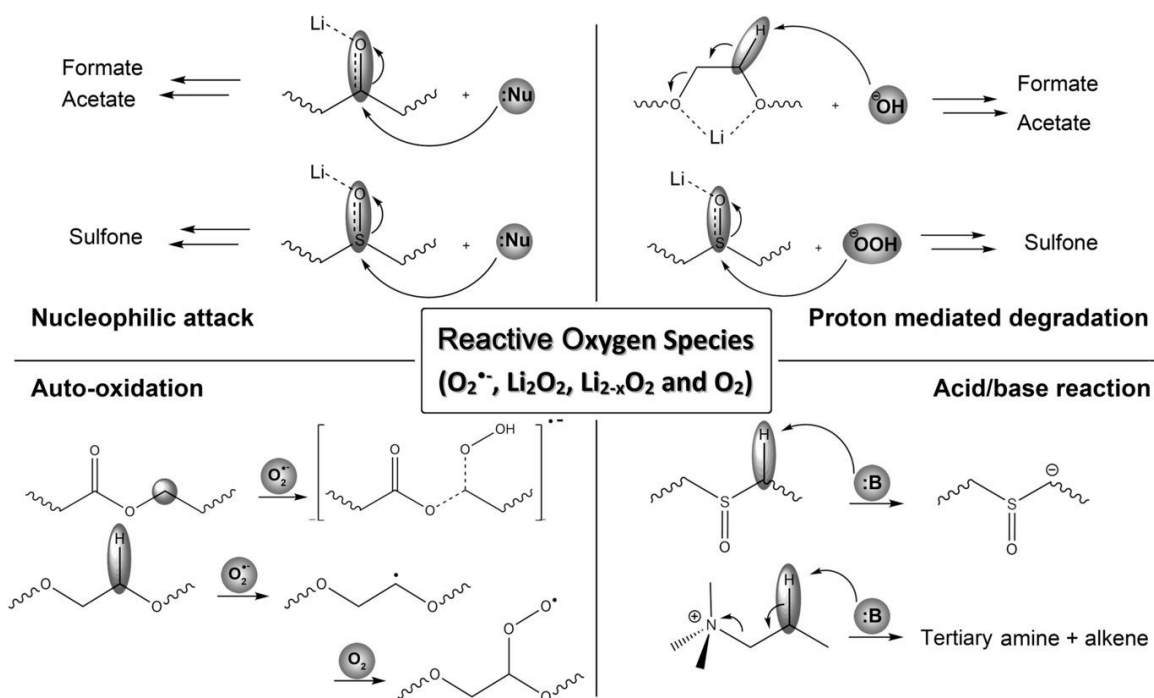


Figure 1-2. Electrolyte decomposition pathways in Li-O₂ batteries. Reprinted with permission from Ref.[7] Copyright (2016) John Wiley and Sons.

The poor SEI generated on Li anode surface will lead to continuous electrolyte decomposition. Li metal shows a highly reductive property with an extremely low redox potential (−3.040 V versus standard hydrogen electrode). Most of the solvent/salt molecules will be easily reduced on the Li surface, forming byproduct such as Li₂O, Li₂CO₃ and some organic species. For a good SEI, the compact byproducts covered on anode functions as a protective layer to inhibit the further decomposition of the electrolyte and enables stable anode operation during battery cycling. However, as Li metal itself is not a proven anode, cracks generate on the SEI during the Li plating/stripping process. Electrolyte will continuously react with Li to form large amount of byproduct, which not only increases the internal resistance but also promotes the degradation of electrolytes. The anode and SEI engineering is crucial to solve the problem. This part will be discussed later in Section 1.2.

1.1.3 Challenges with the cathode

Among all the challenges influencing the performance of a Li-O₂ battery, cathode problems are always regarded as the most critical ones, at least for the current stage of the Li-O₂ battery development. Key challenges with the cathode include: 1) The poor stability of cathode materials towards the reactive oxygen species (e.g., O₂^{•−}, Li₂O₂, and Li_{2-x}O₂) generated during cycling. 2) Sluggish oxygen reaction kinetics (ORR and OER) at cathode. All those problems will finally result in the low capacity, low round-trip efficiency, and quick degradation of the battery performance.

Carbon is the most widely used material as cathode for aprotic Li-O₂ batteries due to the low cost and high conductivity¹⁰. More importantly, the various porous structures of different carbon materials provide abundant templates for cathode engineering, including surface area improvement and microstructural optimization. Ideally, the physical integrity and chemical stability of carbon cathode should be maintained during the ORR/OER cathode chemistries. However, the degradation of carbon cathode was found to be a common phenomenon in the previous researches, finally leading to the poor cycling performance of Li-O₂ batteries¹¹. The evolution of reaction products (including the volume expansion upon Li₂O₂ deposition in discharge and O₂ gas releasing in charge) during cycling can lead to structural destruction of the carbon¹¹. Moreover, the oxidation of carbon towards the reactive oxygen species generated undesirable products such as Li₂CO₃. The gradually increased passivation layer during cycling will increase the over-potential for Li₂O₂ deposition and decomposition, eventually results in low energy efficiency, low round-trip efficiency and quick degradation of battery performance¹².

Besides the physical and chemical stability issue related with the porous carbon material, its poor catalytic activity towards OER and ORR is also problematic. The sluggish kinetic will greatly increase the over-potential of Li₂O₂ decomposition during the charge process. The high voltage (when charging above 3.5 V vs. Li⁺/Li) can accelerate the carbon and electrolyte decomposition in the presence of active oxygen species (see **Figure 1-3**). As a result, more Li₂CO₃ will be generate on the cathode surface during cycling, which further slows down the kinetics and pushes up the over-potential¹². The byproduct accumulation is regarded as the major failure reason for the Li-O₂ batteries at current stage.

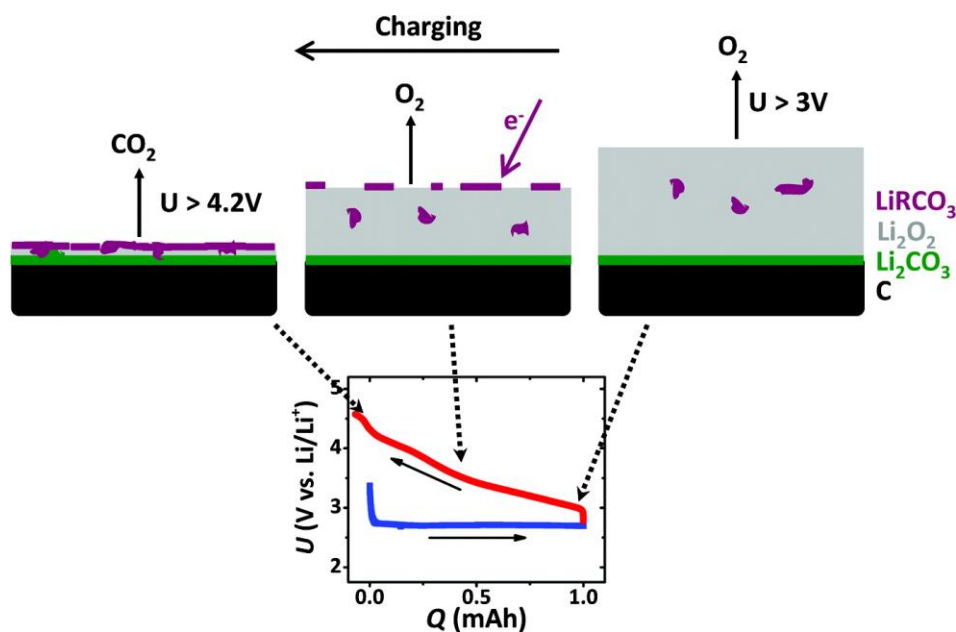


Figure 1-3. Schematic illustrations of the byproduct deposition and over potential increase during Li-O₂ battery charge process. Reprinted with permission from Ref.[12] Copyright (2012) American Chemical Society.

Tremendous efforts have been put into this area to solve the cathode problems. To strengthen the mechanical stability of the porous carbon, carbon materials with higher mechanical stability were explored. For example, the ordered mesoporous carbon nanofiber arrays were proved to be an efficient cathode material by providing sufficient macro sized void spaces to buffer the volume change during the Li₂O₂/O₂ conversion chemistries¹³. Surface protection layer such as FeO_x was also applied to isolate the carbon cathode from peroxide and superoxide species, improving its chemical stability towards oxidation¹⁴. These cathode stability enhancement strategies always went along with the catalyst design to solve the problem of sluggish oxygen reaction kinetics at cathode. So far, various catalysts have been proven to be effective to promote the cathode chemistries and lower the over potential. Noble metals such as Pt, Pd, Ru and Ir have been widely used in the Li-O₂ batteries to enhance the catalytic activity. For example, a Ru-rich multimetallic

catalytic systems was applied on the carbon cathode, showing much lower overpotential and prolonged cycle life for Li-O₂ battery demonstration¹⁵. Other catalysts such as Co₃O₄, MnO₂, and nitrogen various doped carbons were also explored as good catalysts to promote the cathode chemistries¹⁶.

Though various strategies have demonstrated the possibility of solving the challenges of carbon cathode, it is still far away from achieving practical usage. Even with OER/ORR catalyst decorations, the cathode surface is always dominated by carbon due to its much higher surface area than that of the catalyst¹¹. The parasitic reactions and byproduct accumulation still happen. One way to solve the intrinsic problem induced by carbon is to substitute it with the non-carbon materials. For example, TiSi₂ nanonet was reported as a high surface area, conductive material suitable as the new cathode support. Moreover, compared with the widely used carbon support, the TiSi₂ nanonet is advantageous in that it does not show measurable reactivity toward reaction intermediates such as superoxide ions. Combining with the catalyst modification with Ru nanoparticles, the new cathode system Ru-nanoparticles-decorated TiSi₂ nanonet showed a superior cyclability of more than 100 cycles in Li-O₂ batteries¹⁷.

1.2 Toward practical lithium-metal anode

As the LIBs is reaching their limit because of the low capacities of electrode materials, Li metal anode, with highest theoretical specific capacity (3860 mAh g⁻¹) and low potential (-3.04 V vs. the standard hydrogen electrode) has become a promising candidate for the

next-generation battery design. Actually, early in the 1970s, primary LMBs was employed in cardiac pacemakers and successfully extended the battery life to ten years¹⁸. However, to achieve broader applications for energy storage as well as more cost-effective and environmentally friendly, secondary batteries, i.e. rechargeable batteries are needed. Nevertheless, the commercializing of lithium metal batteries (LMBs) has been greatly hindered by the irreversible plating/stripping and severe safety issues with the lithium metal anode¹, as shown in **Figure 1-4**. Due to the extremely high reactivity of lithium metal, the electrolyte decomposition will be spontaneously happened on the Li surface, forming a SEI layer. Ideally, the SEI will function as a protection layer to avoid the direct contact between Li and electrolyte for a stable cycling of the battery, similar to where in LIBs. However, different from the intercalation-type graphite anode with a small volume change of ~10%¹⁹, the “hostless” nature of Li anode brings about an infinite volume change during cycling. The SEI on Li surface can hardly remain crack-free during the cycling with huge volume change. Continuous reaction between newly exposed Li metal and the electrolyte will lead to battery failure either from electrolyte/Li depletion or the accumulation of dead lithium²⁰. The safety concerns mainly come from the dendrite formation. Under electrochemical condition during the charge process, Li tends to deposit as a sharp, dendritic form rather than smooth and uniform ones, which could lead to the short-circuit and even explosion of the LMBs batteries.

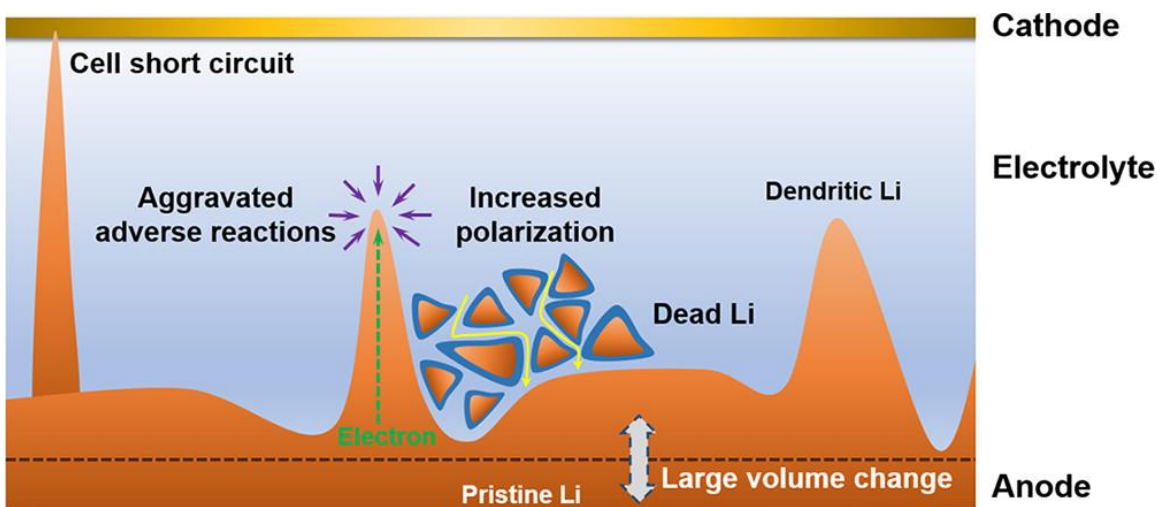


Figure 1-4. Schematic of Li metal anode failure mechanisms in rechargeable batteries.

Reprinted with permission from Ref.[1] Copyright (2017) American Chemical Society.

Although the origin of Li dendrite is not fully understood yet, a variety of mechanisms have been proposed. For the initial nucleation of Li plating, the most well-accepted theory is the space-charge model, which was proposed by Chazalviel in 1990s²¹. Under a high current density, the anion concentration near the electrode surface drops to zero in a dilute solution. The anion depletion creates a large space charge and electric field, leading to ramified growth of Li. The tip-induced nucleation theory further explained the self-enhancing feature of the dendrite growth²². The local electric field at the tips of the protuberances is larger than that around the smooth part. The gathered Li^+ will facilitate the growth of Li metal at the tips, thus resulting in inhomogeneous deposition and formation of mossy/dendritic Li²². . There are generally two directions for the Li metal anode stabilization: dendrite suppression and volume change minimization.

1.2.1 Anode engineering of the lithium metal batteries

To solve the dendrite problem, more robust SEIs were designed on Li anode surface prior to the battery cycling. The “artificial SEI” generally features high mechanical stability to suppress the dendrite growth underneath. For example, a uniform Li_3PO_4 protection layer coated on Li was demonstrated to be effective for restraining Li dendrite growth and reducing the interfacial parasitic reactions. The high chemical and mechanical stability of Li_3PO_4 ensured its functionality as a good SEI for long-time bulk Li cycling for over 200 cycles²³. Other coating materials such as Al_2O_3 ²⁴, LiF ²⁵ and organic polymers for example PDMS (poly(dimethylsiloxane))²⁶ were also used as the artificial SEI for Li anode. Besides the physical protection layer, researchers also tried the chemically pretreatment for Li anode before usage. For instance, Yi Cui *et al.* fabricated a robust pinhole-free- Li_3N artificial SEI layer on Li metal surface through the reaction between clean molten lithium foil and pure nitrogen gas. The pre-coating of Li_3N with high chemical and mechanical stability can efficiently restrain the dendrite growth and suppress the interfacial resistance induced by Li/electrolyte reactions²⁷.

To address the volume change issue, two approaches were proposed. One is to use very thin Li with a thickness less than 20 μm . The second approach is to develop a stable and conductive Li host that can be used to minimize the volume changes or ‘swelling/shrinking’ of Li during cycling, and effectively reduce the local current density²⁸. Following the guidance, different host materials have been introduced to solve the problem. Pre-storing Li into the anode host can not only reduce the volume change, but also maintain the high-energy-density advantage. For example, layered rGO (reduced-graphene oxide) was proved to be a stable host for Li with good lithium affinity. Good lithiophilicity ensures

the strong binding between Li and the materials' surface, which is critical for achieving both uniform molten Li infusion low Li nucleation barrier in battery cycling. With a pre-designed rGO interlayer space confinement, the Li-rGO composite anode successfully achieved a small electrode dimensional change ($\sim 20\%$) during cycling with stable SEI²⁹. Other than carbon host materials, metals (Cu, Ni, etc.) are also demonstrated to be functional Li hosts. Zhang et al. designed a Li-Ni composite anode by infusing molten Li into a metallic Ni foam host. The well-confined Li enabled the low electrode dimension change and dendrite-free deposition³⁰.

1.2.2 Electrolyte design of the lithium metal batteries

Electrolyte components have been proven to influence the Li metal anode stability in two ways: 1) Affect the Li^+ flux distribution and Li metal deposition on electrode. 2) Affect the SEI properties, including uniformity, compositions and morphology.

To avoid dendrite formation, various additives were applied to the electrolyte to rearrange the Li plating. For example, Cs^+ was introduced to the carbonate electrolyte and successfully changed the morphology of the deposited Li from needle-like dendrites to mirror-like films. According to the tip-induced dendrite growth model, Li tends to be deposited around the tips rather than on smooth regions of the anode due to the stronger electrical field. However, the adsorbed additive cations with a reduction potential lower than Li^+ will accumulate around the tip to form an electrostatic shield. This positively charged shield will repel incoming Li^+ while forcing Li^+ deposition to adjacent regions of the anode until a smooth deposition layer is formed³¹. Zhou *et. al* also demonstrated the utilization of MOF (metal-organic framework) modified electrolyte in regulating the Li^+

deposition. The microporous MOF skeletons can restrict the TFSI⁻ ((bis)trifluoromethanesulfonylimide) anion transport to achieve a homogeneous Li⁺ flux near the electrode surface, avoiding the local inhomogeneities of Li deposition³².

The reason why the electrolyte components can help stabilize Li metal through tuning SEI can be explained from two aspects: 1) Artificial SEI with better mechanical and chemical stability has been proved to be a good strategy to suppress the dendrite growth. Different from the ex-situ formed artificial SEI as described in Section 1.2.1, the SEI induced by electrolyte engineering are usually in-situ formed, which brings convenience to the industrial manufacturing of batteries. The presence of additives can either generate inorganic-rich SEI with high mechanical strength or polymeric outer layer with high flexibility or both which are beneficial to the uniform Li deposition³³. 2) The heterogeneity of the SEI on Li is believed to be one of the reasons for the uneven Li deposition. The native SEI on Li without any special modification generally consists of multicomponent inorganic (including oxide, carbonate, fluoride) and organic phases formed by parasitic reactions between Li and the electrolyte³³. The inhomogeneous current density distribution can lead to inhomogeneous lithium metal crystal nucleation and growth³⁴. Although there are still debates on this topic, evidences have shown the distribution of SEI components indeed have a significant influence on the SEI functions. Mono-component SEI design can be a potential strategy to enable the long-time Li anode operation.

Among all the SEI inorganic components, LiF has always be regarded as the most beneficial one because of the high mechanical strength, low solubility, wide electrochemical window and low Li diffusion barrier. A number of studies have been focused on building a LiF-rich SEI by electrolyte engineering. For example, Zhang *et al.*

reported the fluoroethylene carbonate (FEC) additives in carbonate electrolytes can form a LiF-rich SEI on the surface of Li metal, obtaining a uniform morphology of Li deposits³⁵. In recent years, people also found the high salt concentration electrolytes play an important role in affecting the SEI composition. In a traditional dilute electrolyte (~1M), all salts are well dissolved and solvated to form solvent-separated ion pairs. The SEI layers are formed from solvent reduction, i.e. the solvent-derived SEI and the components of SEI film are mainly derived from the decomposition products of solvents in electrolytes. When the salt concentration increases, cations and anions/solvents will be stronger and the content of free-state solvent molecules will decrease. As a result, anions are predominantly reduced and decomposed to form a salt-derived SEI³⁶. Recently, lithium bis(fluorosulfonyl)imide (LiFSI) and LiTFSI have been explored for high concentration electrolytes. The rigid LiF-rich SEI derived from the anion decompositions can not only provides tight isolation of Li metal from the electrolyte corrosion, but also enables fast Li diffusion for low polarization and uniform Li deposition³⁷.

1.3 Mg batteries: High energy density with high safety

When it comes to the practicability of batteries, safety is always a critical factor. As mentioned in Section 1.2, Li metal anode features great promises in energy density but fails to meet the safety requirements. Strategies such as electrode host/surface engineering and electrolyte modification provide opportunities to reduce the safety risk, but cannot completely rule it out. In this circumstance, Mg anode emerged as a promising candidate

to achieve both high energy density and high safety targets. With the low potential (-2.37 V vs. SHE), high theoretical volumetric capacity (3833 mAh cm^{-3}), high abundance in the earth crust and dendrite-free metal deposition properties, Mg stands out to be a more attractive anode material than Li for the next-generation battery technologies³⁸. Among all the advantages, dendrite-free property is the most important one, which distinguished Mg as an intrinsically safe anode.

The electrochemically deposited Mg metal was first studied in 2011 by Masaki Matsui³⁹. It was found by SEM (scanning electron microscope) that the magnesium deposits did not show a typical dendritic morphology as the Li did. Later *in-situ* imaging studies also support the phenomenon. For instance, Zheng *et al.* observed a uniform, smooth thin film of Mg deposition with no dendritic growth though the *in-situ* TEM (Transmission electron microscopy)⁴⁰. Wan *et al.* also observed the dendrite-free Mg deposition by *in situ* AFM (atomic force microscopy)⁴¹. Although the origin of the dendrite-free growth of the electrochemical deposited Mg is still not clear, some hypotheses were proposed based on theoretical calculations. For example, Matsui *et al.* reported a DFT (Density Functional Theory) study on the electrochemical deposition process of Mg, they found the free energy difference between crystals with different shapes was more significant for Mg than for Li due to the stronger bonding between Mg atoms. So the electrochemical deposition of Mg was more preferable to form high dimensional morphologies instead of 1D dendrite⁴². Jäckle *et al.* also reported that Mg exhibits low diffusion barriers and favors high-coordinated configurations. These properties might contribute to the dendrite-free growth⁴³.

The future of Mg anode is bright, but the reality is struggling. Mg batteries are still facing many challenges at current stage, as shown in **Figure 1-5**. The sluggish Mg^{2+} transport through solids induces challenges to different part of the battery system: 1) The high charge density of divalent Mg^{2+} induces strong interactions between Mg^{2+} and the host material. The slow kinetics of the Mg^{2+} intercalation and de-intercalated greatly hindered the utilization of intercalation-type cathode materials. 2) Sluggish Mg^{2+} transport through the passivation layer on Mg anode surface. Due to the low redox potential of anode materials, the spontaneous electrolyte decomposition on the anode is difficult to completely avoid. In LIBs, the surface passivation layer, i.e. SEI layer serves as a physical barrier to protect the anode from further reacting with electrolyte but still enables fast Li^+ transport. However, due to the high charge density, Mg^{2+} cannot be transported through the surface layer formed from electrolyte decomposition. This is the major reason why Mg anode fails in the conventional carbonate electrolytes. 3) Sluggish Mg^{2+} transport through solids also creates huge difficulties in the solid state electrolyte development. The extreme low ionic conductivity ($< 10^{-8}$ S/cm) of Mg^{2+} in the inorganic materials cannot support the practical battery operation. To solve the above issues and enable practical Mg batteries, new materials were explored for both cathodes and electrolytes.

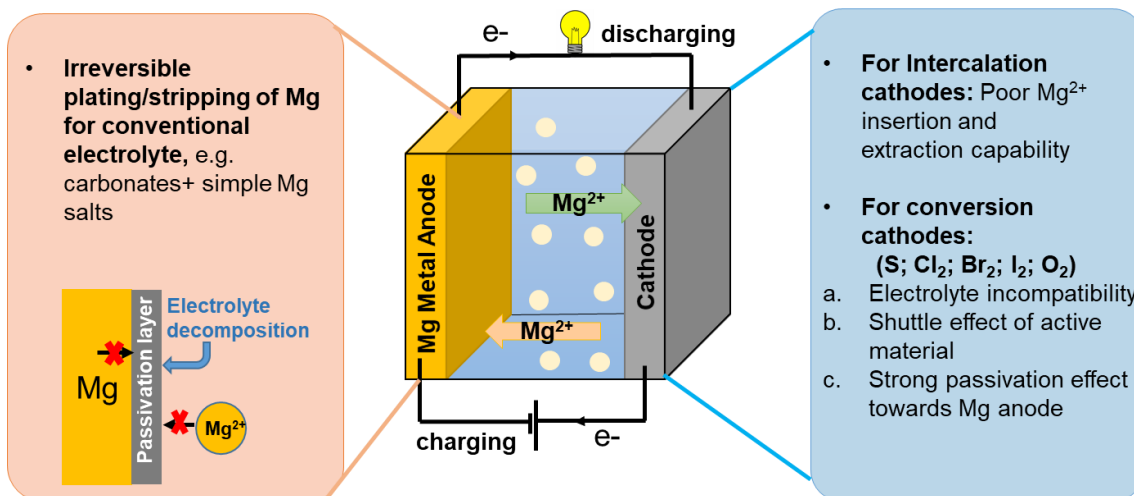


Figure 1-5. Schematic illustration of key challenges of Mg batteries.

1.3.1 From intercalation cathodes to conversion cathodes

Over the past twenty years, tremendous work has been devoted to the discovery of intercalation cathodes for reversible Mg²⁺ intercalation/de-intercalation. Chevrel-Mo₆S₈ was proved to be the most promising one. However, the low energy density of Mo₆S₈ (77 Wh/kg or 400Wh/l) really hindered its practical application⁴⁴. To achieve higher energy density, conversion-type electrodes became alternative candidates. In addition, since the conversion cathodes are operated based on direct redox reactions instead of intercalation chemistry, which could potentially enable fast cathode kinetics. Pioneering work on the conversion cathode for Mg batteries have been demonstrated in recent years, such as Mg-Br₂⁴⁵, Mg-O₂⁴⁶, Mg-I₂⁴⁷ and Mg-S⁴⁸. However, the cathode engineering or structure design is often not the key issue at the current stage. As the surface passivation issue creates great challenges to electrolyte choice, the first and most critical step to enable the conversion

cathode is to find a suitable electrolyte with wide electrochemical window and stable to both the oxidation-vulnerable Mg anode and reduction-vulnerable conversion cathodes.

1.3.2 Toward electrolyte with wide electrochemical window

Due to the severe passivation problem of Mg, conventional electrolyte with high anodic stability ($> 4.0\text{V}$ vs. Mg^{2+}/Mg) cannot be used. New electrolyte development is a crucial step for Mg batteries. Both the solvent and the salt need to be carefully evaluated as either of them can strongly passivate the Mg surface if not chosen appropriately. Grignard reagent (RMgX , where R is an alkyl or aryl group, and X is Cl or Br) was first chosen to be a promising salt for reversible Mg anode operation because of the high cathodic stability⁴⁹. However, it cannot be directly used in batteries either because of the strong reductive property.

To extend the anodic stability of Grignard reagents, Aurbach *et al.* developed the first generation Mg battery electrolyte system in 2000 by dissolving $\text{Mg}(\text{AlCl}_2\text{BuEt})_2$ in THF (Tetrahydrofuran) solvent. The new electrolyte successfully achieved a near 100% efficiency reversibility for Mg plating/stripping⁴⁹. More importantly, the solutions showed an electrochemical window of ca. 2.5V vs. Mg^{2+}/Mg , capable of supporting cathode materials with low voltage. Later, the APC (all phenyl complex) electrolyte was developed by mixing AlCl_3 with PhMgCl in THF, which greatly extended the electrolyte anodic stability up to 3.2V vs. Mg^{2+}/Mg ⁵⁰. This is also the most widely used electrolyte system for Mg batteries up to date. However, the applications of APC electrolytes are only limited to intercalation cathodes. The nucleophilic salts are not compatible with the highly oxidative conversion cathodes such as S, Br_2 or O_2 .

On the way to non-nucleophilic electrolyte for Mg batteries, various new salt or salt-combinations were explored. For example, HMDSMgCl (hexamethyldisilazide magnesium chloride) with AlCl₃ in THF was synthesized by Muldoon *et al.* The non-nucleophilic electrolyte resulted in a dramatic improvement in the anodic stability of ca. 3.2V vs. Mg²⁺/Mg and was proven to be chemically compatible with the electrophilic S cathode⁵¹. Other non-nucleophilic electrolyte such as MACC (Magnesium Aluminum Chloride Complex)⁵², Mg(TFSI)₂/MgCl₂/DME electrolytes⁴⁸ were also explored for conversion cathodes. However, the electrochemical window of current electrolyte systems is still far from satisfying. The ethereal solvents based electrolytes generally provide an anodic stability of < 3.5V vs. Mg²⁺/Mg, which is not enough for practical conversion cathode operation owing to the kinetic overpotential requirements. In response to this challenge, Xia *et al.* proposed a new strategy to separate electrolytes for the anode and cathode in Mg-Br₂ batteries (see **Figure 1-6**)⁴⁵. At the cathode side, ionic liquid with high anodic stability (> 3.7V vs. Mg²⁺/Mg) was used for B₂ cathode. At the anode side, ethereal electrolyte was used to enable reversible stripping and plating of Mg. A porous glass frit was used in between to separate the catholyte and anolyte. Together, this strategy achieved stable Mg-Br₂ battery operation for > 20 cycles⁴⁵.

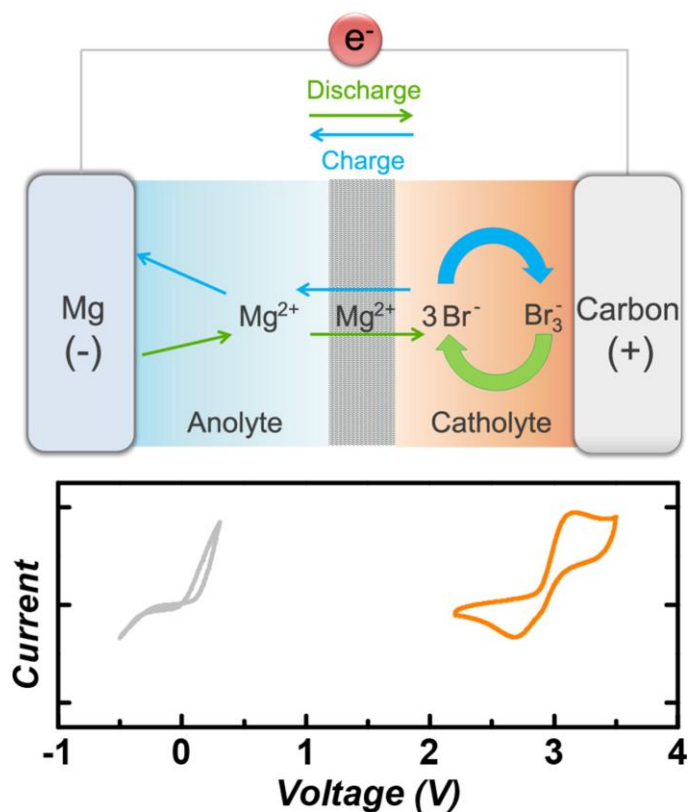


Figure 1-6. Design principle of the Mg-Br₂ battery. Reprinted with permission from Ref.[45] Copyright (2016) Elsevier Ltd.

Ban *et al.* demonstrated another strategy to broaden the electrochemical window of electrolytes by using an artificial interphase for Mg protection. The artificial interphase was formed from a Mg²⁺-conducting polymeric film consisting thermal-cyclized polyacrylonitrile and Mg(CF₃SO₃)₂ (Mg trifluoromethanesulfonate). The strategy rescued the “Mg incompatible” high-voltage carbonate electrolytes for reversible Mg plating/stripping⁵³.

1.4 References

- (1) Cheng, X.-B.; Zhang, R.; Zhao, C.-Z.; Zhang, Q. Toward Safe Lithium Metal Anode in Rechargeable Batteries: A Review. *Chem. Rev.* **2017**, *117* (15), 10403–10473.
- (2) Luntz, A. C.; Voss, J.; Reuter, K. Interfacial Challenges in Solid-State Li Ion Batteries. *J. Phys. Chem. Lett.* **2015**, *6* (22), 4599–4604.
- (3) Manthiram, A. An Outlook on Lithium Ion Battery Technology. *ACS Cent. Sci.* **2017**, *3* (10), 1063–1069.
- (4) Lin, D.; Liu, Y.; Cui, Y. Reviving the Lithium Metal Anode for High-Energy Batteries. *Nat. Nanotechnol.* **2017**, *12* (3), 194–206.
- (5) Imanishi, N.; Yamamoto, O. Perspectives and Challenges of Rechargeable Lithium–Air Batteries. *Mater. Today Adv.* **2019**, *4*, 100031.
- (6) Girishkumar, G.; McCloskey, B.; Luntz, A. C.; Swanson, S.; Wilcke, W. Lithium–Air Battery: Promise and Challenges. *J. Phys. Chem. Lett.* **2010**, *1* (14), 2193–2203.
- (7) Yao, X.; Dong, Q.; Cheng, Q.; Wang, D. Why Do Lithium–Oxygen Batteries Fail: Parasitic Chemical Reactions and Their Synergistic Effect. *Angew. Chem. Int. Ed.* **2016**, *55* (38), 11344–11353.
- (8) Lu, J.; Jung Lee, Y.; Luo, X.; Chun Lau, K.; Asadi, M.; Wang, H.-H.; Brombosz, S.; Wen, J.; Zhai, D.; Chen, Z.; Miller, D. J.; Sub Jeong, Y.; Park, J.-B.; Zak Fang, Z.; Kumar, B.; Salehi-Khojin, A.; Sun, Y.-K.; Curtiss, L. A.; Amine, K. A Lithium–Oxygen Battery Based on Lithium Superoxide. *Nature* **2016**, *529* (7586), 377–382.
- (9) Qiu, F.; Zhang, X.; Qiao, Y.; Zhang, X.; Deng, H.; Shi, T.; He, P.; Zhou, H. An Ultra-Stable and Enhanced Reversibility Lithium Metal Anode with a Sufficient O₂ Design for Li–O₂ Battery. *Energy Storage Mater.* **2018**, *12*, 176–182.
- (10) Pandolfo, A. G.; Hollenkamp, A. F. Carbon Properties and Their Role in Supercapacitors. *J. Power Sources* **2006**, *157* (1), 11–27.
- (11) Chang, Z.; Xu, J.; Liu, Q.; Li, L.; Zhang, X. Recent Progress on Stability Enhancement for Cathode in Rechargeable Non-Aqueous Lithium–Oxygen Battery. *Adv. Energy Mater.* **2015**, *5* (21), 1500633.
- (12) McCloskey, B. D.; Speidel, A.; Scheffler, R.; Miller, D. C.; Viswanathan, V.; Hummelshøj, J. S.; Nørskov, J. K.; Luntz, A. C. Twin Problems of Interfacial Carbonate Formation in Nonaqueous Li–O₂ Batteries. *J. Phys. Chem. Lett.* **2012**, *3* (8), 997–1001.
- (13) Guo, Z.; Zhou, D.; Liu, H.; Dong, X.; Yuan, S.; Yu, A.; Wang, Y.; Xia, Y. Synthesis of Ruthenium Oxide Coated Ordered Mesoporous Carbon Nanofiber Arrays as a Catalyst for Lithium Oxygen Battery. *J. Power Sources* **2015**, *276*, 181–188.
- (14) Xie, J.; Yao, X.; Cheng, Q.; Madden, I. P.; Dornath, P.; Chang, C.-C.; Fan, W.; Wang, D. Three Dimensionally Ordered Mesoporous Carbon as a Stable, High-Performance Li–O₂ Battery Cathode. *Angew. Chem. Int. Ed.* **2015**, *54* (14), 4299–4303..
- (15) Lacey, S. D.; Dong, Q.; Huang, Z.; Luo, J.; Xie, H.; Lin, Z.; Kirsch, D. J.; Vattipalli, V.; Povinelli, C.; Fan, W.; Shahbazian-Yassar, R.; Wang, D.; Hu, L. Stable Multimetallic Nanoparticles for Oxygen Electrocatalysis. *Nano Lett.* **2019**, *19* (8), 5149–5158.

- (16) Eftekhari, A.; Ramanujam, B. In Pursuit of Catalytic Cathodes for Lithium–Oxygen Batteries. *J. Mater. Chem. A* **2017**, *5* (17), 7710–7731.
- (17) Xie, J.; Yao, X.; Madden, I. P.; Jiang, D.-E.; Chou, L.-Y.; Tsung, C.-K.; Wang, D. Selective Deposition of Ru Nanoparticles on TiSi₂ Nanonet and Its Utilization for Li₂O₂ Formation and Decomposition. *J. Am. Chem. Soc.* **2014**, *136* (25), 8903–8906.
- (18) Mallela, V. S.; Ilankumaran, V.; Rao, N. S. Trends in Cardiac Pacemaker Batteries. *Indian Pacing Electrophysiol. J.* **2004**, *4* (4), 201–212.
- (19) Qi, Y.; Guo, H.; Jr, L. G. H.; Timmons, A. Threefold Increase in the Young’s Modulus of Graphite Negative Electrode during Lithium Intercalation. *J. Electrochem. Soc.* **2010**, *157* (5), A558.
- (20) Wang, H.; Liu, Y.; Li, Y.; Cui, Y. Lithium Metal Anode Materials Design: Interphase and Host. *Electrochem. Energy Rev.* **2019**, *2* (4), 509–517.
- (21) Chazalviel, J.-N. Electrochemical Aspects of the Generation of Ramified Metallic Electrodeposits. *Phys. Rev. A* **1990**, *42* (12), 7355–7367.
- (22) Wang, A.; Deng, Q.; Deng, L.; Guan, X.; Luo, J. Eliminating Tip Dendrite Growth by Lorentz Force for Stable Lithium Metal Anodes. *Adv. Funct. Mater.* **2019**, *29* (25), 1902630.
- (23) Li, N.-W.; Yin, Y.-X.; Yang, C.-P.; Guo, Y.-G. An Artificial Solid Electrolyte Interphase Layer for Stable Lithium Metal Anodes. *Adv. Mater.* **2016**, *28* (9), 1853–1858.
- (24) Kozen, A. C.; Lin, C.-F.; Pearse, A. J.; Schroeder, M. A.; Han, X.; Hu, L.; Lee, S.-B.; Rubloff, G. W.; Noked, M. Next-Generation Lithium Metal Anode Engineering via Atomic Layer Deposition. *ACS Nano* **2015**, *9* (6), 5884–5892.
- (25) Fan, L.; Zhuang, H. L.; Gao, L.; Lu, Y.; Archer, L. A. Regulating Li Deposition at Artificial Solid Electrolyte Interphases. *J. Mater. Chem. A* **2017**, *5* (7), 3483–3492.
- (26) Zhu, B.; Jin, Y.; Hu, X.; Zheng, Q.; Zhang, S.; Wang, Q.; Zhu, J. Poly(Dimethylsiloxane) Thin Film as a Stable Interfacial Layer for High-Performance Lithium-Metal Battery Anodes. *Adv. Mater.* **2017**, *29* (2), 1603755.
- (27) Li, Y.; Sun, Y.; Pei, A.; Chen, K.; Vailionis, A.; Li, Y.; Zheng, G.; Sun, J.; Cui, Y. Robust Pinhole-Free Li₃N Solid Electrolyte Grown from Molten Lithium. *ACS Cent. Sci.* **2018**, *4* (1), 97–104.
- (28) Liu, J.; Bao, Z.; Cui, Y.; Dufek, E. J.; Goodenough, J. B.; Khalifah, P.; Li, Q.; Liaw, B. Y.; Liu, P.; Manthiram, A.; Meng, Y. S.; Subramanian, V. R.; Toney, M. F.; Viswanathan, V. V.; Whittingham, M. S.; Xiao, J.; Xu, W.; Yang, J.; Yang, X.-Q.; Zhang, J.-G. Pathways for Practical High-Energy Long-Cycling Lithium Metal Batteries. *Nat. Energy* **2019**, *4* (3), 180–186.
- (29) Lin, D.; Liu, Y.; Liang, Z.; Lee, H.-W.; Sun, J.; Wang, H.; Yan, K.; Xie, J.; Cui, Y. Layered Reduced Graphene Oxide with Nanoscale Interlayer Gaps as a Stable Host for Lithium Metal Anodes. *Nat. Nanotechnol.* **2016**, *11* (7), 626–632.
- (30) Chi, S.-S.; Liu, Y.; Song, W.-L.; Fan, L.-Z.; Zhang, Q. Prestoring Lithium into Stable 3D Nickel Foam Host as Dendrite-Free Lithium Metal Anode. *Adv. Funct. Mater.* **2017**, *27* (24), 1700348.
- (31) Ding, F.; Xu, W.; Graff, G. L.; Zhang, J.; Sushko, M. L.; Chen, X.; Shao, Y.; Engelhard, M. H.; Nie, Z.; Xiao, J.; Liu, X.; Sushko, P. V.; Liu, J.; Zhang, J.-G. Dendrite-Free Lithium Deposition via Self-Healing Electrostatic Shield Mechanism. *J. Am. Chem. Soc.* **2013**, *135* (11), 4450–4456.

- (32) Bai, S.; Sun, Y.; Yi, J.; He, Y.; Qiao, Y.; Zhou, H. High-Power Li-Metal Anode Enabled by Metal-Organic Framework Modified Electrolyte. *Joule* **2018**, *2* (10), 2117–2132.
- (33) He, M.; Guo, R.; Hobold, G. M.; Gao, H.; Gallant, B. M. The Intrinsic Behavior of Lithium Fluoride in Solid Electrolyte Interphases on Lithium. *Proc. Natl. Acad. Sci.* **2020**, *117* (1), 73–79.
- (34) Li, Q.; Pan, H.; Li, W.; Wang, Y.; Wang, J.; Zheng, J.; Yu, X.; Li, H.; Chen, L. Homogeneous Interface Conductivity for Lithium Dendrite-Free Anode. *ACS Energy Lett.* **2018**, *3* (9), 2259–2266.
- (35) Zhang, X.-Q.; Cheng, X.-B.; Chen, X.; Yan, C.; Zhang, Q. Fluoroethylene Carbonate Additives to Render Uniform Li Deposits in Lithium Metal Batteries. *Adv. Funct. Mater.* **2017**, *27* (10), 1605989.
- (36) Yamada, Y.; Wang, J.; Ko, S.; Watanabe, E.; Yamada, A. Advances and Issues in Developing Salt-Concentrated Battery Electrolytes. *Nat. Energy* **2019**, *4* (4), 269–280.
- (37) Wang, M.; Huai, L.; Hu, G.; Yang, S.; Ren, F.; Wang, S.; Zhang, Z.; Chen, Z.; Peng, Z.; Shen, C.; Wang, D. Effect of LiFSI Concentrations To Form Thickness- and Modulus-Controlled SEI Layers on Lithium Metal Anodes. *J. Phys. Chem. C* **2018**, *122* (18), 9825–9834.
- (38) Muldoon, J.; Bucur, C. B.; Gregory, T. Quest for Nonaqueous Multivalent Secondary Batteries: Magnesium and Beyond. *Chem. Rev.* **2014**, *114* (23), 11683–11720.
- (39) Matsui, M. Study on Electrochemically Deposited Mg Metal. *J. Power Sources* **2011**, *196* (16), 7048–7055.
- (40) Wu, Y. A.; Yin, Z.; Farmand, M.; Yu, Y.-S.; Shapiro, D. A.; Liao, H.-G.; Liang, W.-I.; Chu, Y.-H.; Zheng, H. In-Situ Multimodal Imaging and Spectroscopy of Mg Electrodeposition at Electrode-Electrolyte Interfaces. *Sci. Rep.* **2017**, *7* (1), 1–9.
- (41) Hu, X.-C.; Shi, Y.; Lang, S.-Y.; Zhang, X.; Gu, L.; Guo, Y.-G.; Wen, R.; Wan, L.-J. Direct Insights into the Electrochemical Processes at Anode/Electrolyte Interfaces in Magnesium-Sulfur Batteries. *Nano Energy* **2018**, *49*, 453–459.
- (42) Ling, C.; Banerjee, D.; Matsui, M. Study of the Electrochemical Deposition of Mg in the Atomic Level: Why It Prefers the Non-Dendritic Morphology. *Electrochimica Acta* **2012**, *76*, 270–274.
- (43) Jäckle, M.; Groß, A. Microscopic Properties of Lithium, Sodium, and Magnesium Battery Anode Materials Related to Possible Dendrite Growth. *J. Chem. Phys.* **2014**, *141* (17), 174710.
- (44) Canepa, P.; Sai Gautam, G.; Hannah, D. C.; Malik, R.; Liu, M.; Gallagher, K. G.; Persson, K. A.; Ceder, G. Odyssey of Multivalent Cathode Materials: Open Questions and Future Challenges. *Chem. Rev.* **2017**, *117* (5), 4287–4341.
- (45) Yao, X.; Luo, J.; Dong, Q.; Wang, D. A Rechargeable Non-Aqueous Mg-Br₂ Battery. *Nano Energy* **2016**, *28*, 440–446.
- (46) Dong, Q.; Yao, X.; Luo, J.; Zhang, X.; Hwang, H.; Wang, D. Enabling Rechargeable Non-Aqueous Mg–O₂ Battery Operations with Dual Redox Mediators. *Chem. Commun.* **2016**, *52* (95), 13753–13756.
- (47) Tian, H.; Gao, T.; Li, X.; Wang, X.; Luo, C.; Fan, X.; Yang, C.; Suo, L.; Ma, Z.; Han, W.; Wang, C. High Power Rechargeable Magnesium/Iodine Battery Chemistry. *Nat. Commun.* **2017**, *8* (1), 1–8.

- (48) Gao, T.; Hou, S.; Wang, F.; Ma, Z.; Li, X.; Xu, K.; Wang, C. Reversible S₀/MgS_x Redox Chemistry in a MgTFSI₂/MgCl₂/DME Electrolyte for Rechargeable Mg/S Batteries. *Angew. Chem. Int. Ed.* **2017**, *56* (43), 13526–13530.
- (49) Aurbach, D.; Lu, Z.; Schechter, A.; Gofer, Y.; Gizbar, H.; Turgeman, R.; Cohen, Y.; Moshkovich, M.; Levi, E. Prototype Systems for Rechargeable Magnesium Batteries. *Nature* **2000**, *407* (6805), 724–727.
- (50) Pour, N.; Gofer, Y.; Major, D. T.; Aurbach, D. Structural Analysis of Electrolyte Solutions for Rechargeable Mg Batteries by Stereoscopic Means and DFT Calculations. *J. Am. Chem. Soc.* **2011**, *133* (16), 6270–6278.
- (51) Kim, H. S.; Arthur, T. S.; Allred, G. D.; Zajicek, J.; Newman, J. G.; Rodnyansky, A. E.; Oliver, A. G.; Boggess, W. C.; Muldoon, J. Structure and Compatibility of a Magnesium Electrolyte with a Sulphur Cathode. *Nat. Commun.* **2011**, *2* (1), 1–6.
- (52) Doe, R. E.; Han, R.; Hwang, J.; Gmitter, A. J.; Shterenberg, I.; Yoo, H. D.; Pour, N.; Aurbach, D. Novel, Electrolyte Solutions Comprising Fully Inorganic Salts with High Anodic Stability for Rechargeable Magnesium Batteries. *Chem. Commun.* **2013**, *50* (2), 243–245.
- (53) Son, S.-B.; Gao, T.; Harvey, S. P.; Steirer, K. X.; Stokes, A.; Norman, A.; Wang, C.; Cresce, A.; Xu, K.; Ban, C. An Artificial Interphase Enables Reversible Magnesium Chemistry in Carbonate Electrolytes. *Nat. Chem.* **2018**, *10* (5), 532–539.

Chapter 2. Wood derived porous carbon electrodes for Li-O₂ batteries

[This chapter is adapted with permission from “Jingru Luo, Xiahui Yao, Lei Yang, Yang Han, Liao Chen, Xiumei Geng, Vivek Vattipalli, Qi Dong, Wei Fan, Dunwei Wang, Hongli Zhu, Free-Standing Porous Carbon Electrodes Derived from Wood for High-Performance Li-O₂ Battery Applications. *Nano Res.* **2017**, *10* (12), 4318–4326. <https://doi.org/10.1007/s12274-017-1660-x>.” Copyright 2017 Springer Nature.]

Electrode materials with porous structures, particularly hierarchical pores, are highly coveted for energy applications such as fuel cells ^{1,2}, batteries ^{3,4} and (super) capacitors ^{5,6}. Of these materials, porous carbon is perhaps the most commonly used owing to its relatively high electrical conductivity, good chemical stability, low cost and the non-toxic nature ^{7,8}. However, most commercially available carbon materials are in particulate forms with typical sizes ranging between nanometers and microns ⁹, presenting challenges in assembling them for desired connectivity and mechanical strength for practical applications. One strategy to address this issue is to introduce polymeric additives as binders which help hold the particles together ¹⁰. While widely implemented in many commercially successful systems, such approach does introduce unintended consequences. For example, the addition of these inactive materials inadvertently adds to the weight and volume of devices ¹¹ (e.g., batteries) and complicate the manufacturing processes ¹². Moreover, the additives sometimes introduce unexpected side effects that are detrimental to the operation of energy conversion and storage devices ¹³. The problem can be especially acute for emerging technologies such as Li-O₂ batteries. For instance, poly (vinylidene

difluoride) (PVdF) as a binder plays a critical role in the success of Li-ion batteries, but it has been reported unstable with respect to superoxide species that are ubiquitous in Li-O₂ batteries^{14, 15}. Furthermore, there have been studies showing that the binders used in the cathode may limit O₂ diffusion by blocking the pores and reduce the active surface area for Li₂O₂ deposition^{16, 17}. These negative issues connected to the particulate nature of carbon can in principle be solved by using free-standing carbons that are much larger in their macro scale dimensions but feature pores of similar sizes in the micro and meso scale¹⁸. Indeed, efforts toward this direction have been proposed and promising preliminary results have been reported¹⁹⁻²⁴. For instance, Zhang *et al.*²⁰ developed a free-standing palladium-modified hollow spherical carbon cathode, which endows good performance in Li-O₂ batteries. Shao-Horn *et al.*²¹ reported a hierarchical functionalized multiwalled carbon nanotube/graphene structure as self-standing electrodes for the positive electrode of lithium ion batteries. The electrodes achieved a thickness up to tens of micrometers and a relatively high density (> 1 g cm⁻³).

Within the context of free-standing carbon with micro and meso scale pores, wood provides an ideal platform in that it offers macro scale structural integrity while presenting hierarchical pores inherent to its natural formation mechanism²⁵. When properly carbonized, the structural integrity and the porous nature can be preserved, yielding a carbon scaffold unique in its mechanical strength and structures²⁶. Inspired by this consideration, here we present a free-standing porous carbon derived from the Yellow Pine²⁷. To exploit the utilities of the structured pores in wood enabled by microfibrils and tracheids during growth, we applied the resulting carbon as a cathode for Li-O₂ batteries, where transport of a multitude of species is of critical importance²⁸. Take the discharge

process as an example. O_2 (from the gas phase) is reduced, the products of which bind with Li^+ (from the liquid phase) to form Li_2O_2 (as a solid). The process requires the transportation of O_2 from the headspace of the battery, Li^+ from the anode side through the electrolyte and electrons from the cathode ²⁹. The concerted transportation of these three components calls for high surface area for large capacity, good electrical conductivity for high current density and sufficiently large pores to prevent clogging ³⁰. All these requirements can be simultaneously met by wood-derived carbon. The channels and pores formed from the well-oriented microfibers and tracheids can serve as routes through which facile Li^+ and O_2 diffusion is ensured. Preserving the inherent structure of wood provides adequate mechanical strength for the carbon to be used as a free-standing electrode without excessive fabrication, eliminating the need for binders or conductive additives. Furthermore, we explore the facile doping of carbon by N during the carbonization process for enhanced O_2 reduction reaction (ORR) activities ^{31, 32}, which is critically important to the Li- O_2 battery operations.

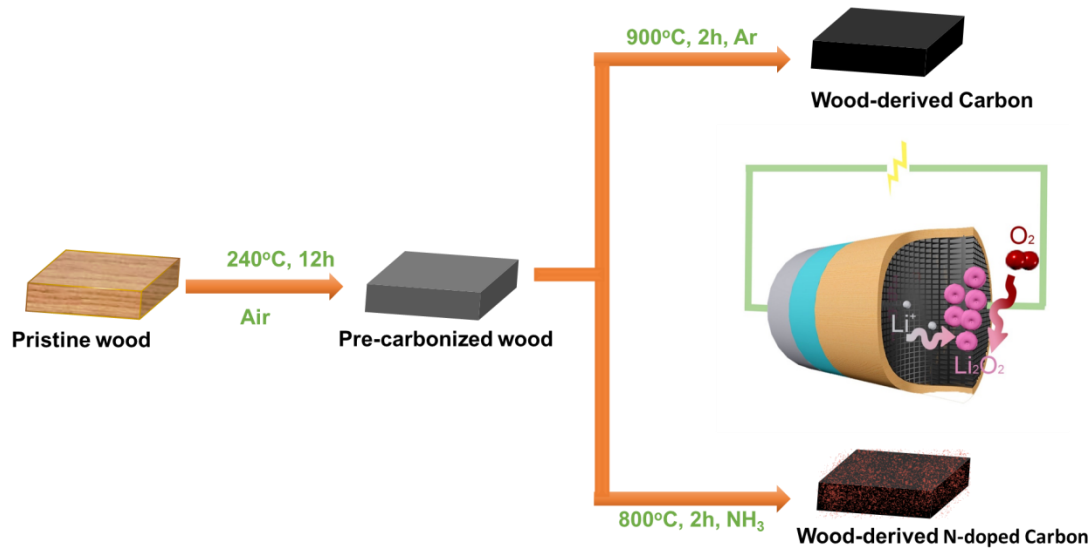


Figure 2-1. The preparation of wd-C/wd-NC and its application in Li- O_2 batteries. The

wood was first cut into rectangular pieces and baked at 240°C for 12 h in ambient air. For wd-C, the resulting sample was transferred to a tube furnace under Ar atmosphere for full carbonization at 900 °C for 2 h. For N-doped carbon (wd-NC), the carbonization was carried out at 800 °C with anhydrous NH₃ for 2 h.

2.1 Experimental

2.1.1 Material preparation

The pristine wood was obtained from Yellow Pine. The carbonization was carried out in two steps. As shown in **Figure 2-1**, the wood was first cut into rectangular pieces and baked at 240 °C for 12 h in ambient air. The resulting sample was then transferred to a tube furnace under Ar atmosphere (30 sccm) for full carbonization at 900 °C for 2 h to obtain wood-derived carbon (wd-C)³³.

For N-doped carbon (wd-NC), the carbonization was carried out at 800 °C with anhydrous NH₃ (Airgas, 75 sccm) for 2 h. The wd-NC was carbonized at 800 °C but not 900 °C because wood was found to react with NH₃ severely. The wd-C (and wd-NC) was further vacuum dried at 150 °C for at least 12 h in the antechamber before transferring into the glovebox (Mbraun, MB20G, with O₂ and H₂O concentrations < 0.1 ppm). All carbon samples were used directly without further processing with the areal density of 19 mg/cm² at the thickness of 1 mm.

2.1.2 Material characterization

Scanning electron microscopy (SEM) was collected on a JEOL 6340F microscope operating at 15 kV. Raman spectra were acquired using a micro-Raman system (XploRA, Horiba) with an excitation laser of $\lambda=532$ nm. The surface area and pore volume information was obtained by N₂ adsorption/desorption experiments carried out on an automatic gas sorption analyzer (Autosorb iQ, Quantachrome) at 77 K. For XPS analysis of the carbon electrode after Li-O₂ operations, the cell was transferred to an O₂-tolerant Ar-filled glove box (H₂O level < 0.1 ppm, MBraun), where it was disassembled to extract the cathodes. The cathodes were further washed with pure anhydrous dimethoxyethane (DME, anhydrous grade, Sigma-Aldrich) 3 times to remove trapped salts. Afterwards, the cathode was vacuumed to remove solvents and then transferred to the XPS (K-Alpha, Thermo Scientific) vacuum chamber with minimal exposure to ambient air (< 1 min). X-ray diffraction data was obtained on a PANalytical X'Pert Pro diffractometer with air-tight sample holder without exposing the sample to ambient air. Mechanical test was performed with a Discovery HR-1 hybrid rheometer. All samples tested were of the same dimensions (9mm×8mm×3mm).

2.1.3 Electrochemical characterization

LiClO₄ (99.99%, battery grade, Sigma-Aldrich) was first baked at 130 °C in the antechamber of the glovebox and then dissolved in DME to obtain a 0.1 M electrolyte solution. Customized Swagelok™ type cells were assembled in the glove box with Li metal (380 μm in thickness, Sigma-Aldrich) as the anode, 2 Celgard 2400 film as the

separator, and 0.1 M LiClO₄ (100 to 200 μL) as the electrolyte. The assembled batteries were then transferred to the O₂-tolerant Ar-filled glove box and O₂ (ultrahigh purity, Airgas) was purged into the cell to replace Ar. Electrochemical characterizations were conducted using an electrochemical station (Biologic, VMP3).

2.2 Results and discussion

The free-standing nature of the wd-NC with good structural integrity can be visualized in **Figure 2-2 (a)**. The mechanical properties of the resulting carbon were characterized by the engineering compression test. The ultimate loading stress before fracturing was reported in **Figure 2-2(b)** and **Figure 2-3**. As a comparison, commercial Vulcan carbon powder was fabricated into similar size and shape but was bonded by 5 % of PVdF, which is commonly used as cathode in literature³⁴. As seen in Fig. 1b, wd-NC bore the highest loading stress of 860 kPa. It clearly suggests that wd-NC features mechanical stability suitable for free-standing electrode applications.

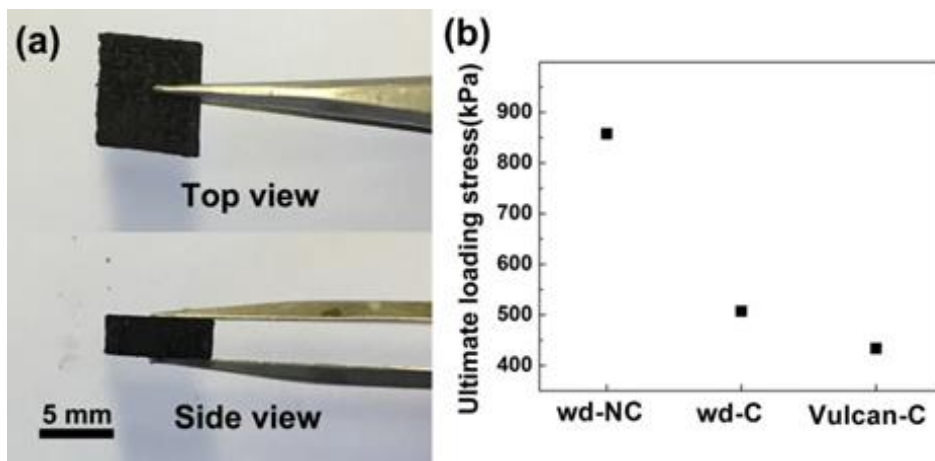


Figure 2-2. (a) Digital photos showing the structural integrity of freestanding wd-NC cathode; (b) Mechanical test showing the comparison between wd-NC, wd-C and Vulcan carbon. wd-NC can bear the highest loading stress of 860 kPa.

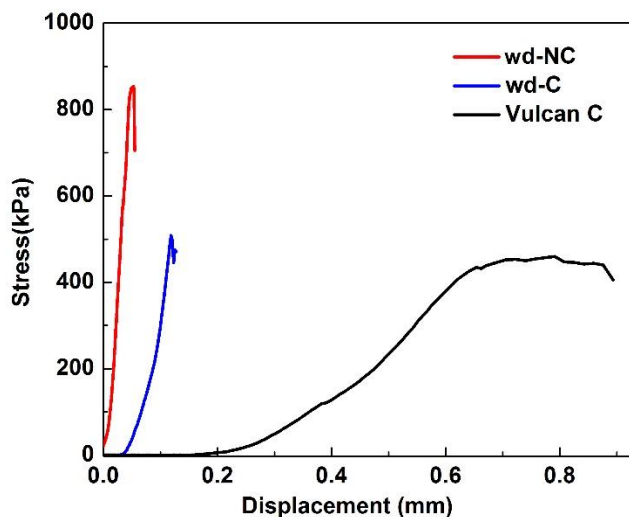


Figure 2-3. Compression tests show the ultimate loading stress of wd-NC, wd-C and Vulcan C. As a comparison, commercial Vulcan carbon powder was fabricated in to similar size and shape bonded by 5 % of PVdF. The sudden drop of the curves stands for the physical crush of the samples. The wd-NC can bear the highest loading stress of 860 kPa, which ensures a good mechanical stability of the wd-NC as a free-standing electrode.

During the first step of pre-carbonization, 67 % weight loss was measured as a result of dehydration and evaporation of small molecules. An additional 50 % weight loss was observed during the second step (i.e., the total weight the carbonized product is ca. 17 % of the original wood). However, for wd-NC, the resulting substrate was measured as 11% of the original weight of the parent wood, as opposed to 17 % in the process without N-doping. The additional weight loss is a result of the reactions between the carbon and

NH_3 to form HCN , C_2H_2 , CH_3NH_2 and $\text{CH}_3\text{C}\equiv\text{N}$ ³⁵. This process serves as an activation of the carbon material by enlarging the surface area and enlarging volumes. Though some carbon is consumed in the process, the structural integrity of the wd-NC remains identical to wd-C. The microstructure of the resulting carbons was further characterized by SEM. From the comparison among wd-C (**Figure 2-4 (a)**), wd-NC (**Figure 2-4 (b)**) and pre-carbonized wood (**Figure 2-5**), the diameters of the channels are in a similar range of 10 ~ 50 μm .

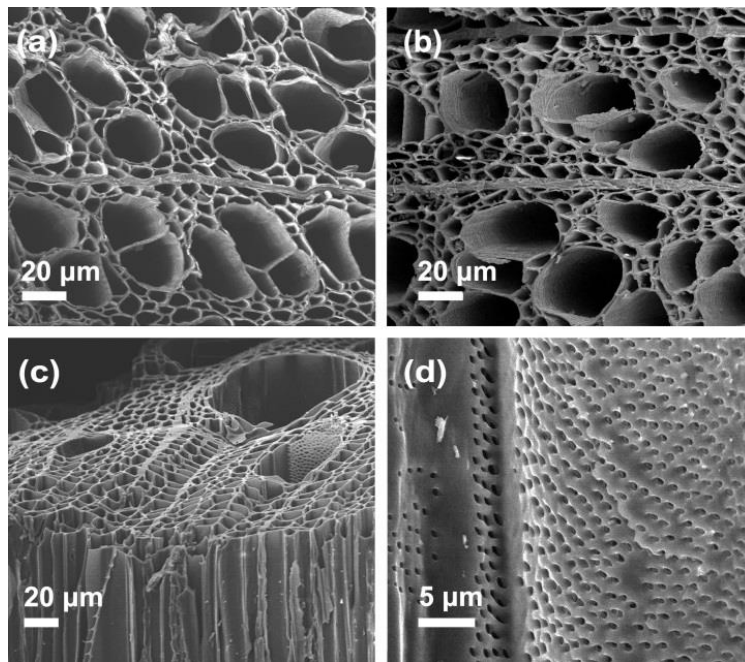


Figure 2-4. SEM images showing the microstructure of wd-C and wd-NC samples. (a) &(b) Top view of wd-C and wd-NC, respectively. (c) The hierarchical pore structure of wd-NC. (d) The inter-channel pores on the walls of wd-NC.

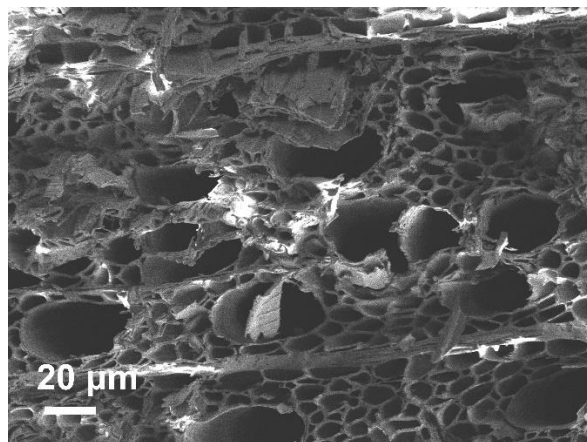


Figure 2-5. SEM image of pre- carbonized carbon. The porous structure is similar to that of wd-C and wd-NC. The pre-carbonized wood also features similar porous structure to wd-C and wd-NC. Due to the incompleteness of carbonization (and hence poor conductivity), the sample charged severely under SEM observations, resulting in the bright spots as shown in the figure.

However, the micropore volumes of the two samples differed, as shown in **Table 2-1**. wd-NC reached a pore volume of $0.36 \text{ cm}^3/\text{g}$, 10 times larger than wd-C. This difference can be explained by the reaction between carbon and NH_3 as mentioned above, which creates more pores inside carbon. **Figure 2-4(c)** shows that the hierarchical pore structure inherent to the parent wood remained intact, where channels enabled by aligned microfibers penetrating through the full thickness of the substrate to form interconnected pathways desired for mass transport in applications such as Li-O₂ batteries. In **Figure 2-4(d)**, a side-view image of the channel walls reveals the inter-channel pores on the walls of the carbon with the average diameter of $2 \mu\text{m}$. This inter-channel pores are expected to further facilitate mass transport by providing additional pathways in the event of pore clogging at the ends of the channels.

Table 2-1 Summary of BET surface area and pore volume for wd-NC and wd-C samples.

Sample	BET surface area (m ² /g)	Micro pore volume (cm ³ /g)	Total pore volume (cm ³ /g)
wd-C	75.5	0.035	0.035
wd-NC	745	0.22	0.36
Vulcan XC72 ^a	254 ^a	—	0.174 ^a

^a The data of Vulcan carbon from literature values was provided for comparison. (*Energy Environ. Sci.* **2012**, *5*, 8608-8620.)

Raman spectra and X-ray photoelectron spectra (XPS) were obtained to confirm the carbonization of wood and N doping. From the Raman spectra (**Figure 2-6(a)**), the two peaks corresponding to the D band at $\sim 1330\text{ cm}^{-1}$ and G band at $\sim 1590\text{ cm}^{-1}$ ³⁶ were prominent for both wd-C and wd-NC samples, whereas pristine wood sample featured severe fluorescence effect under illumination. The disappearance of the fluorescent behavior in the two carbon samples indicates the complete conversion from wood to carbon. The slightly higher D/G ratio of wd-NC sample indicates slightly poorer crystallinity of the sample. While the difference may be reflected on the conductivity and stability of the cathode materials, the effect is expected to be insignificant.

The N content of wd-NC was further characterized by XPS. **Figure 2-6(b)** revealed the existence of carbon species in the form of C-C, C-N, C-O and C=O bonding. Semi-quantitative elemental analysis from XPS yielded 8% of N content on the surface of N-doped carbon and 9% O species. By comparison, XPS characterization of wd-C did not show any N signal (**Figure 2-7**). Further examinations of the N 1s spectrum (**Figure 2-6(c)**) revealed the chemical environment of doped N. The most prominent form appears to be pyridinic N as represented by the peak with a binding energy of 398.2 eV³⁷. This binding environment has been previously reported as the most active for the oxygen reduction reactions (ORR). For example, Guo et. al.³² have shown that carbon atoms next to pyridinic N are the active sites for O₂ adsorption, which is the initial step of ORR. In the

same XPS spectrum (**Figure 2-6(c)**), there is also a second peak corresponding to pyrrolic N at 400.7 eV. This is consistent with N substituting O in the 5-membered ring of the carbon precursor³⁷. This analysis suggests that doped N has the potential to improve the ORR activity. More on this will be discussed later in this article.

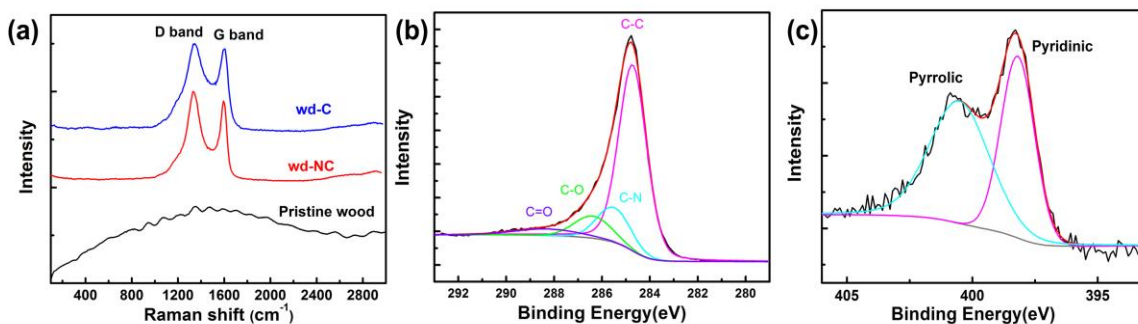


Figure 2-6. Raman and XPS characterization confirming the carbonization and N doping of wd-NC (a) The two Raman peaks corresponding to the D band at $\sim 1330\text{ cm}^{-1}$ and G band at $\sim 1590\text{ cm}^{-1}$ of carbon are prominent for both wd-C and wd-NC samples. (b) XPS spectrum of C 1s electrons revealing the bonding environment of C in wd-NC. (c) XPS spectrum of N 1s electrons confirming the N doping in wd-NC and showing the chemical environment of N. The most prominent component is the pyridinic N with the binding energy of 398.2 eV.

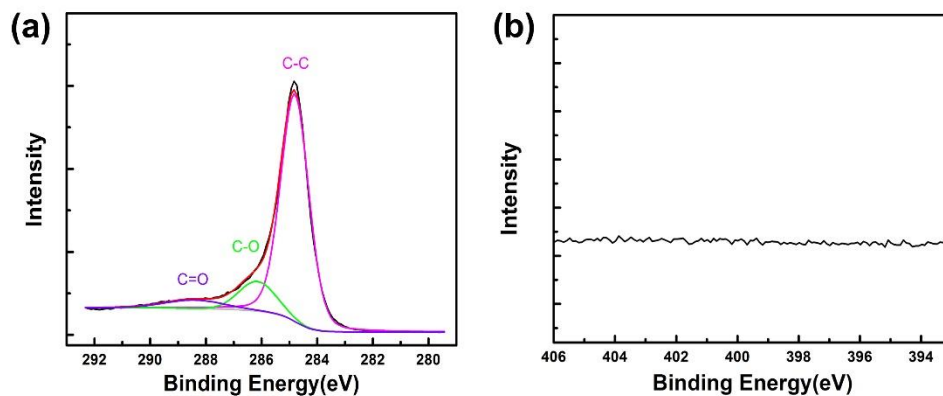


Figure 2-7. XPS characterization of wd-C indicated no N content on the wd-C surface.

(a) C1s spectrum of wd-C; (b) N1s spectrum of wd-C.

Next, we studied the electrochemical activity of wood-derived freestanding carbon by building it into Li-O₂ batteries as a cathode material. First, we compared the performance of wd-NC with wd-C to investigate the effect of hetero-atom (N atoms) on Li-O₂ battery performance. As shown in **Figure 2-8**, the discharge capacity for wd-NC was 1.86 mAh/cm², ca. 5 times higher than wd-C (0.38 mAh/cm²). The value is comparable to particulate carbon cathodes bonded by polymers (1~10 mAh/cm²). The discharge potential increased from 2.55 V (wd-C) to 2.70 V (wd-NC) as calculated from the plateau value of the discharge profile.

This phenomenon can be explained by the intrinsically high catalytic activity of N doped carbon, which is supported by previous experimental and computational works^{32, 38}. The NH₃ doping process can also further activate carbon by creating more micropores and enlarging the surface area. More significantly, the average recharge potential decreased from 4.20 V to 3.45 V, suggesting the discharge product may have more intimate contact with the cathode for more facile decomposition of Li₂O₂. Overall, the average overpotential of the charge/discharge process decreased from 1.65 V to 0.75 V with a capacity increase of 5 times for wd-NC. The remarkable performance improvement further highlights the positive effects of N doping.

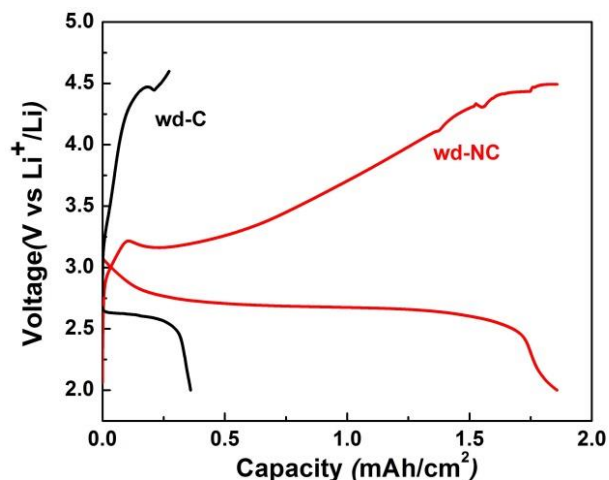


Figure 2-8. Voltage profiles of wd-NC and wd-C as cathodes with the same current density of 0.08 mA/cm^2 (4 mA/g). Compared with wd-C, the average roundtrip overpotential of wd-NC decreased from 1.65 V to 0.75 V and the areal capacity increased by 5 times.

To demonstrate the practicability of the freestanding wd-NC cathode, we next characterized the test Li-O₂ battery cell at different charging/discharging rates. As shown in **Figure 2-9(a)** and **Figure 2-10**, with the current density varying between 0.04 mA/cm^2 and 0.20 mA/cm^2 , the discharge voltage plateau decreased from 2.75 V to 2.40 V , and the charge voltage plateau increased from 3.3 V to 4.4 V . This observation indicates that N doping facilitates the ORR kinetics more effectively than it does the OER. Galvanostatic cycling tests were carried under a constant current density of 0.08 mA/cm^2 (with the capacity being limited at 1.5 mAh , or 70% depth of full discharge). As presented in **Figure 2-11**, for the first 20 cycles the battery exhibited a stable discharge plateau of 2.5 V . However, the energy efficiency decreased from 70% to 60% after 5 cycles. Such poor stability of carbon cathode has been observed by other authors and us. We have shown previously that passivating carbon cathode or decorating it with catalysts or both could improve the cycling performance by reducing parasitic chemical reactions ³⁰.

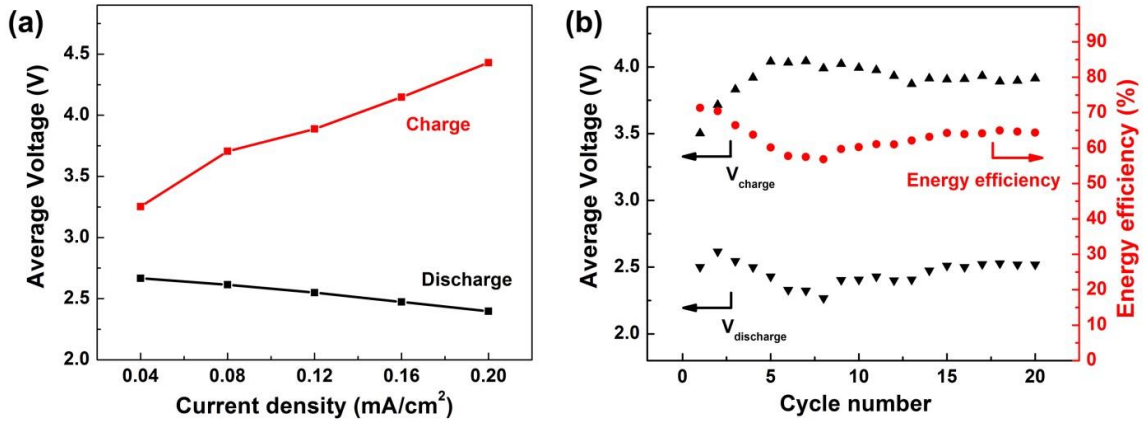


Figure 2-9. Rate capability and cycling performance of wd-NC. (a) With the current density increased from 0.04 mA/cm² to 0.20 mA/cm², the discharge voltage plateau decreased from 2.75 V to 2.40 V, and the charge voltage plateau increased from 3.3 V to 4.4 V, indicating N doping facilitates the ORR kinetics more effectively than it does the OER. (b) Galvanostatic cycling tests under a constant current density of 0.08 mA/cm² and 70% depth of full discharge (Absolute capacity each cycle: 1.5 mAh). The average voltages and energy efficiency for each cycle was plotted against the cycle number. The energy efficiency decreased from 70% to 60% after 5 cycles and remained stable onward.

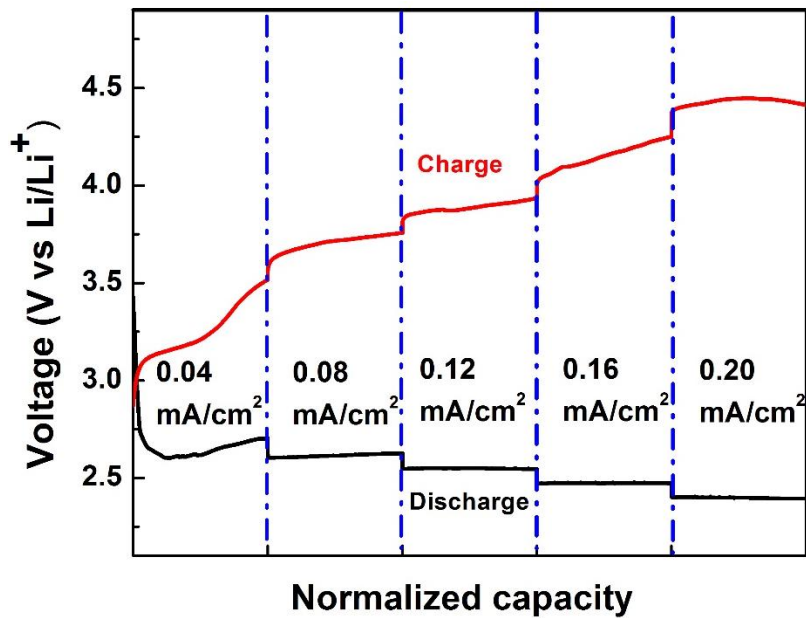


Figure 2-10. Rate capability of wd-NC. With the current density increases from $0.04\text{mA}/\text{cm}^2$ to $0.20\text{mA}/\text{cm}^2$, the discharge plateau decreased from 2.75V to 2.40V , and the charge plateau increased from 3.3V to 4.4V , indicating the N doping facilitates the ORR kinetics more than the OER. Each discharge / charge plateau at different current density was normalized to the same capacity.

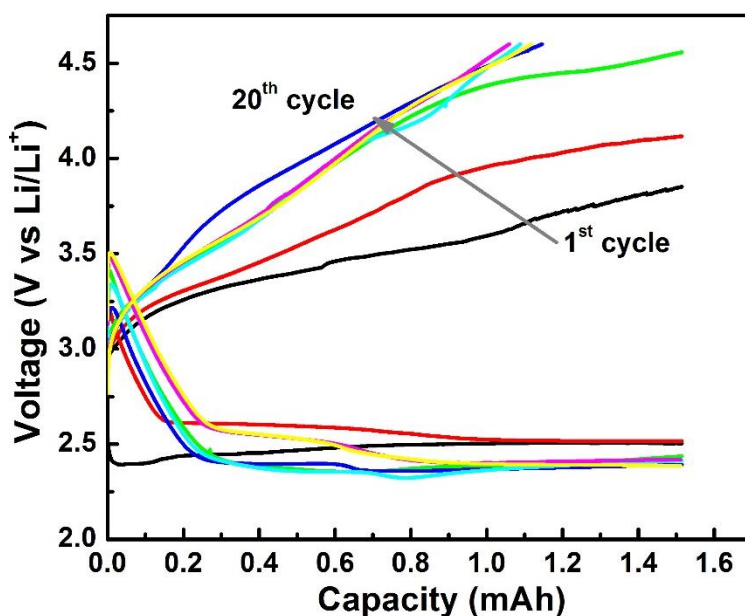


Figure 2-11. Cycling performance of wd-NC with a limited discharge capacity of 1.5mAh at a current density of $0.08\text{mA}/\text{cm}^2$. Representative cycle profiles of the 1st, 2nd, 5th, 10th, 13th, 18th, 20th cycles are color coded and shown for clarity. Within 20 cycles the battery showed a stable discharge plateau at around 2.5V , which indicated a reasonable cyclability of the wd-NC. However, the average recharge voltage increased from 3.5V to 4.0V , which resulted in the decrease of energy efficiency.

Our next task for this body of work was to analyze the discharge and recharge products. This task is of paramount importance because proving the electrochemical

characteristics are indeed connected to Li_2O_2 formation/decomposition is critical. For this purpose, we conducted X-ray diffraction (XRD) characterization. As shown in **Figure 2-12(a)**, the XRD pattern unambiguously confirmed the formation of Li_2O_2 upon discharge. The peaks at 32.8° and 34.8° match the documented diffraction peaks of Li_2O_2 (JCPDS 74-0115). A shifted by-product peak of Li_2CO_3 at 31.5° was also observed in the same XRD spectrum. The slight shift (-0.3°) than standard pattern (JCPDS 87-0729) is common for solution derived sample³⁹, relating with the solvation of Li^+ . XPS spectra were also collected to verify the composition of Li_2O_2 (**Figure 2-12(b)&(c)**). After discharge, the peaks at 55.0 eV (Li 1s) and 531.8 eV (O 1s) increased dramatically, indicating the formation of Li_2O_2 . After recharge, much less O 1s signal at 534.0 eV and Li 1s signal at 55.0 eV were observed, indicating the decomposition of Li_2O_2 ⁴⁰.

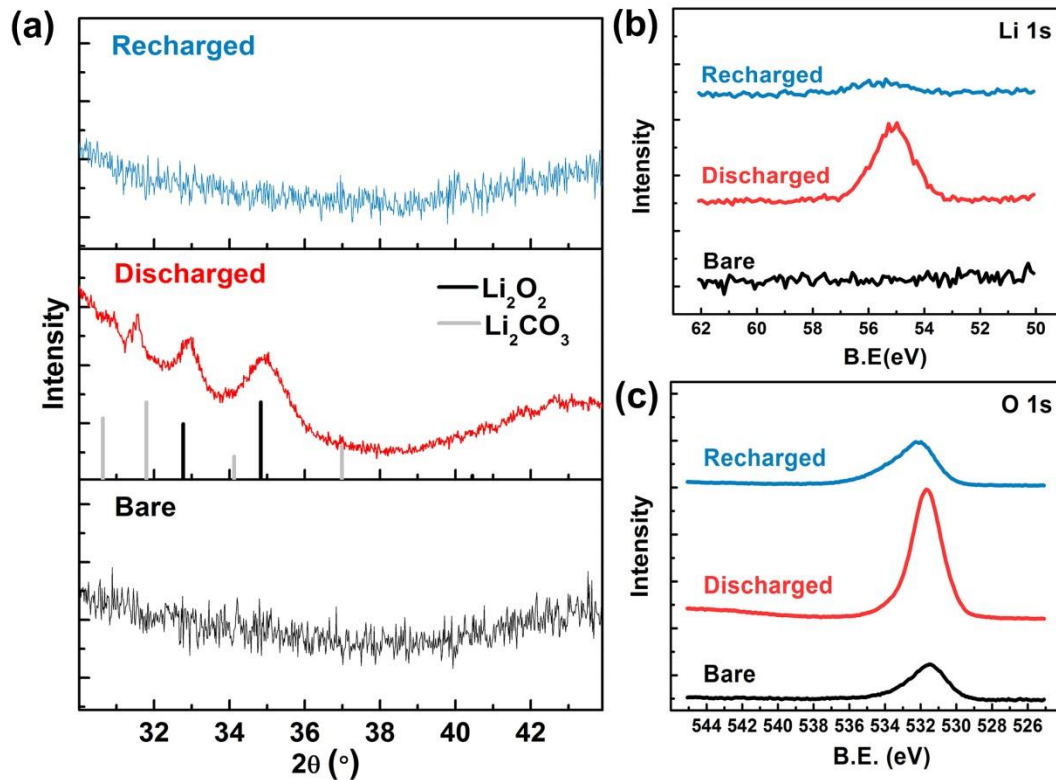


Figure 2-12. Li_2O_2 detection. (a) X-ray diffraction patterns of wd-NC before discharge (bare), after the 1st cycle discharge (discharged) and the 1st cycle recharge (recharged). The peaks at 32.8° and 34.8° in the discharged sample match the documented diffraction peaks of Li_2O_2 (JCPDS 74-0115). (b) & (c) XPS spectra of Li 1s and O 1s confirming the formation and decomposition of Li_2O_2 . After discharge, the peaks at 55.0 eV (Li 1s) and 531.8 eV (O 1s) increased dramatically, indicating the formation of Li_2O_2 . After recharge, much less O 1s and Li 1s signal were observed, indicating the decomposition of Li_2O_2 .

Scanning electron micrographs (SEM) as shown in **Figure 2-13** further support the Li_2O_2 formation/decomposition. The surface of pristine wd-NC was smooth and clean (**Figure 2-13(a)**). After discharge, Li_2O_2 particles were observed to accumulate both inside the pores and on the surface of the carbon walls (**Figure 2-13(b)**). After full recharge, those particles disappeared (**Figure 2-13(c)**). The SEM images together with the XRD and XPS results provide strong support that Li_2O_2 formation and decomposition was connected to the discharge and recharge electrochemical characteristics. The quantitative product detection of Li_2O_2 by idometric titration method was not successful in this study^{30,41}. This is due to the large surface area and tortuosity of our free standing wood-derived N-doped carbon, which leads to strong adsorption of iodine.

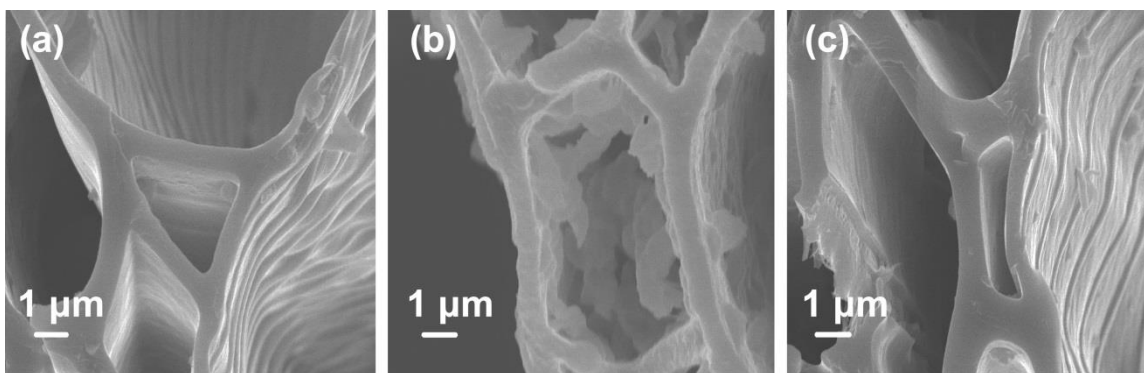


Figure 7 SEM image confirming the formation and decomposition of Li_2O_2 . (a) Clean surface of the bare wd-NC. (b) After discharge, Li_2O_2 particles were observed to accumulate on the surfaces of wd-NC. (c) After full recharge, the Li_2O_2 particles were decomposed and the surface of the wd-NC was revealed.

2.3 Conclusion

In summary, we have investigated a new nitrogen-doped free-standing porous carbon material as a promising cathode material for Li-O₂ battery. This material takes advantage of the spontaneously formed hierarchical porous structure derived from wood. The structure is expected to facilitate both mass transport and discharge product storage. Moreover, we introduced heteroatom (N) doping to further improve the catalytic activity of the carbon cathode for lower overpotential and higher capacity. We have unambiguously confirmed the initial electrochemical process to be the desired reactions of Li_2O_2 formation and decomposition. The free standing nature and mechanical strength of wood derived carbon makes it possible to eliminate the need for additional current collector and binders, improving the overall energy density and reducing possible parasitic chemical reactions. Also, the renewability of wood with this unique structure could potentially provide a cost-effective route as porous electrode for large-scale mass production. Further effort to improve the cell performance can be anticipated by protecting the carbon surface using strategies that have been demonstrated by us and others previously.

2.4 References

- (1) Fang, B.; Kim, J. H.; Kim, M.; Yu, J.-S. Ordered hierarchical nanostructured carbon as a highly efficient cathode catalyst support in proton exchange membrane fuel cell. *Chem. Mater.* **2009**, *21*, 789-796.
- (2) Kjeang, E.; Michel, R.; Harrington, D. A.; Djilali, N.; Sinton, D. A microfluidic fuel cell with flow-through porous electrodes. *J. Am. Chem. Soc.* **2008**, *130*, 4000-4006.
- (3) Long, J. W.; Dunn, B.; Rolison, D. R.; White, H. S. Three-dimensional battery architectures. *Chem. Rev.* **2004**, *104*, 4463-4492.
- (4) Ogasawara, T.; Débart, A.; Holzapfel, M.; Novák, P.; Bruce, P. G. Rechargeable Li_2O_2 electrode for lithium batteries. *J. Am. Chem. Soc.* **2006**, *128*, 1390-1393.
- (5) Wang, D.-W.; Li, F.; Liu, M.; Lu, G. Q.; Cheng, H.-M. 3D aperiodic hierarchical porous graphitic carbon material for high-rate electrochemical capacitive energy storage. *Angew. Chem., Int. Ed.* **2008**, *47*, 373-376.
- (6) Zhai, Y.; Dou, Y.; Zhao, D.; Fulvio, P. F.; Mayes, R. T.; Dai, S. Carbon materials for chemical capacitive energy storage. *Adv. Mater.* **2011**, *23*, 4828-4850.
- (7) Pandolfo, A. G.; Hollenkamp, A. F. Carbon properties and their role in supercapacitors. *J. Power Sources* **2006**, *157*, 11-27.
- (8) Dutta, S.; Bhaumik, A.; Wu, K. C. W. Hierarchically porous carbon derived from polymers and biomass: Effect of interconnected pores on energy applications. *Energy Environ. Sci.* **2014**, *7*, 3574-3592.
- (9) Long, C. M.; Nascarella, M. A.; Valberg, P. A. Carbon black vs. black carbon and other airborne materials containing elemental carbon: Physical and chemical distinctions. *Environ. Pollut.* **2013**, *181*, 271-286.
- (10) Liu, G.; Zheng, H.; Song, X.; Battaglia, V. S. Particles and polymer binder interaction: A controlling factor in lithium-ion electrode performance. *J. Electrochem. Soc.* **2012**, *159*, A214-A221.
- (11) Ha, D.-H.; Islam, M. A.; Robinson, R. D. Binder-free and carbon-free nanoparticle batteries: a method for nanoparticle electrodes without polymeric binders or carbon black. *Nano Lett.* **2012**, *12*, 5122-5130.
- (12) Chen, Z.; Li, H.; Tian, R.; Duan, H.; Guo, Y.; Chen, Y.; Zhou, J.; Zhang, C.; Dugnani, R.; Liu, H. Three dimensional graphene aerogels as binder-less, freestanding, elastic and high-performance electrodes for lithium-ion batteries. *Sci. Rep.* **2016**, *6*, 27365.
- (13) Yao, X.; Dong, Q.; Cheng, Q.; Wang, D. Why do lithium–oxygen batteries fail: parasitic chemical reactions and their synergistic effect. *Angew. Chem., Int. Ed.* **2016**, *55*, 11344-11353.
- (14) Black, R.; Oh, S. H.; Lee, J.-H.; Yim, T.; Adams, B.; Nazar, L. F. Screening for superoxide reactivity in Li-O_2 batteries: Effect on $\text{Li}_2\text{O}_2/\text{LiOH}$ crystallization. *J. Am. Chem. Soc.* **2012**, *134*, 2902-2905.
- (15) Amanchukwu, C. V.; Harding, J. R.; Shao-Horn, Y.; Hammond, P. T. Understanding the chemical stability of polymers for lithium–air batteries. *Chem. Mater.* **2015**, *27*, 550-561.

- (16) Etacheri, V.; Sharon, D.; Garsuch, A.; Afri, M.; Frimer, A. A.; Aurbach, D. Hierarchical activated carbon microfiber (ACM) electrodes for rechargeable Li–O₂ batteries. *J. Mater. Chem. A* **2013**, *1*, 5021-5030.
- (17) Lacey, M. J.; Jeschull, F.; Edström, K.; Brandell, D. Porosity blocking in highly porous carbon black by PVdF binder and its implications for the Li–S system. *J. Phys. Chem. C* **2014**, *118*, 25890-25898.
- (18) Wang, Z.-L.; Xu, D.; Xu, J.-J.; Zhang, L.-L.; Zhang, X.-B. Graphene oxide gel-derived, free-standing, hierarchically porous carbon for high-capacity and high-rate rechargeable Li-O₂ batteries. *Adv. Funct. Mater.* **2012**, *22*, 3699-3705.
- (19) Liu, Q.-C.; Xu, J.-J.; Xu, D.; Zhang, X.-B. Flexible lithium-oxygen battery based on a recoverable cathode. *Nat. Commun.* **2015**, *6*, 7892.
- (20) Xu, J.-J.; Wang, Z.-L.; Xu, D.; Zhang, L.-L.; Zhang, X.-B. Tailoring deposition and morphology of discharge products towards high-rate and long-life lithium-oxygen batteries. *Nat. Commun.* **2013**, *4*, 2438.
- (21) Byon, H. R.; Gallant, B. M.; Lee, S. W.; Shao-Horn, Y. Role of oxygen functional groups in carbon nanotube/graphene freestanding electrodes for high performance lithium batteries. *Adv. Funct. Mater.* **2013**, *23*, 1037-1045.
- (22) Yin, Y.-B.; Xu, J.-J.; Liu, Q.-C.; Zhang, X.-B. Macroporous interconnected hollow carbon nanofibers inspired by golden-toad eggs toward a binder-free, high-rate, and flexible electrode. *Adv. Mater.* **2016**, *28*, 7494-7500.
- (23) Chang, Z.-w.; Xu, J.-j.; Liu, Q.-c.; Li, L.; Zhang, X.-b. Recent progress on stability enhancement for cathode in rechargeable non-aqueous lithium-oxygen battery. *Adv. Energy Mater.* **2015**, *5*, 1500633.
- (24) Liu, T.; Liu, Q.-C.; Xu, J.-J.; Zhang, X.-B. Cable-type water-survivable flexible Li-O₂ battery. *Small* **2016**, *12*, 3101-3105.
- (25) Zhu, H.; Luo, W.; Ciesielski, P. N.; Fang, Z.; Zhu, J. Y.; Henriksson, G.; Himmel, M. E.; Hu, L. Wood-derived materials for green electronics, biological devices, and energy applications. *Chem. Rev.* **2016**, *116*, 9305-9374.
- (26) Zhu, H.; Jia, Z.; Chen, Y.; Weadock, N.; Wan, J.; Vaaland, O.; Han, X.; Li, T.; Hu, L. Tin anode for sodium-ion batteries using natural wood fiber as a mechanical buffer and electrolyte reservoir. *Nano Lett.* **2013**, *13*, 3093-3100.
- (27) Byrne, C.; Nagle, D. Carbonization of wood for advanced materials applications. *Carbon* **1997**, *35*, 259-266.
- (28) Read, J.; Mutolo, K.; Ervin, M.; Behl, W.; Wolfenstine, J.; Driedger, A.; Foster, D. Oxygen transport properties of organic electrolytes and performance of lithium/oxygen battery. *J. Electrochem. Soc.* **2003**, *150*, A1351-A1356.
- (29) Bruce, P. G.; Freunberger, S. A.; Hardwick, L. J.; Tarascon, J.-M. Li-O₂ and Li-S batteries with high energy storage. *Nat. Mater.* **2012**, *11*, 19-29.
- (30) Xie, J.; Yao, X.; Cheng, Q.; Madden, I. P.; Dornath, P.; Chang, C.-C.; Fan, W.; Wang, D. Three dimensionally ordered mesoporous carbon as a stable, high-performance Li–O₂ battery cathode. *Angew. Chem., Int. Ed.* **2015**, *54*, 4299-4303.
- (31) Gong, K.; Du, F.; Xia, Z.; Durstock, M.; Dai, L. Nitrogen-doped carbon nanotube arrays with high electrocatalytic activity for oxygen reduction. *Science* **2009**, *323*, 760-764.

- (32) Guo, D.; Shibuya, R.; Akiba, C.; Saji, S.; Kondo, T.; Nakamura, J. Active sites of nitrogen-doped carbon materials for oxygen reduction reaction clarified using model catalysts. *Science* **2016**, *351*, 361-365.
- (33) Pang, J.; John, V. T.; Loy, D. A.; Yang, Z.; Lu, Y. Hierarchical mesoporous carbon/silica nanocomposites from phenyl-bridged organosilane. *Adv. Mater.* **2005**, *17*, 704-707.
- (34) Lu, Y.-C.; Kwabi, D. G.; Yao, K. P. C.; Harding, J. R.; Zhou, J.; Zuin, L.; Shao-Horn, Y. The discharge rate capability of rechargeable Li-O₂ batteries. *Energy Environ. Sci.* **2011**, *4*, 2999-3007.
- (35) Shevlin, P. B.; McPherson, D. W.; Melius, P. Reaction of atomic carbon with ammonia. The mechanism of formation of amino acid precursors. *J. Am. Chem. Soc.* **1983**, *105*, 488-491.
- (36) Tuinstra, F. Raman spectrum of graphite. *J. Chem. Phys.* **1970**, *53*, 1126.
- (37) Matter, P. H.; Zhang, L.; Ozkan, U. S. The role of nanostructure in nitrogen-containing carbon catalysts for the oxygen reduction reaction. *J. Catal.* **2006**, *239*, 83-96.
- (38) Gong, K.; Du, F.; Xia, Z.; Durstock, M.; Dai, L. Nitrogen-doped carbon nanotube arrays with high electrocatalytic activity for oxygen reduction. *Science* **2009**, *323*, 760-764.
- (39) Yin, W.; Grimaud, A.; Lepoivre, F.; Yang, C.; Tarascon, J. M. Chemical vs electrochemical formation of Li₂CO₃ as a discharge product in Li-O₂/CO₂ batteries by controlling the superoxide intermediate. *J. Phys. Chem. Lett.* **2017**, *8*, 214-222.
- (40) Younesi, R.; Hahlin, M.; Björefors, F.; Johansson, P.; Edström, K. Li-O₂ battery degradation by lithium peroxide (Li₂O₂): A model study. *Chem. Mater.* **2013**, *25*, 77-84.
- (41) Xie, J.; Dong, Q.; Madden, I.; Yao, X.; Cheng, Q.; Dornath, P.; Fan, W.; Wang, D. Achieving low overpotential Li-O₂ battery operations by Li₂O₂ decomposition through one-electron processes. *Nano Lett.* **2015**, *15*, 8371-8376.

Chapter 3. Enabling lithium metal anode in nonflammable phosphate electrolyte

[This chapter is adapted from a paper to be submitted, “Haochuan Zhang,[†] Jingru Luo,[†] Miao Qi, Qi Dong, Nicholas Dulock, Christopher Pavinelli, Nicholas Wong, Dunwei Wang, “Enabling Lithium Metal Anode in Nonflammable Phosphate Electrolyte with Electrochemically-Induced Chemical Reactions”.]

Safety is of paramount importance to modern electrochemical energy storage devices. For state-of-the-art Li-ion batteries, a common failure mechanism is understood to start with uneven plating of Li on the anode, which leads to the formation of dendrites that short the circuit¹⁻⁴. The flammable nature of the common electrolytes exacerbates the problem and, hence, the often-dramatic fashion in which batteries fail. Concerns over the safety issue have been a key roadblock that limits the development of new battery technologies. For instance, the promises held by new cathode chemistries, such as Li-S and Li-O₂ batteries, could not be materialized unless the anode is of high-capacities, which can only be delivered by Li metals. To this end, being able to safely use Li metal as the anode has broad appeals, thanks to its low electrochemical potential and unparalleled capacity⁵. In recognition of these concerns and opportunities, significant research attention has been attracted to study how to greatly increase the capacity of batteries without compromising safety by, for example, enabling Li metal or employ non-flammable electrolytes or both. Researchers have examined what has worked extremely well in state-of-the-art Li-ion batteries and found that the initial electrochemical reactions between the anode (graphite)

and the electrolyte (typically organic carbonate-based solutions) hold the key. As a result of the initial electrochemical reactions, a thin layer of complex compositions comprised of inorganic and organic Li salts (*i.e.*, the solid-electrolyte interphase layer, or SEI) serve to permit only Li^+ to pass, so as to suppress uncontrolled Li plating that can short the circuit². The SEI also limits runaway “dead” Li, which have been suggested as a culprit for capacity losses. Inspired by this understanding, researchers have tested a number of approaches on forming a SEI on Li metal similar to that on graphite. For instance, fluoroethylene carbonate (FEC) and LiNO_3 have proven effective as additives in introducing LiF-rich and Li_3N -rich SEI for stable Li operations, respectively^{6,7}. Separately, coating of reactive polymer composites has been shown to enable the formation of self-repairing SEI for high-efficiency cycling in lean electrolyte conditions⁸. These exciting progresses notwithstanding, the prior demonstrations were carried out in electrolytes that are flammable. The safety concerns connected to the flammability of the electrolyte remain outstanding. It is, therefore, important to correct the deficiency by exploring Li/electrolyte reactions in non-flammable electrolytes. Our project is conceived within this context, with the goal of enabling the formation of a stable SEI to permit operations of Li metal in non-flammable media.

Great attention has already been attracted to replicate stable SEI formation on Li anode in nonflammable electrolytes. With all other parameters equal, being able to replace flammable electrolytes with nonflammable ones should readily improve the safety of batteries. Guided by this idea, a number of solvents have been tested, and organic phosphates (*e.g.*, triethyl phosphate or TEP) stand out. This is because the P atoms can act as trapping agents for hydrogen radicals that play critical roles in initiating combustion

chain reactions⁹. Indeed, prior studies have shown that TEP could serve as a flame retardant to reduce the flammability of the conventional electrolytes. Direct utilization of TEP for Li-ion batteries, however, exhibited a multitude of problems, including speculated TEP insertion into graphite and rapidly increasing interface resistance on Li metal⁹. To circumvent these issues, approaches such as adding nitrate salts or relying on the decomposition of salts but not solvents have been proposed and proven promising^{10,11}. Inspired by these prior efforts, we hereby report a radically new approach. Our strategy involves promoting new chemical reaction pathways. It takes advantage of the unique reactivity between electrochemically reduced O₂ species and TEP, which enables the formation of a stable and effective SEI directly on Li anode. The reaction mechanism is supported by the detection of the corresponding products both in the electrolyte and the SEI. When tested in a symmetric Li||Li cell, >300 cycles of repeated Li plating and stripping was achieved at a current density of 0.5 mA·cm⁻²; when tested in a Li-O₂ prototypical cell, the system showed comparable performance as in a flammable, ether-based electrolyte. Similar strategy worked equally well for prototypical Li-ion batteries, too. The approach represents a new direction in addressing the critical safety concerns for high-capacity electrochemical energy storage technologies.

3.1 Experimental

3.1.1 Materials preparation

TEP (99.98%, Sigma-Aldrich) was dried with 4 Å molecular sieves prior to use. DME (99.99%) was purchased from BASF and used directly. LiTFSI (> 99.95%), LiClO₄ (99.9%), Li ribbon (> 99.9%) and polytetrafluoroethylene (PTFE, 60 wt% aq.) were purchased from Sigma-Aldrich. LiFePO₄ (LFP, active material density: 120 g/m², single sided) was purchased from MTI. Three-dimensionally ordered mesoporous (3DOm) carbon was prepared according to the procedure reported by Fan *et al.*¹². The O₂ electrode was prepared by drop-casting method. 3DOm carbon was firstly mixed with PTFE binder and then well dispersed in isopropyl alcohol (IPA) in a 95:5 mass ratio. The prepared solution was then drop casted onto the carbon paper substrate repeatedly to achieve a specific weight loading (1.0 ± 0.1 mg). Since the carbon paper area is ca. 1.0 cm², the density loading of 3DOm carbon is ca. 1.0 mg/cm². All electrodes were dried in a vacuum oven for 2 days at 150° C before battery assembly. The TEP-electrolyte was prepared by dissolving 1M LiTFSI into TEP.

3.1.2 Materials characterization

Scanning electron microscopy (SEM) was collected on a JEOL 6340F microscope operating at 10 kV. XX-ray photoelectron spectroscopy (XPS) was carried out on a K-Alpha+ XPS (Thermo Scientific) with an Al X-ray source (incident photon energy 1486.7

eV). Infrared (IR) spectra were recorded on a Bruker Alpha attenuated total reflectance infrared spectrometer. ^1H NMR spectra were collected on a Varian Unity INOVA spectrometers (500 MHz, or 600 MHz) with chemical shifts reported in ppm. Impedance spectra were recorded by using a ModuLab[®] XM potentiostat. The EIS data were measured by a 25 mV perturbation from 1MHz to 0.1 Hz. Raman spectra were acquired using a micro-Raman system (XploRA, Horiba) with an excitation laser of $\lambda=532$ nm.

3.1.3 Electrochemical characterization

Customized SwagelokTM type cells were assembled in the glove box (Mbruan, O_2 and $\text{H}_2\text{O} < 0.1$ ppm) with Li metal as the anode, 2 Celgard 2400 film as the separator, and 1 M LiTFSI in TEP (200 μL) as the electrolyte. The assembled batteries were then transferred to the O_2 -tolerant Ar-filled glove box and O_2 (ultrahigh purity, Airgas) was purged into the cell to replace Ar. Electrochemical characterizations were conducted using an electrochemical station (Biologic, VMP3). Cyclic Voltammetry (CV) study of Li metal reversibility in TEP electrolytes was conducted in the Li||Cu cell with a scan rate of 0.4 mV/s. Long-term cycling test of Li metal in TEP electrolyte was conducted in the Li||Li cell for at a current density of $0.5 \text{ mA}\cdot\text{cm}^{-2}$. CV measurement for O_2 chemistry evaluation in TEP electrolyte was conducted with a three-electrode system with a glassy carbon as working electrode, two Li metal as counter and reference electrode separately.

3.2 Results and discussion

Our first task was to establish a baseline of TEP electrochemical behaviors when Li is used as an electrode. For this purpose, we prepared 1M Li bis(trifluoromethanesulfonyl)imide (LiTFSI) in TEP as an electrolyte and constructed a two-electrode Li||Cu cell that is typically used in the literature for similar studies. In this configuration, Cu serves as the working electrode, and Li is used as both the counter and reference electrodes. As shown in **Figure 3-1**, three reduction peaks were observed at ca. 1.4 V, 1.2 V and 0.5 V (vs. Li/Li⁺; unless noted, all potentials hereafter are relative to this reference) in the first cycle of cyclic voltammetry (CV) scan. Of them, the peak at 0.5 V was ascribed to the reduction of TEP⁹; the peaks at 1.4 V and 1.2 V may report on the reduction of TEP or TFSI⁻. The dominating reduction wave past 0 V is due to Li plating onto the Cu working electrode. On the reverse scan, an oxidation peak at ca. 0.1 V was observed, corresponding to the stripping of the newly plated Li. The broad peak at >1.0 V is believed to be due to re-oxidation of SEI components¹³. Notably, these redox features were quickly suppressed upon repeated CV scans, and they were barely visible after only 5 cycles (**Figure 3-1(a)**). This feature suggests that the Li plating/stripping in TEP-based electrolyte as observed in the initial CV scan is highly irreversible. Correspondingly, when tested in a symmetric Li||Li cell, the system exhibited a rapid increase of the plating and stripping overpotentials (**Figure 3-1(c)**). By the 5th cycle, the plating overpotential already reached -0.75 V, and stripping overpotential reached 1 V. At this point, we considered the test cell has failed. The phenomenon as reported here is consistent with prior reports on TEP electrochemical behaviors when used directly for Li plating and stripping studies¹⁰. It highlights the

challenges of using TEP as a non-flammable electrolyte for safe operations of Li electrodes. Next, we introduced O₂ to the system and observed dramatic improvements. As shown in **Figure 3-1(b)**, the first difference we noticed was the appearance of a new, broad reduction peak at ca. 1.8 V in the Li||Cu cell in the presence of O₂. Presumably, this peak corresponds to the reduction of O₂. While the other reduction features of the first scan were similar to those without O₂, the oxidation peak was indeed more pronounced upon the first reverse scan, reporting a greater recovery of plated Li (ca. 65%) when tested in O₂ than without O₂ (ca. 55%). The most striking difference, however, was how the cell behaved upon repeated CV scans. The Li stripping and plating features were by and large preserved at the 5th cycle (**Figure 3-1(b)**), although the broad peak corresponding to O₂ reduction was now absent. Arguably, the Li stripping peak appeared to be enhanced in comparison to that in the first cycle. These observations led us to conclude that the initial (electrochemical) reactions on the surface of Cu working electrode in O₂-containing TEP electrolyte have resulted in an SEI that favors subsequent Li plating and stripping. To further test this understanding, we next performed cycling tests in a symmetric Li||Li cell. At a current density of 0.5 mA·cm⁻², no apparent increase of the overpotentials (<120 mV) for both plating and stripping of Li was observed after 300 cycles (**Figure 3-1(c)**), at which point the experiment was artificially terminated. Similar results were reproduced for two more times. The excellent cycling performance is comparable to the best reported results using approaches such as high-concentration TEP electrolytes or with nitrate salt additives.

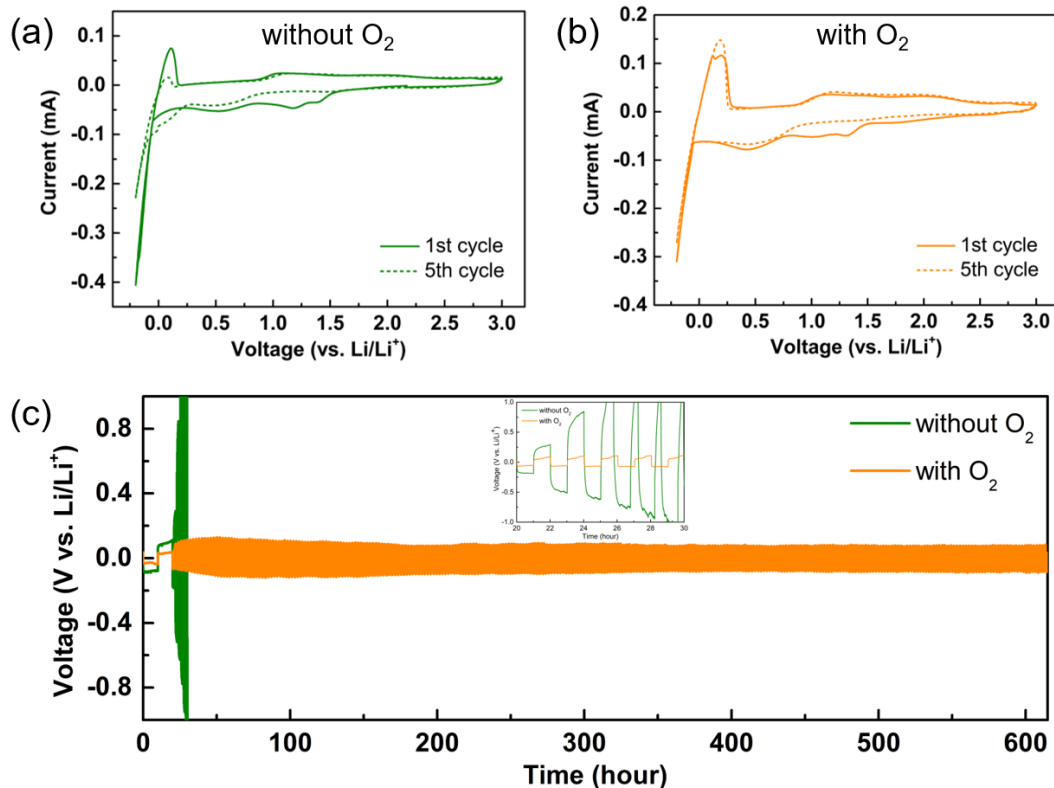


Figure 3-1. Electrochemical performance of TEP electrolyte with or without O₂. CV study of Li||Cu cell with a scan rate of 0.4 mV/s (a) without O₂ and (b) with O₂; (c) Voltage profiles of Li||Li cell for long-term cycling test at a current density of 0.5 mA·cm⁻², limited capacity of 0.5mAh/cm².

How the simple addition of O₂ greatly improves the Li stripping and plating behaviors in TEP-based electrolyte is exciting but also intriguing. To understand the results, we examined the structure of the Cu electrode after the initial plating of Li by scanning electron microscope (SEM). As shown in **Figure 3-2**, with the presence of O₂, a relatively uniform and compact layer of Li with granular microstructures was observed. The grain size was up to 10 μm in diameters. Recent studies have alluded that a desired structure of electrochemically plated Li should retain an even microstructure with large granular sizes and minimum tortuosity; otherwise the loss of "dead" Li would be significant

and, hence, low Coulombic Efficiencies (CE)¹⁴. That we observed such structures by simply adding O₂ to the TEP electrolyte is highly encouraging. In stark contrast, a layer of loose and spikey Li was observed in TEP without O₂, which are typical for Li plating without proper protections of an SEI. Inspired by the prior reports, we hypothesize that the introduction of O₂ has dramatically changed the SEI formation in TEP.

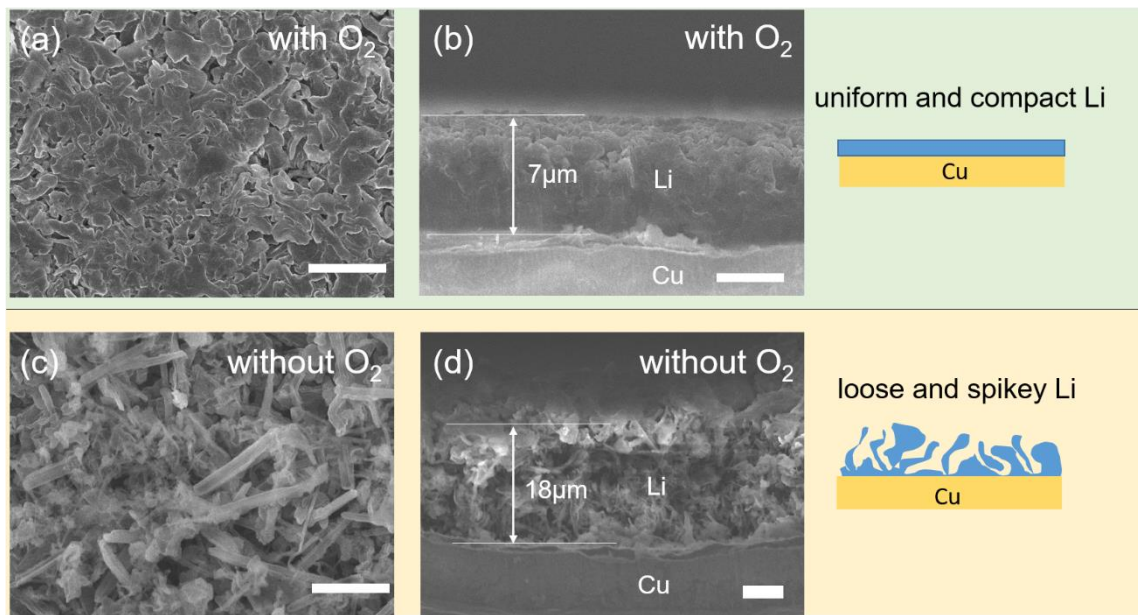


Figure 3-2. Morphology of deposited Li on Cu electrode. SEM images of plated electrodes (a) (b) without O₂ and (c) (d) with O₂. Scale bars: 5 μ m.

As shown in **Figure 3-3**, the presence of O₂ may lead to at least 3 possible reactions on the anode surface: (i) promoted decomposition of TFSI⁻ anions by reduced O₂; (ii) formation of Li₂O on the anode surface; and (iii) electrochemically induced chemical reactions between TEP solvent and O₂ species. These considerations are made with the assumption that electrochemical reduction of O₂ precedes these surface chemical reactions, which is supported by the broad O₂ reduction peak in the CV scan (**Figure 3-1(b)**).

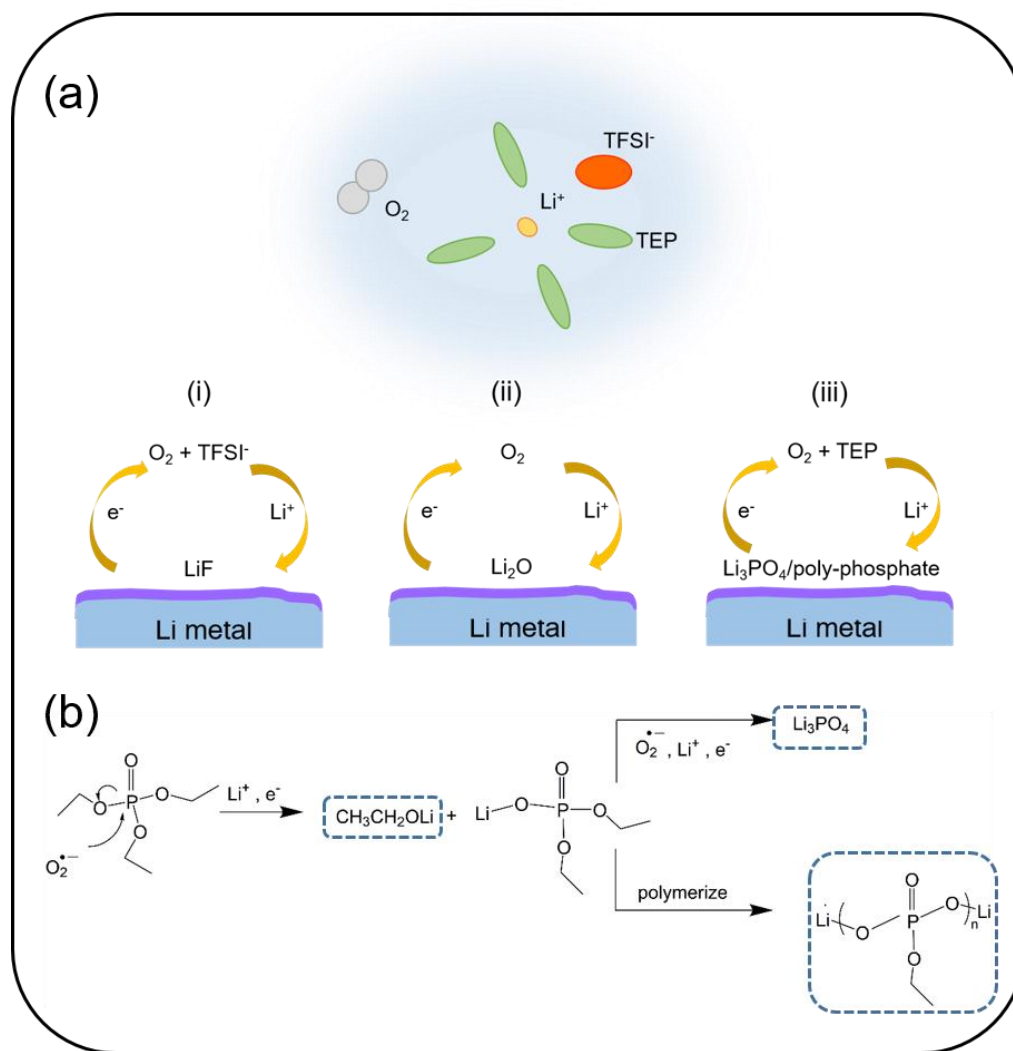


Figure 3-3. Schematic of reaction mechanisms. (a) Three possible reactions on the anode surface; (b) Detailed mechanism of hypothesis (iii), electrochemically induced chemical reactions between TEP solvent and O_2 species to form the Li_3PO_4 or poly-phosphate species.

Next, we examined the first possibility that concerns anion decomposition. Recently, there has been a surge of publications on using high-concentration electrolytes, especially FSI/TFSI-containing ones, to enable reversible Li metal plating/stripping¹⁵. These approaches are based on the premise that the electrolyte decomposition could

produce LiF-rich SEI's that are beneficial for Li plating/stripping. To measure the compositions of the SEI, we collected X-ray photoelectron spectra (XPS) on the Cu working electrode after Li plating. No measurable increase of LiF contents was observed (**Figure 3-4**). Given that the TFSI⁻ concentration is relatively low (1 M), the first possibility of TFSI⁻ decomposition as the main reason for the dramatic increase of the cycling performance is highly unlikely.

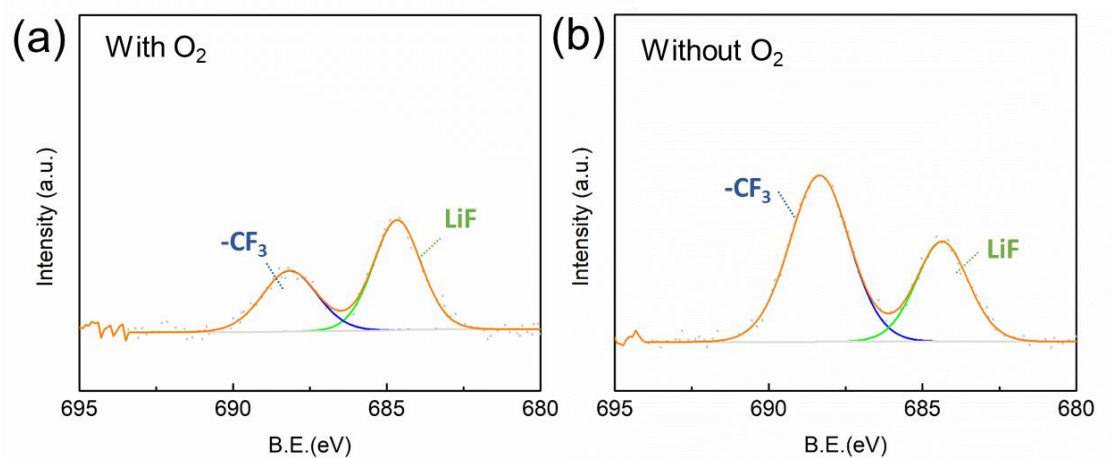


Figure 3-4. XPS F1s spectra of the Li samples after plating Li on the Cu working electrode. (a) with O₂ and (b) without O₂.

To further support this conclusion, we conducted similar cycling experiments as those shown in **Figure 3-1(c)** but with 1 M LiClO₄ (in TEP) as the support electrolyte (**Figure 3-5**). The presence of O₂ clearly exhibited similar effects on enabling the cycling of the symmetric Li||Li test cell. Taken as a whole, the evidence clearly ruled out the first possibility as shown in **Figure 3-3(a)**.

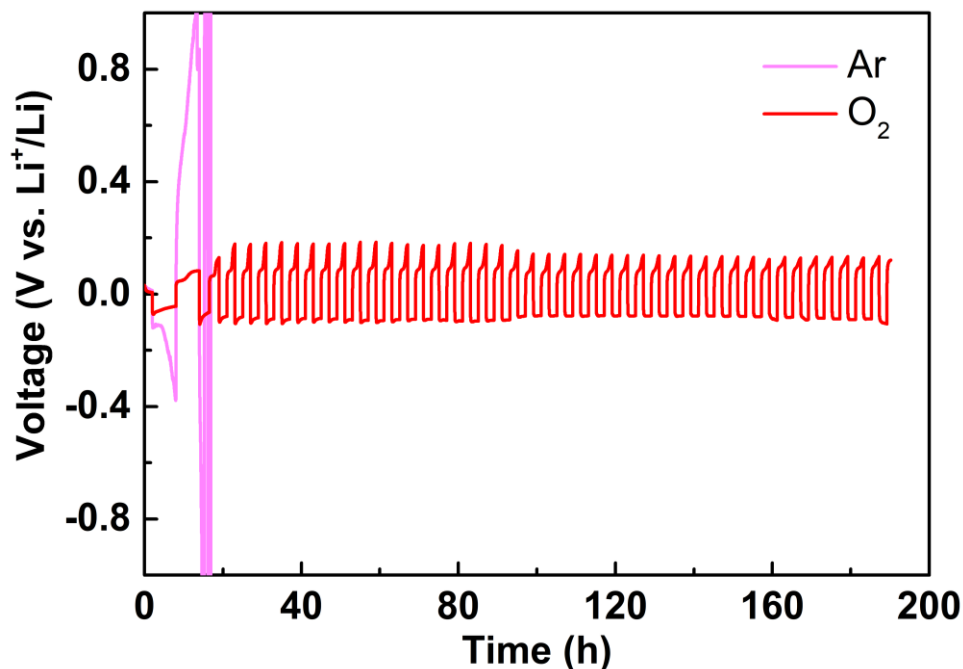


Figure 3-5. Cycling performance of Li||Li cell with 1 M LiClO₄ in TEP electrolyte at a current density of 0.5 mA·cm⁻².

Second, the possibility of Li₂O formation on the anode was considered. Given the presence of O₂ and the low electrochemical potentials of Li oxidation, it is highly conceivable that Li₂O may form on the anode. Recent studies have shown that Li₂O could play a positive role as a component in the SEI¹⁶. To test this possibility, we carried out control experiments by pre-forming Li₂O on Li using two different methods. In the first method, we sought to form Li₂O ex situ by soaking a Li foil in O₂-saturated TEP. Afterwards, the treated Li foil was used as the working electrode in a symmetric Li||Li cell for cycling test. Without O₂ in the TEP electrolyte, the cell failed within 4 cycles (**Figure 3-6(a)**). Similarly, Li foil treated with dry O₂ exhibited Li₂O formation but did not show improvement in cycling tests (**Figure 3-6(b)**). This set of experiments suggest that ex situ Li₂O does not enable Li plating/stripping in TEP.

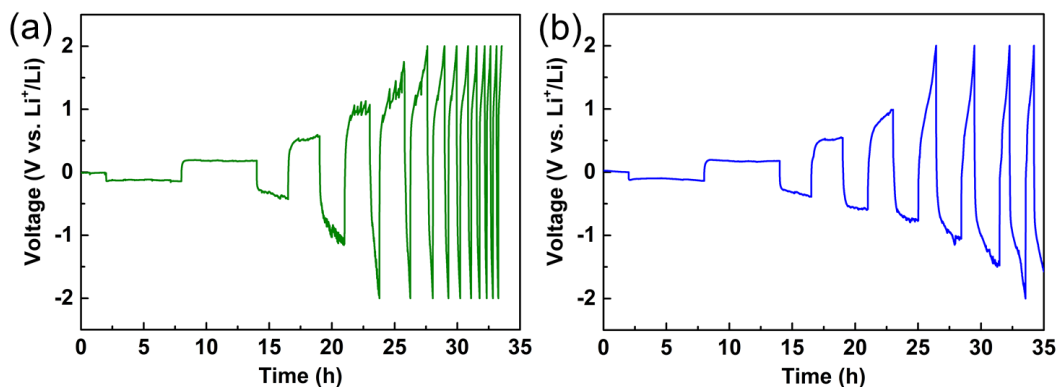


Figure 3-6. Cycling performance of Li||Li cell in LiTFSI-TEP electrolyte with different ex-situ formed Li_2O at a current density of $0.5 \text{ mA} \cdot \text{cm}^{-2}$. (a) ex-situ Li_2O formed by soaking a Li foil in O_2 -saturated TEP (b) ex-situ Li_2O formed by treating Li foil with dry O_2 .

One may argue that in situ formed Li_2O by electrochemistry is necessary for the purpose. To address this concern, we employed the second method of promoting Li_2O formation in a Li||Li cell in an ether-based electrolyte (1M LiTFSI in Tetraethylene glycol dimethyl ether (TEGDME)). After 5 cycles of repeated plating and stripping, a Li_2O -rich SEI was formed on Li surface. The Li foil was then removed from the test cell and washed with 1,2-dimethoxyethane (DME). A new test cell was assembled with TEP as the support electrolyte. Without O_2 , the cell failed quickly after 5 cycles, too (**Figure 3-7**). Taken together, we concluded that the reaction between O_2 and Li cannot account for the observed improvement.

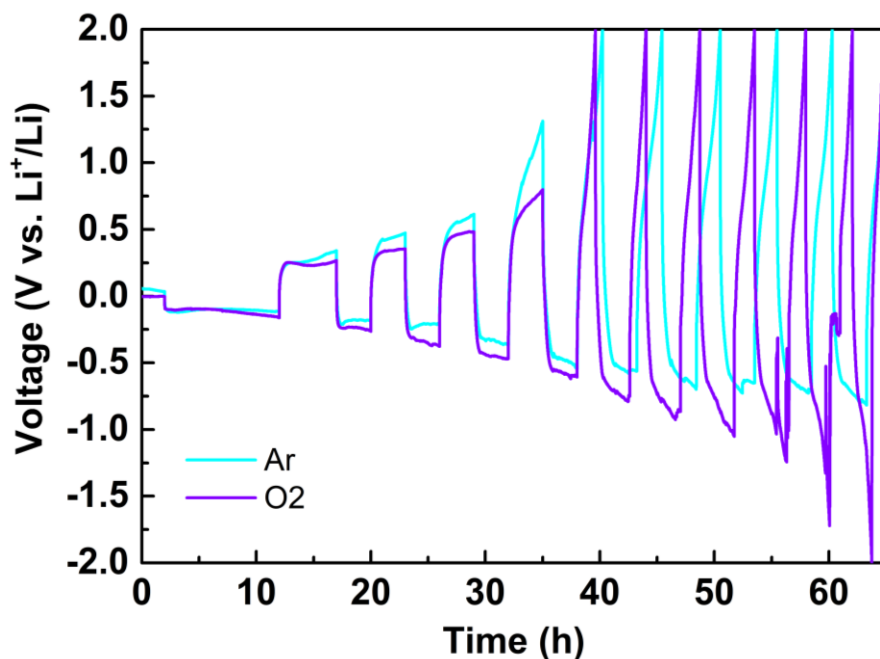


Figure 3-7. Cycling performance of Li||Li cell in LiTFSI-TEP electrolyte with in-situ formed Li_2O at a current density of $0.5 \text{ mA}\cdot\text{cm}^{-2}$.

With the first two possibilities excluded, we are now guided to understand the improvement as a result of the unique reactions between TEP solvent and O_2 species under electrochemical conditions. Close examinations of **Figure 3-1(b)** reveal that O_2 is reduced at potentials $<2.2 \text{ V}$ during the first cycle. As the most likely species of the first electron transfer during oxygen reduction reaction (ORR) in an aprotic electrolyte, $\text{O}_2^{\cdot-}$ is a nucleophile. It can substitute the ethoxy group of TEP via the $\text{S}_{\text{N}}2$ mechanism, as has been reported in the literature¹⁷. Subsequent electron transfer and O-O bond dissociation are expected to lead to the production of Li_3PO_4 or other poly-phosphate products. The hypothesized reaction pathways are illustrated schematically in **Figure 3-3(b)**. If the mechanism holds true, we would expect the release of Li ethoxide ($\text{LiOCH}_2\text{CH}_3$) as a by-product of the first step $\text{S}_{\text{N}}2$ reaction. Indeed, ^1H nuclear magnetic resonance (NMR) spectra clearly confirmed this expectation, where the peak at 3.71 ppm chemical shift may

be assigned to $\text{CH}_3\text{-CH}_2\text{-O-Li}$ (**Figure 3-8(a)**). The relatively low intensity of the signals is due to the low contents of the by-products. A number of reasons contribute to this fact. First, as shown in **Figure 3-1(b)**, the electrochemically induced decomposition of TEP is only significant during the initial CV scans. By the 5th cycle, the reduction wave due to ORR is no longer measurable. As is true for other functional SEI formation, the reaction is self-limiting in nature. Second, the scale of the reaction is small. This is not only because the small size of the electrode ($<1\text{ cm}^2$), but also because the relative thinness of the SEI, which is desired for battery applications. Importantly, no $\text{LiOCH}_2\text{CH}_3$ was detected in the absence of O_2 . The direct decomposition of TEP under electrochemical condition without O_2 is expected to lead to the formation of organolithium compounds (e.g. lithiated phosphates) and inorganic lithium salts (e.g. LiOH), which are poor Li^+ conductors. We next studied the SEI by IR. It is observed in **Figure 3-8(b)** that the introduction of O_2 clearly suppressed the formation of chemicals that give rise to IR peaks at 1048 and 1226 cm^{-1} . According to the literature, they correspond to the stretching of ester group (P-O-R) and P=O, respectively, in organo-phosphorous species¹⁸. The absorption peaks in the range between 1400-1800 cm^{-1} correspond to the C-H bending and C=C/C=O stretching, which may result from direct decomposition of TEP solvent¹⁸. The distinct peak at 952 cm^{-1} reports on the P-O stretching in orthophosphates (PO_4^{3-}) or metaphosphates (PO_3^-)¹⁸. This set of data suggests that direct TEP decomposition produces organo-phosphorous species; the introduction of O_2 alters the reaction pathways to promote the formation of phosphates.

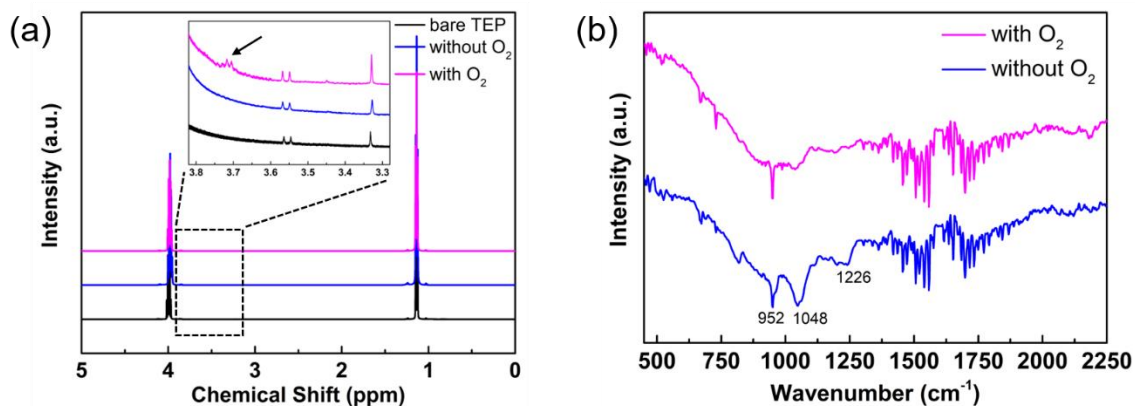


Figure 3-8. (a) NMR spectra of electrolyte solution after cycling; (b) IR spectra of deposited Li on Cu electrode.

It has been reported that Li-conducting Li_3PO_4 SEI layer with a high Young's modulus can effectively suppress side reactions between Li and the electrolyte¹⁹; it also limits Li dendrite growth. Moreover, a dense layer of poly-phosphates is expected to prevent direct decomposition of TEP, in a similar fashion how poly-carbonate in the SEI enables the operation of graphite electrode. We are, therefore, inspired to understand the effects as follows. Electrochemically reduced O_2 leads to the unique decomposition of TEP to yield a thin layer of SEI rich in Li phosphate and polyphosphates. Such an SEI exhibits desired electrical and mechanical properties to regulate Li plating. The net result is that the plated Li is dense and free of dendrites. The stark difference of the plated Li for TEP with and without O_2 (**Figure 3-2**) strongly support this hypothesis. To further validate the conjecture, we performed electrochemical characterization by electrochemical impedance spectroscopy (EIS). Here, the $\text{Li}||\text{Li}$ cell was examined as a function of the cycling history. It is seen in **Figure 3-9** that the initial charge transfer resistance was similar for cells with or without O_2 (ca. 300Ω). After only 1 cycle of Li plating/stripping, the resistance increased dramatically (to ca. 1900Ω) for the cell without O_2 ; in stark

contrast, that for the cell with O_2 did not change significantly. The comparison highlights that direct decomposition of TEP under electrochemical conditions is highly detrimental to Li plating/stripping, consistent with prior reports that organolithium compounds (e.g. lithiated phosphates) and inorganic lithium salts (e.g. LiOH) are poor Li^+ conductors²⁰. In fact, the measured resistance would increase to ca. 2700 Ω after 10 cycles for a cell without O_2 , making it not meaningful to further characterize the cell. The increase of the charge transfer resistance as measured by EIS is consistent with the rapid rise of the overpotentials as shown in **Figure 3-1(c)**. By comparison, repeated plating/stripping of Li in TEP with O_2 gradually decreased the charge transfer resistance to ca. 250 Ω after 40 cycles.

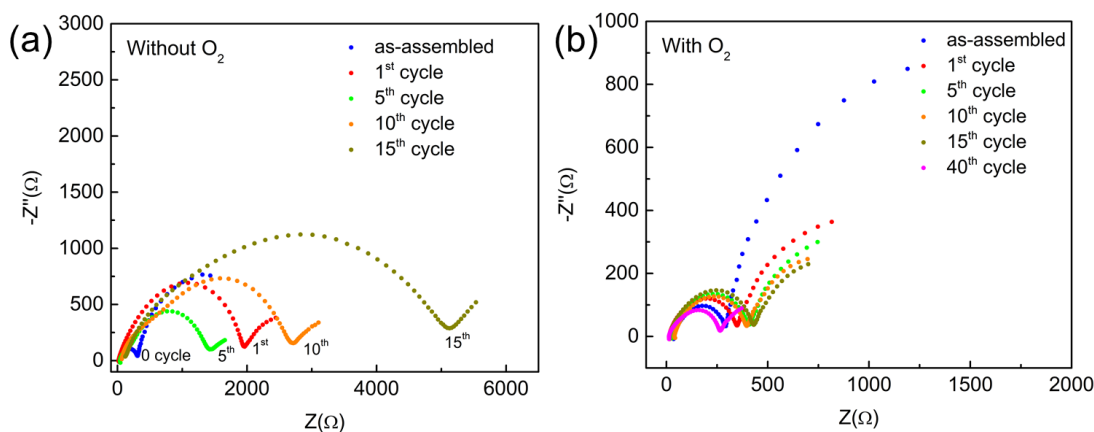


Figure 3-9 EIS results of interfacial resistance during cycling in the Li||Li symmetric cells. (a) without O_2 , (b) with O_2 .

While further research will likely be needed to further reduce the contact resistance for practical applications, the results are encouraging as they are comparable with other literature reports studying Li metal as an anode, particularly in non-flammable phosphate electrolytes. Most encouragingly, the nature of the reaction is such that the resistance actually decreases over cycling, strongly suggesting that a favorable SEI is formed, as is true in other functional SEI formation processes. To the best of our knowledge, this is the

first time that a unique electrochemically-induced electrolyte decomposition pathway is proposed. The mechanism not only enriches the knowledge on the complex reactions that enable the formation of “good” SEI, but also serves as a facile approach to enable the utilization of an otherwise difficult to implement electrolyte. Next, we explored the utility of the as-formed SEI in protecting Li metal as an anode in Li-O₂ and Li-ion batteries.

Given the involvement of O₂ in the above-identified processes, the first prototypical battery we sought to test was Li-O₂ batteries with TEP as an electrolyte. Due to the poor performance of the anode, earlier attempts toward this end have concluded that organic phosphate-based electrolyte was not compatible with Li-O₂ batteries. To prove that the system indeed works, we first studied the electrochemical behaviors of the system in a three-electrode configuration, where glassy carbon was used as the working electrode, and a Li ribbon was used as the counter and reference electrodes. As shown in **Figure 3-10(a)**, the reduction wave took off at ca. 2.6 V, corresponding to the O₂ → Li₂O₂ reaction; on the reverse scan, the oxidation wave was observed starting from ca. 3.0 V, corresponding to the O₂ evolution reaction. The redox features in TEP electrolyte resemble those in ether-based electrolytes, which are well established for Li-O₂ battery operations. Importantly, these electrochemical features were absent without O₂, strongly suggesting that they report on reversible O₂ reduction and evolution in a TEP electrolyte, which is desired but has not been reported previously. Then we fabricated a Li-O₂ full cell for galvanostatic tests. Three dimensionally ordered mesoporous carbon (3DOM) was used as the cathode to take advantage of its good performance for such applications, especially its stability against oxidation²¹. As shown **Figure 3-10(b)**, more than 10 cycles of discharge and recharge were achieved at a current density of 250 mA/g_{carbon} in TEP electrolyte. The cycling

performance is comparable to that in the more popularly studied 1,2-dimethoxyethane (DME) electrolyte under similar test conditions²¹.

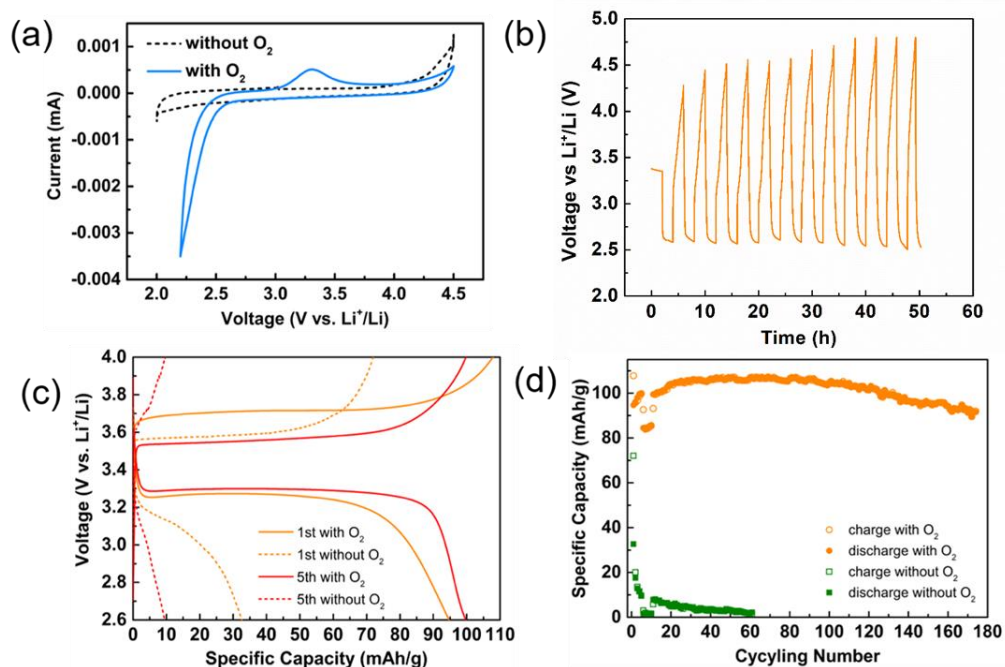


Figure 3-10. (a) CV measured on a glassy carbon working electrode with or without O₂; (b) The voltage profiles of the 3D0m carbon electrode during cycling under constant current (250 mA/g_{carbon}) with a cutoff capacity of 500 mAh/g_{carbon}; (c) Charge-discharge profile of Li||LFP cells with or without O₂; (d) Cycling performance of Li||LFP cells with or without O₂.

To confirm that the electrochemical features indeed report on the formation and decomposition of Li₂O₂ as the discharge product, the morphology of deep-discharged cathode was studied by SEM. **Figure 3-11** shows that a representative toroidal structure was observed, consistent with literature reports where fast kinetics favors toroid formation²².

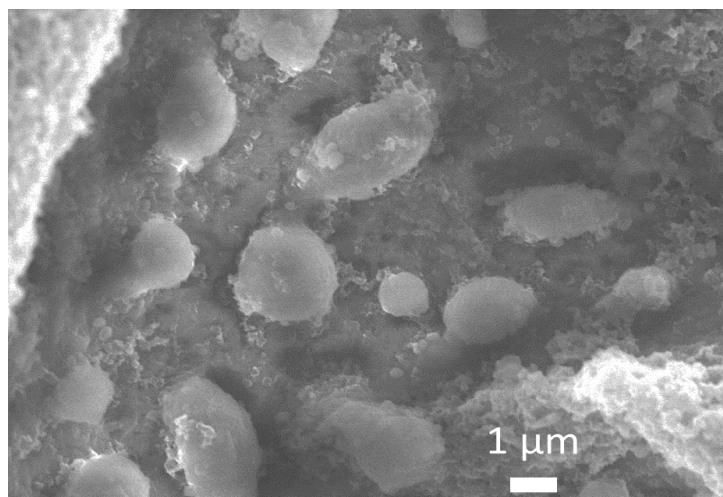


Figure 3-11 SEM image of Li₂O₂ on cathode after discharge.

The Raman spectrum in **Figure 3-12** also proved Li₂O₂ as the discharge product. It is worthy highlighting that the results were obtained by using Li metal as the anode without special protections. This is the first time that a non-flammable phosphate electrolyte is demonstrated for the operation of Li-O₂ batteries. It opens up the door to constructing safe Li-O₂ batteries that could offer high energy densities to fully actualize the potentials held by this new chemistry.

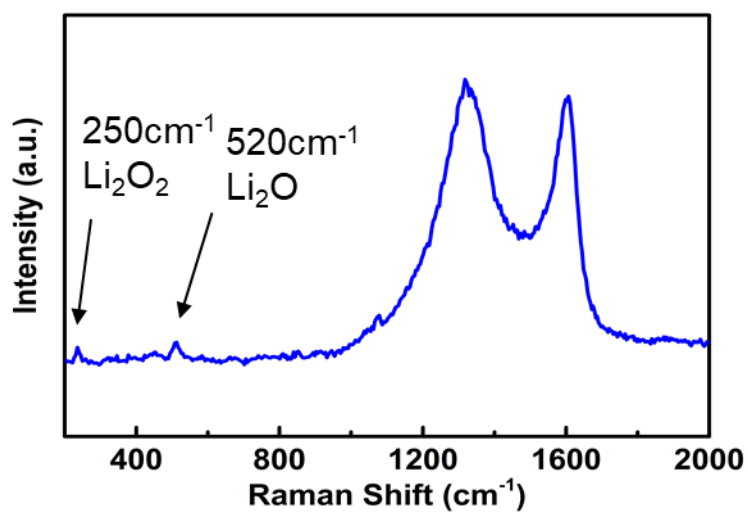


Figure 3-12 Raman spectrum shows the Li₂O₂ on cathode after discharge.

With exciting results on Li-O₂ batteries established, we next tested whether the same strategy works for Li-ion batteries. For this purpose, a full battery consisting of LiFePO₄ (LFP) as the cathode and a Li metal as the anode was fabricated. Stark differences were readily observed in the voltage-capacity profiles as shown in **Figure 3-10(c)** with and without O₂. The presence of O₂ promoted the formation of functional SEI on the Li anode and established stable charge and discharge plateaus at 3.55 V and 3.30 V, respectively, during the first cycle. No stable discharge plateau was observed on the cell without O₂, which quickly worsened even further afterwards, and the cell has practically failed on the 5th cycle. **Figure 3-10(d)** shows that the Li||LFP battery can realized more than 170 reversible cycles with capacity retention of 82% by introducing O₂ as additives. These experiments further demonstrate that our strategy can be utilized to promote the development of Li metal anode in Li-ion batteries and make non-flammable TEP electrolyte as a promising candidate.

3.3 Conclusion

In conclusion, we demonstrate that O₂ as additives can enable Li metal anode operation in non-flammable TEP electrolyte. The significantly different cycling performance and deposited Li morphology results from the electrochemically induced chemical reaction between O₂ species and TEP solvent molecules, which leads the Li-compatible SEI formation and effectively suppresses the TEP decomposition. The promise of safe TEP electrolyte was also demonstrated in Li-O₂ battery and Li-LFP battery. In the future, more

characterization work need to be done to further reveal the details of secondary reaction happened in the electrolyte and how SEI components regulate Li plating/stripping behavior. With better understanding of the system, modification of TEP electrolyte can serve as a promising safe choice to meet the requirements of practical application of Li metal anode.

3.4 References

- (1) Cheng, X.-B.; Zhang, R.; Zhao, C.-Z.; Zhang, Q. Toward Safe Lithium Metal Anode in Rechargeable Batteries: A Review. *Chem. Rev.* **2017**, *117* (15), 10403–10473.
- (2) Zhang, X.; Wang, A.; Liu, X.; Luo, J. Dendrites in Lithium Metal Anodes: Suppression, Regulation, and Elimination. *Acc. Chem. Res.* **2019**, *52* (11), 3223–3232.
- (3) Wang, H.; Liu, Y.; Li, Y.; Cui, Y. Lithium Metal Anode Materials Design: Interphase and Host. *Electrochem. Energy Rev.* **2019**, *2* (4), 509–517.
- (4) Zhang, S. S. Problem, Status, and Possible Solutions for Lithium Metal Anode of Rechargeable Batteries. *ACS Appl. Energy Mater.* **2018**, *1* (3), 910–920.
- (5) Lin, D.; Liu, Y.; Cui, Y. Reviving the Lithium Metal Anode for High-Energy Batteries. *Nat. Nanotechnol.* **2017**, *12* (3), 194–206.
- (6) Zhang, X.-Q.; Cheng, X.-B.; Chen, X.; Yan, C.; Zhang, Q. Fluoroethylene Carbonate Additives to Render Uniform Li Deposits in Lithium Metal Batteries. *Adv. Funct. Mater.* **2017**, *27* (10), 1605989.
- (7) Cheng, X.-B.; Yan, C.; Chen, X.; Guan, C.; Huang, J.-Q.; Peng, H.-J.; Zhang, R.; Yang, S.-T.; Zhang, Q. Implantable Solid Electrolyte Interphase in Lithium-Metal Batteries. *Chem* **2017**, *2* (2), 258–270.
- (8) He, M.; Guo, R.; Hobold, G. M.; Gao, H.; Gallant, B. M. The Intrinsic Behavior of Lithium Fluoride in Solid Electrolyte Interphases on Lithium. *Proc. Natl. Acad. Sci.* **2020**, *117* (1), 73–79.
- (9) Wang, X.; Yasukawa, E.; Kasuya, S. Nonflammable Trimethyl Phosphate Solvent-Containing Electrolytes for Lithium-Ion Batteries: I. Fundamental Properties. *J. Electrochem. Soc.* **2001**, *148* (10), A1058.
- (10) Tan, S.-J.; Yue, J.; Hu, X.-C.; Shen, Z.-Z.; Wang, W.-P.; Li, J.-Y.; Zuo, T.-T.; Duan, H.; Xiao, Y.; Yin, Y.-X.; Wen, R.; Guo, Y.-G. Nitriding-Interface-Regulated Lithium Plating Enables Flame-Retardant Electrolytes for High-Voltage Lithium Metal Batteries. *Angew. Chem. Int. Ed.* **2019**, *58* (23), 7802–7807.

- (11) Wang, J.; Yamada, Y.; Sodeyama, K.; Watanabe, E.; Takada, K.; Tateyama, Y.; Yamada, A. Fire-Extinguishing Organic Electrolytes for Safe Batteries. *Nat. Energy* **2018**, *3* (1), 22–29.
- (12) Fan, W.; Snyder, M. A.; Kumar, S.; Lee, P.-S.; Yoo, W. C.; McCormick, A. V.; Lee Penn, R.; Stein, A.; Tsapatsis, M. Hierarchical Nanofabrication of Microporous Crystals with Ordered Mesoporosity. *Nat. Mater.* **2008**, *7* (12), 984–991.
- (13) Rezvani, S. J.; Nobili, F.; Gunnella, R.; Ali, M.; Tossici, R.; Passerini, S.; Di Cicco, A. SEI Dynamics in Metal Oxide Conversion Electrodes of Li-Ion Batteries. *J. Phys. Chem. C* **2017**, *121* (47), 26379–26388.
- (14) Fang, C.; Li, J.; Zhang, M.; Zhang, Y.; Yang, F.; Lee, J. Z.; Lee, M.-H.; Alvarado, J.; Schroeder, M. A.; Yang, Y.; Lu, B.; Williams, N.; Ceja, M.; Yang, L.; Cai, M.; Gu, J.; Xu, K.; Wang, X.; Meng, Y. S. Quantifying Inactive Lithium in Lithium Metal Batteries. *Nature* **2019**, *572* (7770), 511–515.
- (15) Wang, M.; Huai, L.; Hu, G.; Yang, S.; Ren, F.; Wang, S.; Zhang, Z.; Chen, Z.; Peng, Z.; Shen, C.; Wang, D. Effect of LiFSI Concentrations To Form Thickness- and Modulus-Controlled SEI Layers on Lithium Metal Anodes. *J. Phys. Chem. C* **2018**, *122* (18), 9825–9834.
- (16) Qiu, F.; Zhang, X.; Qiao, Y.; Zhang, X.; Deng, H.; Shi, T.; He, P.; Zhou, H. An Ultra-Stable and Enhanced Reversibility Lithium Metal Anode with a Sufficient O₂ Design for Li-O₂ Battery. *Energy Storage Mater.* **2018**, *12*, 176–182.
- (17) Isbell, D. C.; Dewald, R. R. Kinetic Study of the Reduction of Trimethyl Phosphate, Triethyl Phosphate, and Tributyl Phosphate by Sodium in Liquid Ammonia. *J. Phys. Chem.* **1987**, *91* (27), 6695–6698.
- (18) Eisa, M. Y.; Dabbas, M. A.; Abdulla, F. H. Quantitative Identification of Phosphate Using X-Ray Diffraction and Fourier Transform Infra Red (FT-IR) Spectroscopy. *Int J Curr Microbiol App Sci* **2015**, *4*, 270–283.
- (19) Li, N.-W.; Yin, Y.-X.; Yang, C.-P.; Guo, Y.-G. An Artificial Solid Electrolyte Interphase Layer for Stable Lithium Metal Anodes. *Adv. Mater.* **2016**, *28* (9), 1853–1858.
- (20) Lu, J.; Jung Lee, Y.; Luo, X.; Chun Lau, K.; Asadi, M.; Wang, H.-H.; Brombosz, S.; Wen, J.; Zhai, D.; Chen, Z.; Miller, D. J.; Sub Jeong, Y.; Park, J.-B.; Zak Fang, Z.; Kumar, B.; Salehi-Khojin, A.; Sun, Y.-K.; Curtiss, L. A.; Amine, K. A Lithium–Oxygen Battery Based on Lithium Superoxide. *Nature* **2016**, *529* (7586), 377–382.
- (21) Xie, J.; Yao, X.; Cheng, Q.; Madden, I. P.; Dornath, P.; Chang, C.-C.; Fan, W.; Wang, D. Three Dimensionally Ordered Mesoporous Carbon as a Stable, High-Performance Li–O₂ Battery Cathode. *Angew. Chem. Int. Ed.* **2015**, *54* (14), 4299–4303.
- (22) Dong, Q.; Yao, X.; Zhao, Y.; Qi, M.; Zhang, X.; Sun, H.; He, Y.; Wang, D. Cathodically Stable Li-O₂ Battery Operations Using Water-in-Salt Electrolyte. *Chem* **2018**, *4* (6), 1345–1358.

Chapter 4. Metal-Organic Framework thin film for selective Mg²⁺ transport

[This chapter is adapted with permission from “Luo, J.; Li, Y.; Zhang, H.; Wang, A.; Lo, W.-S.; Dong, Q.; Wong, N.; Povinelli, C.; Shao, Y.; Chereddy, S.; Wunder, S.; Mohanty, U.; Tsung, C.-K.; Wang, D. A Metal–Organic Framework Thin Film for Selective Mg²⁺ Transport. *Angewandte Chemie International Edition* **2019**, *58* (43), 15313–15317. <https://doi.org/10.1002/anie.201908706>.” Copyright (2019) John Wiley and Sons.]

In the quest for post-Li-ion battery electrochemical energy storage technologies, Mg-battery stands out for its low cost and no dendritic growth upon plating.¹ Indeed, recent years have witnessed a growing body of reports on realizing the full potential of Mg batteries.² This exciting progress notwithstanding, existing demonstrations face important issues, the most significant of which concerns the incompatibility of the anode and the cathode chemistries.^{2c,3} That is, the types of electrolytes and chemical reactions desired for the anode reactions are often incompatible with those for the cathode and vice versa. Considering the Mg-S battery as an example, for successful practical conversion at the cathode, high potentials (for example, >3.5 V vs. Mg/Mg²⁺) are often needed owing to the kinetic overpotential requirements,⁴ but electrolytes that could be used for such processes (for example, organic carbonate-based ones), would form an inert passivation layer on the Mg anode, which would greatly increase the overpotentials for Mg stripping and plating.⁵ Conversely, chemicals such as Grignard reagents enable facile Mg stripping and plating on a Mg anode but would react with S to form phenyl disulfide and biphenyl sulfide.^{3a} Similar issues were encountered in emerging Mg-Br₂ and Mg-O₂ batteries as

well.^{2c, 2e} While some potentially promising solutions have been proposed, using, for example, non-nucleophilic electrolytes such as Mg(TFSI)₂ (where TFSI is bis(trifluoromethanesulfonyl)imide),^{4, 6} Mg/AlCl_x complexes⁷ and (HMDS)₂Mg+AlCl₃ (where HMDS stands for bis(trimethylsilyl) amine) in ethereal solvents,⁸ these electrolytes either suffer from poor stability with the Mg anode or severely corrode current collectors.^{3b} A broadly applicable strategy to solve this issue is needed to push the field forward.

One solution to this problem lies in a separator that permits selective Mg²⁺ transport but separate the anolyte and the catholyte,^{2c} so as to greatly broaden the choices for each respective chemical process (**Figure 4-1**). Solid-state electrolytes⁹ and polymer electrolytes¹⁰ have been explored to serve as such separators. However, they either feature extremely low room temperature conductivity of 10⁻¹²–10⁻⁸ S cm⁻¹,^{9c} or the lack of durable selectivity due to, for example, the structural changes caused by the swelling of the polymers,¹¹ which made them less than ideal for practical applications.

A third class of materials that have been explored for the purpose of selective ionic transport is metal–organic frameworks (MOFs).¹² MOFs feature well-defined porous structures that could be ideal for selective ionic transport.¹³ Indeed, MOFs have been exploited for the transport of protons (H⁺),¹⁴ Li⁺,¹⁵ and Na⁺,¹⁶ and promising results have been published.¹⁷ Just within the context of Mg²⁺ transport, MOFs have been examined by Long et al. and Dinca et al., separately.^{15c, 17b, 18} Mg²⁺ conductivity up to 2.5×10⁻⁴ S cm⁻¹ has been reported.¹⁸ Nevertheless, these pioneering studies often employed pressed pellets of MOF powders to bring the fundamental understanding; except in rare cases where low resistance was specifically reported,¹⁸ pressed pellets often featured resistances

(>5,000 Ω) that are too high for practical applications. Furthermore, there are inevitable gaps between adjacent particles in a pressed pellet, which makes it exceedingly difficult to understand the true behavior of MOFs as selective ionic conductors.¹⁹ Clearly, there is a need to fill the gap in research on selective Mg^{2+} transport by MOFs. Herein we show that this need may be met by MOF thin films, which were synthesized on a membrane that can be readily utilized.²⁰ It also eliminates interparticle gaps that are abundant in pressed pellets. Such a feature may become important in the future because it would enable studies on the inherent ionic transport properties of MOFs without confounding factors such as inadvertent transport through the gaps.

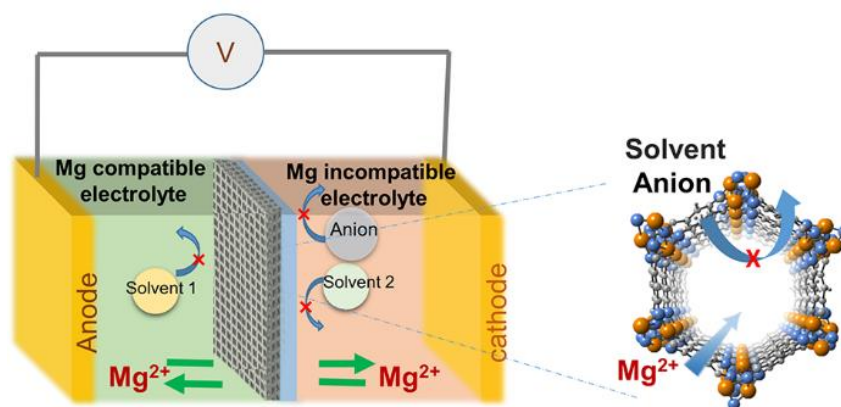


Figure 3-1. Schematic illustration of how MOF film may be used in a hybrid battery for selective transport of Mg^{2+} , where Mg metal serves as the anode and a high-potential Mg-storage materials (*e.g.*, S or O_2) as the cathode. The incompatible anolyte and catholyte (with high anodic stability) could be separated by a MOF membrane.

4.1 Experimental procedures

Chemicals and materials: MgCl_2 , dimethoxyethane(DME), bis(2-methoxyethyl) ether (diglyme) and propylene carbonate (PC) (all anhydrous grade) were purchased from Sigma-Aldrich. Mg metal (Ribbon, $\geq 99\%$ trace metals basis, Sigma-Aldrich) was scraped by a blade to remove the surface passivation layer before usage. $\text{Mg}(\text{TFSI})_2$ was purchased from Solvionic. Magnesium nitrate hexahydrate ($\text{Mg}(\text{NO}_3)_2 \cdot 6\text{H}_2\text{O}$, Sigma-Aldrich, 99%), 2,5-dihydroxyterephthalic acid (Alfa Aesar, 98%), acetic acid (Sigma-Aldrich, $\geq 99.7\%$), sodium hydroxide (Alfa Aesar, 97.0%), dimethylformamide (DMF, Alfa Aesar, 98%), dimethyl sulfoxide-D6 (DMSO-D6; D, 99.9%, Cambridge Isotope Laboratories, Inc.), difluoroacetic acid (Sigma-Aldrich, $\geq 97.0\%$), hydrochloric acid (Fisher), were used without further purification unless otherwise stated. Ultrapure deionized water (DI H_2O , 18.2 $\text{M}\Omega$) was used for aqueous solution preparation. Free-standing anodic aluminum oxide wafers (size: 13 mm, thickness: 100 μm , pore size: 80 nm in diameter) were purchased from Inredox Materials Innovation.

Instrumentation: Scanning electron microscopy (SEM) was performed on a JEOL JSM-6340F and JEOL JSM-7001F scanning electron microscope. Powder X-ray diffraction (PXRD) patterns were collected on a Bruker D2 diffractometer with $\text{Cu K}\alpha$ radiation ($\lambda=1.5418 \text{ \AA}$). AJA International Orion 8 sputter deposition system was applied to make substrate. An adhesive layer of Ti or Cr with 5 nm was firstly sputtered on Si wafer, and then a thin layer of Au with 50 nm was sputtered. ^1H NMR and ^{19}F NMR spectra were collected on a Varian Unity INOVA spectrometers (500 MHz, or 600 MHz) with chemical shifts reported in ppm. Mg plating/stripping and CV measurements were performed in an

Argon glovebox (Mbraun, O₂ and H₂O <0.1 ppm) at room temperature and data collected on a VMP3 BioLogic potentialstat. Impedance spectra were recorded by using a ModuLab® XM potentiostat. The EIS data were measured by a 25 mV perturbation from 1MHz to 0.1 Hz. The atomic force microscopy (AFM) measurement was performed using ezAFM equipment (Nanomagnetic Instruments), with BM-10 Bench Top Vibration Isolation Platform (Minus K Technology). The images were taken with 512x512 Pixel resolution.

Mg-MOF-74 thin film synthesis: The substrate was washed by acetone, methanol and isopropanol by sonication in sequence before use. In an autoclave, substrate (1 cm x 1 cm) was placed on a cuboid teflon holder (1 cm x 1 cm x 1 cm). 50 µL of precursor solution, made by dissolving 2,5-dihydroxyterephthalic acid (0.0606 mmol), magnesium nitrate hexahydrate (0.545 mmol), acetic acid (0.303 mol) and sodium hydroxide (0.439 mmol) in the 13 mL mixture of DMF, ethanol and water (volume ratio: 1:1:1), was added on the substrate. 4 mL mixture of DMF, ethanol and water (volume ratio: 12:1:1) was added in autoclave, which would not reach the substrate. Then the autoclave was sealed and put in the oven that was preheated to 100°C for 24 h. Then the as-synthesized film was taken out washed by DMF and methanol.

Mg-MOF-74/AAO: The synthesis of MOF-74/AAO was similar to the synthesis MOF-74 thin film on Au/Si. An AAO substrate was washed with methanol before use. 75 µL of precursor solution (same as MOF-74 thin film) was added on the AAO. The following methods are the same as the synthesis of MOF-74 thin film.

Solvent Exchange and Activation of Mg-MOF-74 thin film: Sample was soaked in methanol and change with fresh methanol every 3 h. The solvent exchange continues two

days. And then the sample was placed under 150 °C in vacuum oven for 3 d before any measurements.

Electrochemical measurements: The exposed portion of the Au contact was connected to a wire using silver paste. Silver paste was cured at 80 °C for 30 min. The surface was further covered by an insulating epoxy resin but leaving a small area (3 mm in diameter) of MOF exposed. The epoxy resin was cured at 80 °C for 15 min.

For Fc measurements, 1 mM Fc was dissolved in 10 mL acetonitrile with 0.1 M TBAP6F as the supporting electrolyte. Mg-MOF-74/Au was used as the working electrode (exposed area was ~3 mm in diameter). FTO (Fluorine-doped tin oxide) was used as counter electrode (~1 cm² immersed into the solution). Ag/AgCl was used as the reference electrode. In glove box, cyclic voltammograms were conducted with a scan rate of 50 mV/s. The voltage range was -0.3 V– 0.5 V vs. Ag/AgCl.

For CoTPP measurements, 1 mM CoTPP was dissolved in 10 mL DMSO with 0.1 M TBAP6F as the supporting electrolyte. Mg-MOF-74/Au was used as working electrode. FTO was used as counter electrode (~1 cm² immersed into the solution). Pt was used as reference electrode. CV scans were conducted with a scan rate of 50 mV/s. The voltage range was -1.0 V – 1.0 V vs. Pt.

Conductivity measurements: The Mg salts were filled into the MOF-74 thin film by electric field. The Mg-MOF-74/Au was employed as working electrode and it was exposed to in 0.25 M Mg(TFSI)₂ / 0.5 M MgCl₂ /DME liquid electrolyte with applied potential (-0.5 V) for 4h to uptake Mg²⁺ before usage (two Mg stripes were used as the counter electrode and the reference electrode, respectively). A Swagelok cell was used in the EIS measurement. The Au blocking electrode was connected to the cell with silver paste. The

Cu foil was used as the other blocking electrode with a contact area of *ca.* 0.5 cm². A thin layer of Mg²⁺-conducting ion-gel electrolyte (prepared in a 90/10 weight ratio of EMIMTFSI ionic liquid and methyl cellulose with 0.25M Mg(TFSI)₂ salt) was placed between Cu and Mg-MOF-74 to ensure the contact. An alternating current (AC) voltage was applied between the two electrodes with the frequencies varying between 0.1 Hz and 1 MHz. After the EIS measurement, the Mg-MOF-74/Au electrode was taken out and etched by 0.5 M HCl for 2 h to fully dissolve the Mg-MOF-74 layer. After drying, the electrode was subjected to the same EIS measurements with only the ion-gel electrolyte in between the two blocking electrodes. All cell assemblies were performed in a glovebox (Mbruan, O₂ and H₂O < 0.1 ppm) at room temperature.

The conductivities at different temperature were obtained by same method as described above. The Swagelok cell was rested at the certain temperature for over 2 hours before the EIS measurement. The temperature ranged from 25°C to 65°C. The activation energy (E_a) was calculated using the equation $\sigma_T = \sigma_o \exp(-E_a/k_B T)$, where σ_T is the conductivity, σ_o is the pre-exponential parameter, T is absolute temperature, E_a is the activation energy, and k_B is the Boltzmann constant.

The EIS data of MOF/AAO was measured with two stainless steel as blocking electrodes in H-cell with dual electrolytes. The contact area is 0.196 cm². An AC voltage was applied between the two blocking electrodes with the frequencies varying between 0.1 Hz and 1 MHz.

Mg asymmetric cell measurements: Three different Mg stripes were used as the working electrode, the counter electrode and the reference electrode, respectively. MgCl₂ (0.1 M) and AlCl₃ (0.1 M) were dissolved in DME as the anolyte. Mg(TFSI)₂ (0.1 M) was

dissolved in diglyme as the catholyte. The volumes of the electrolytes were both 2 mL in each chamber. The two electrolytes were separated by a Mg-MOF-74 /AAO membrane. All electrochemical measurements were performed in a glovebox (Mbruan, O₂ and H₂O < 0.1 ppm) at room temperature.

Solvent (Diglyme and PC)/TFSI⁻ blocking capability measurements: 0.1 M Mg(TFSI)₂ dissolved in PC was placed on one side of the Mg-MOF-74/AAO separator in an H-cell. Pure diglyme was placed on the other side of the H-cell with Mg-MOF-74/AAO placed between as a separator. For NMR analysis on the diglyme side, 20 μL solvent was taken out. Then it was mixed with 600 μL DMSO-D6 and 3 μL F₂CHCOOH (as a comparison in ¹⁹F NMR). For the NMR analysis on the PC side, 20 μL solvent was taken out and mixed with 600 μL DMSO-D6.

4.2 Results and discussion

In this work, we chose Mg-MOF-74 as a study platform.²¹ With parallel 1D hexagonal pores of single-type apertures about 13 Å in diameter, Mg-MOF-74 consists of coordinatively unsaturated Mg²⁺ cations as the inorganic building blocks.²² These open metal sites can potentially coordinate with multidentate anions and solvent molecules to facilitate Mg²⁺ transport.^{15a, 18} To examine the conductivity and selectivity of Mg²⁺ transport in Mg-MOF-74, we used a wet-chemistry approach to grow a thin film (ca. 202 nm) on a Si wafer sputtered with a thin Au layer (ca. 50 nm) that served as a conductive contact (**Figure 4-2**).

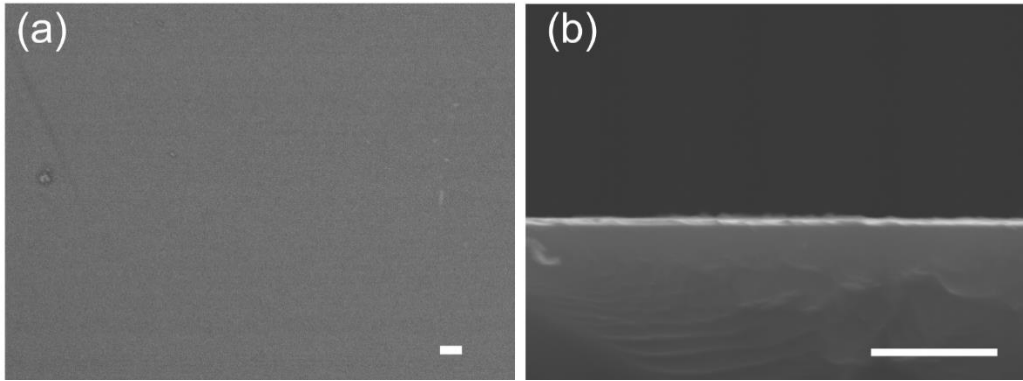


Figure 4-2. (a) Top-view and (b) cross-sectional SEM images of Au-coated Si wafer. Scale bars: 1 μm .

X-ray diffraction (XRD) patterns of the resulting film showed two characteristic peaks that could be assigned to $(2\bar{1}0)$ and (300) of Mg-MOF-74, in good agreement with the simulated data (**Figure 4-3 (c)**). The morphology of the film was observed by scanning electron microscopy (SEM). As shown in **Figure 4-3 (c)**, uniform coverage of the film was achieved. The cross-sectional side view configuration revealed that the film was uniform across the viewing field with a thickness of about 202 nm on a thin layer of Au (**Figure 4-3(b)**). The uniformity of the film was also characterized by atomic force microscopy (AFM; **Figure 4-4**), where the root mean square roughness (R_q) was calculated as 4.40 nm.

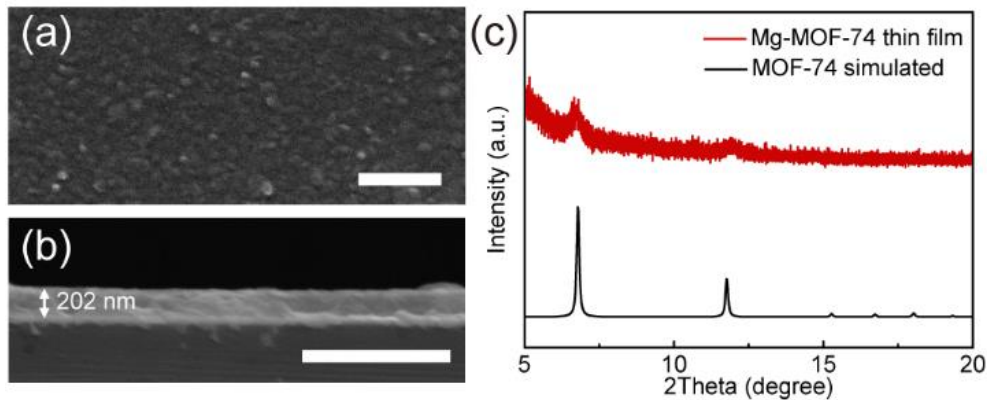


Figure 4-3. Structural characterization of the Mg-MOF-74 thin film. (a) Top-view SEM image. Scale bar: 1 μm . (b) Cross-section SEM image of Mg-MOF-74 film on a Si wafer sputtered with a thin Au layer (*ca.* 50 nm). Scale bar: 1 μm . (c) XRD patterns of MOF-74 thin film and a comparison with simulated data.

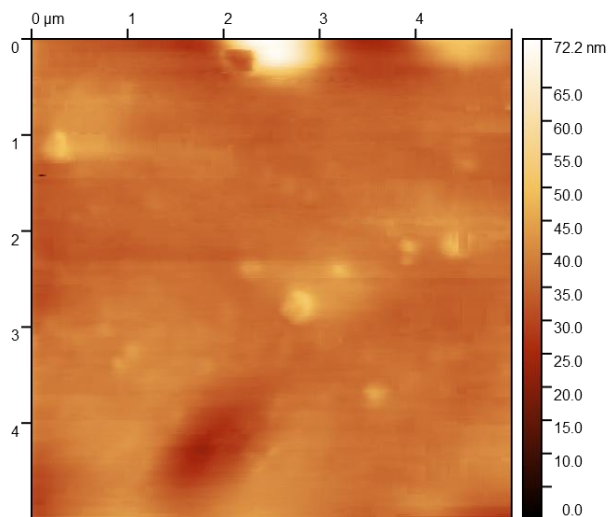


Figure 4-4. Top-view AFM image of Mg-MOF-74 thin film on Au.

Next, the electrochemical properties of the MOF thin film were studied. Our first goal was to show that the coverage of the resulting Mg-MOF-74 thin film on Au-coated Si was complete, and the film was crack-free. For this purpose, Co tetraphenylporphyrin (CoTPP) was employed as a probe redox specie, which is 19 Å in diameter,²³ larger than the pore of Mg-MOF-74 at 13 Å. As expected, a featureless cyclic voltammogram (CV) between -1.0 and +1.0 V (vs. Pt reference; see the Supporting Information for experimental details) was recorded. In stark contrast, the same electrolyte would yield two pairs of distinct redox peaks on a bare Au electrode (**Figure 4-5(a)**), corresponding to the reversible $\text{Co}^{\text{I}} \leftrightarrow \text{Co}^{\text{II}}$ and $\text{Co}^{\text{II}} \leftrightarrow \text{Co}^{\text{III}}$ conversion, respectively.^{2c} This set of data showed that our film is crack-free and electronically insulating. When the redox specie was switched to ferrocene, whose diameter is 6.6 Å,²⁴ a clean pair of redox peaks characteristic

of the $\text{Fe}^{\text{II}} \leftrightarrow \text{Fe}^{\text{III}}$ conversion were observed (**Figure 4-5(b)**). Together with the CoTPP experiments, the data supported that Mg-MOF-74 permits size-selective transport of ions/molecules.

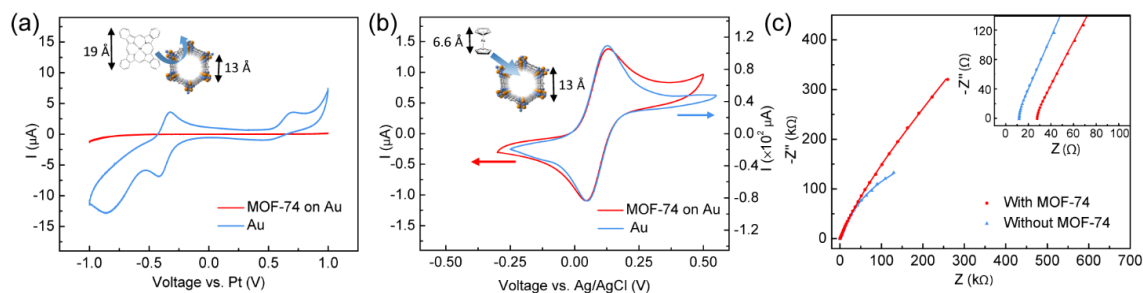


Figure 4-5. Electrochemical properties of the Mg-MOF-74 thin film. (a) Cyclic voltammograms in 1 mM CoTPP or (b) 1 mM ferrocene with bare gold substrate or MOF-74 film on Au-coated Si. (c) Electrochemical impedance spectra measured on Au with and without MOF with the magnified view (inset) at the high frequency end.

To further understand the behavior of Mg-MOF-74 as a candidate for selective Mg^{2+} transport, we carried out electrochemical impedance spectroscopic (EIS) experiments using a solid|ion-gel²⁵ hybrid cell as schematically illustrated in **Figure 4-6**. Here a hybrid cell was chosen for convenience, so that a reliable contact can be made with the MOF thin film without shorting the circuit. An alternating current (AC) voltage was applied between the two electrodes with the frequencies varying between 0.1 Hz and 1 MHz.

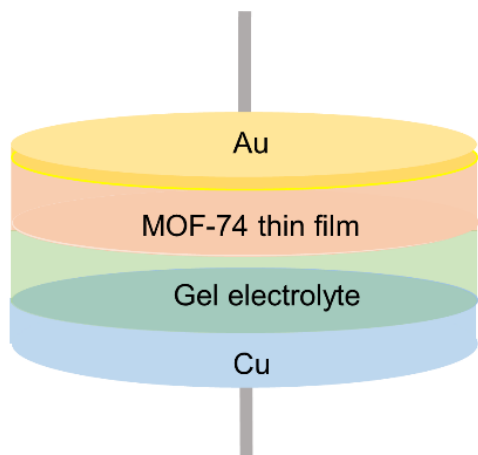


Figure 4-6. The cell configuration of the conductivity measurement.

As can be seen from **Figure 4-5(c)**, the high-frequency intersection of the Nyquist plot with the x axis reported on the bulk ionic resistance of the materials. And the Bode plots in **Figure 4-7** also showed the impedance plateau at high frequency that was characteristic of bulk ion conduction.

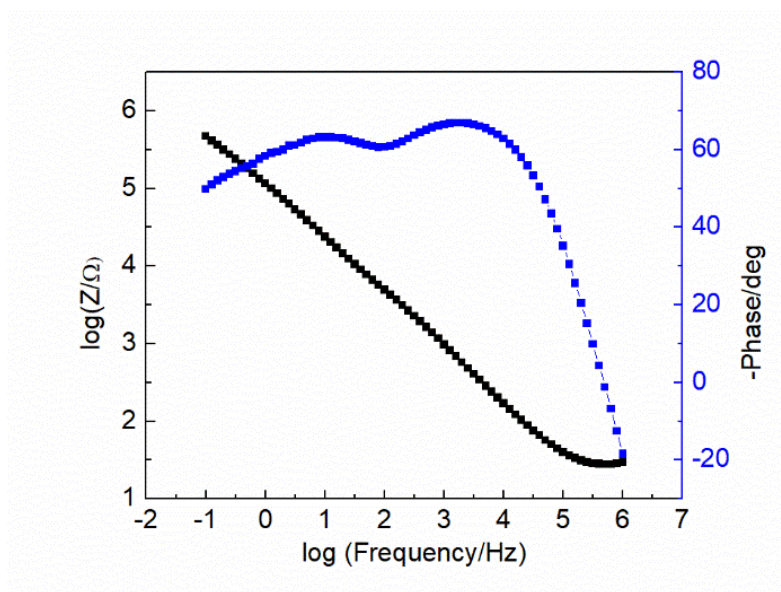


Figure 4-7. Bode plots of MOF thin film at room temperature.

Without the Mg-MOF-74, the value was 13.4Ω , corresponding to the ionic resistance of the ion gel and the resistance of the whole setup; with Mg-MOF-74, a resistance of 25.6Ω was recorded. The difference (ca. 12Ω) was attributed to the resistance of the thin Mg-MOF-74 film. Given that the film thickness was 202 nm (**Figure 4-3(b)**) and using the measured cross-sectional area of 0.52 cm^2 , we calculated the conductivity as about $3.17 \times 10^{-6} \text{ S cm}^{-1}$. It is in the same range as reported previously, where the MOF-74 was used as a solid electrolyte ($1.58 \times 10^{-6} \text{ S cm}^{-1}$).¹⁸ It is also worth noting that the value reported previously was measured on pressed pellets which were rich in voids between grains. To what extent these gaps and voids contribute to the measured conductivity will require further research to understand. Our CoTPP electrochemical study showed that our measured values have no such contribution. We are, therefore, confident that the normalized resistivity represents the inherent properties of Mg-MOF-74. The activation energy of the Mg-MOF-74 thin film was 0.53 eV (**Figure 4-8**).

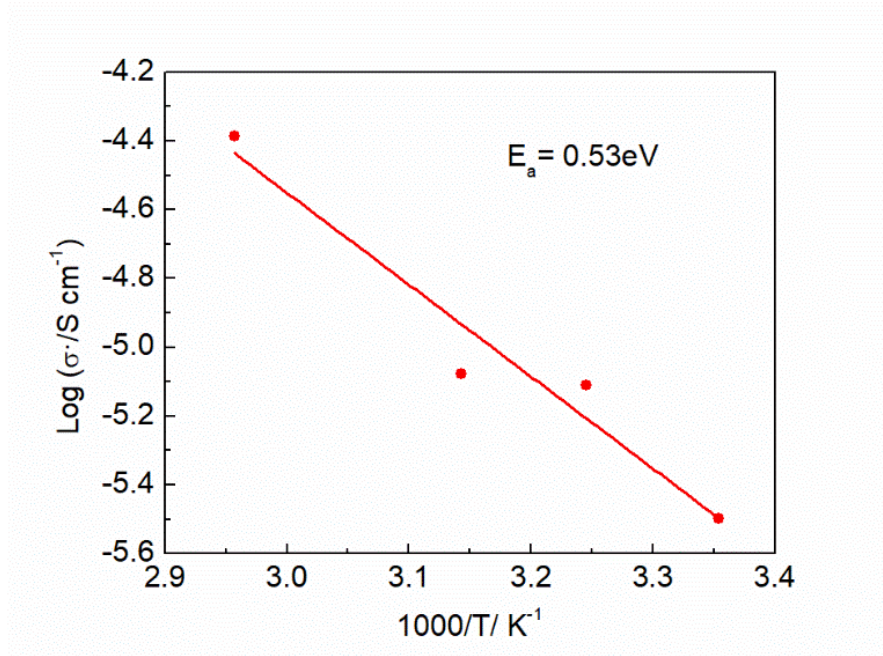


Figure 4-8. Arrhenius plots of the Mg-MOF-74 thin film.

With the inherent transport properties understood, our next task was to examine whether Mg-MOF-74 permits selective Mg^{2+} transport. An asymmetric cell as depicted in **Figure 4-9** was employed. It consisted of a Mg strip as the anode, a mixture of MgCl_2 (0.1 m), AlCl_3 (0.1 m) and DME as the anolyte, and another Mg strip as the cathode with $\text{Mg}(\text{TFSI})_2$ (0.1 m) in bis(2-methoxyethyl) (diglyme) as the catholyte. The two electrodes were separated by a film made of Mg-MOF-74 directly grown on an anodized aluminum oxide (AAO) porous support via the same wet-chemistry procedure. Here AAO served as a non-conductive porous support to provide the needed mechanical strength to the MOF thin film. To accurately measure the potentials of the working electrode (that is, the anode), we also introduced a third Mg strip in the working electrode chamber as a reference. In operating this cell, our goals were threefold. First, we expected to test whether Mg^{2+} can be transported through the Mg-MOF-74 thin film reliably under electrochemical conditions. Second, we hoped to study whether the Mg-MOF-74 thin film was effective in blocking solvent molecules from crossing over. Third, we wished to monitor whether the anions (for example, TFSI^-) could be blocked by Mg-MOF-74.

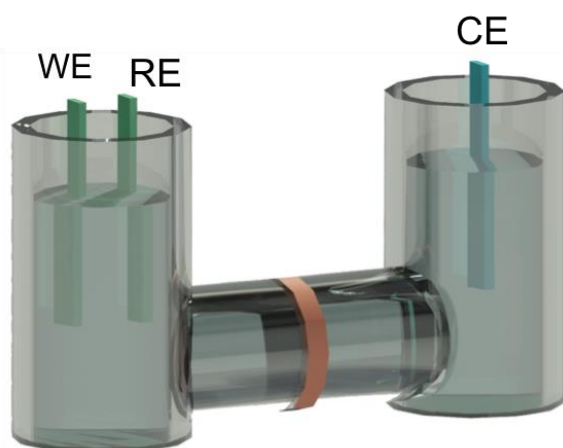


Figure 4-9. Schematics of the 3-electrode cell configuration.

As shown in **Figure 4-10**, the Mg plating process took place at about -0.15 V (vs. Mg^{2+}/Mg ; unless noted, all potentials are relatively to this reference), whereas the potential for Mg stripping was ca. 0.10 V. These electrochemical features are comparable to literature reports in similar electrolytes.⁷ In contrast, the overpotential was ca. 0.5 V with a bare AAO as a separator. The increased overpotential could come from severe crossover of TFSI^- from catholyte to anolyte which would passivate the Mg electrode.^{3b, 26}

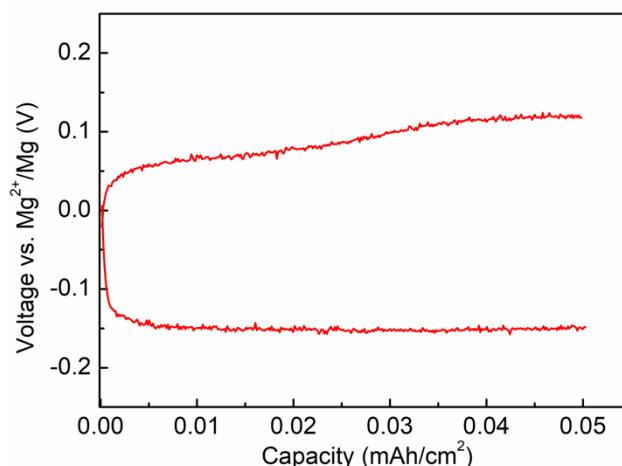


Figure 4-10. Mg plating/stripping data as measured in an asymmetric cell with Mg-MOF-74/AAO as the separator. The Mg plating process took place at ca. -0.15 V (vs. Mg^{2+}/Mg), whereas the potential for Mg stripping was ca. 0.10 V (vs. Mg^{2+}/Mg).

The cycled Mg working electrodes were characterized by SEM. As shown in **Figure 4-11**, the morphologies of cycled Mg were similar in cells either with bare AAO or with MOF/AAO separator. However, the surface components varied according to the X-ray photoelectron spectroscopy (XPS) spectra (**Figure 4-12**). Compared with the MOF/AAO system, the cycled Mg working electrode with the bare AAO separator contained more MgCO_3 , MgF_2 , N and S components that were likely owing to TFSI^- decomposition.²⁷ This evidence proved that the Mg electrode was less passivated by

TFSI⁻ with the MOF/AAO separator than with only the AAO separator, leading to lower overpotentials in the Mg plating/stripping experiments, which is desired.

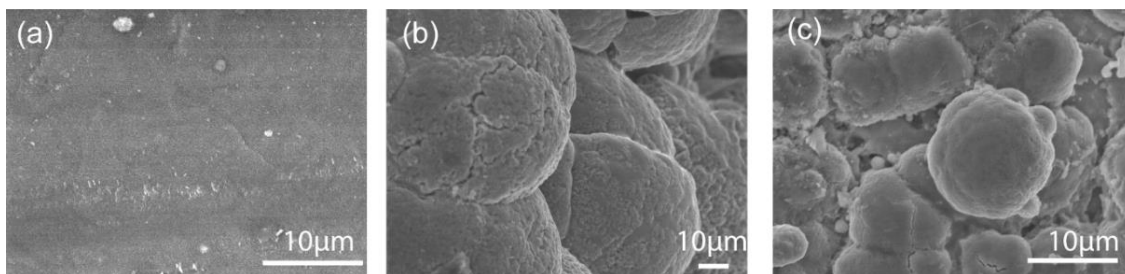


Figure 4-11. SEM images of the Mg working electrodes (in anolyte chamber). (a) Pristine Mg electrode; (b) Mg electrode after cycling in cell with bare AAO; (c) Mg electrode after cycling in cell with MOF/AAO.

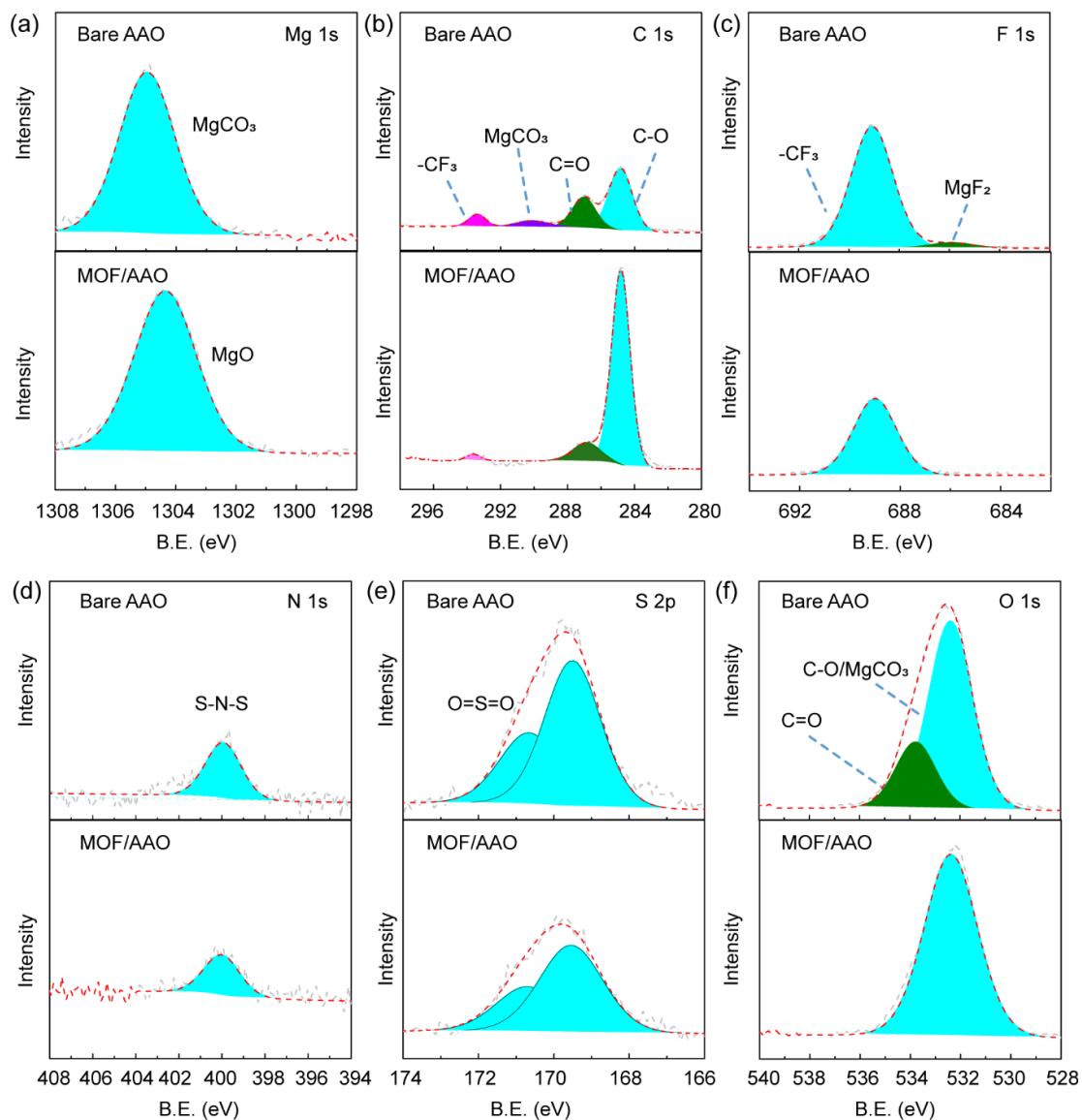


Figure 4-12. XPS spectra of cycled Mg working electrodes with bare AAO (top) and MOF/AAO (bottom). (a) Mg 1s, (b) C 1s, (c) F 1s, (d) N 1s, (e) S 2p and (f) O 1s. The cycled Mg working electrode with bare AAO separator showed contained MgCO_3 and MgF_2 components which were not shown in the spectra of cycled Mg electrode with MOF/AAO separator.

The asymmetric cell with Mg-MOF-74/AAO as separator operated for over 100 cycles with a low overpotential of <0.3 V, as shown in **Figure 4-13(a)**. This set of

experiments proved that Mg-MOF-74 as a stand-alone membrane provides adequate Mg^{2+} transport to support repeated stripping/plating of Mg in a glyme-based electrolyte system and good TFSI^- blocking capability under electrochemical conditions. It is noted that the Mg-MOF-74/AAO platform used to obtain these results can be further optimized. For instance, the overall resistance of the Mg-MOF-74/AAO membrane was higher than what one would expect from a thin Mg-MOF-74 film (for example, that shown in **Figure 4-2(a),(b)**) as shown in **Figure 4-14**. This may be due to the inadvertent penetration of Mg-MOF-74 into the pores of AAO (**Figure 4-15**). While addressing this issue is beyond the scope of this work, we envision that the deficiency could be readily corrected by using different porous substrates.

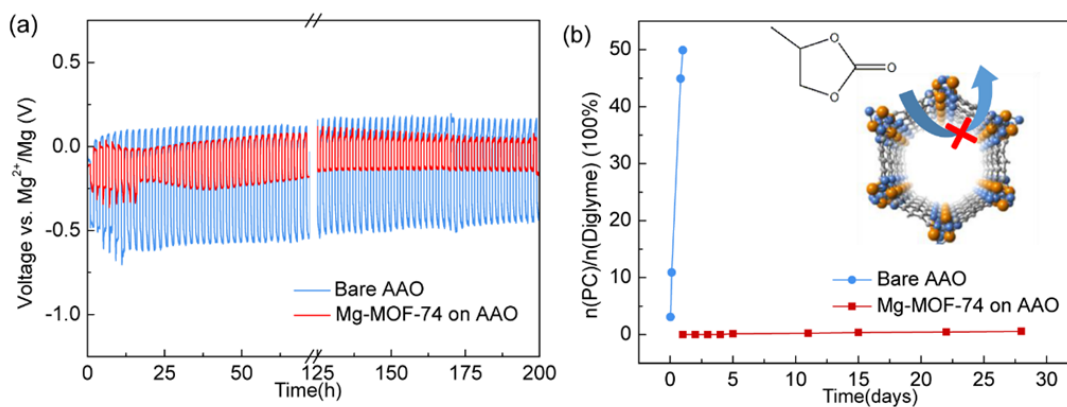


Figure 4-13. Properties of Mg-MOF-74 as a membrane in a practical electrochemical cell. (a) Electrochemical features of Mg plating/stripping in an asymmetric cell (see main text for details of the experimental conditions). Current density: $0.05\text{mA}/\text{cm}^2$. Each plating/stripping cycle lasted 2 h. (b) Negligible solvent (PC) crossover was measured when Mg-MOF-74 film was used as a separator (red); the crossover was significant when bare AAO was used (blue).

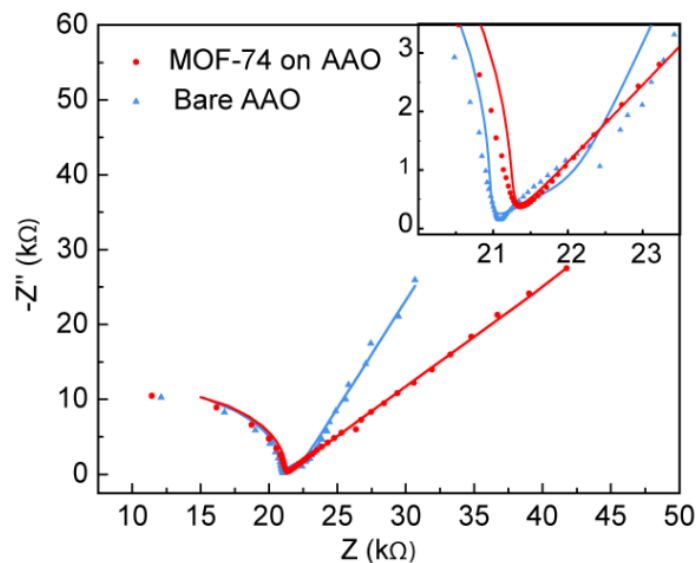


Figure 4-14. Electrochemical impedance spectra measured of MOF/AAO(red) and bare AAO (blue) with the magnified view (inset) at the high frequency end. The resistance of the MOF film grown on AAO was calculated as 327Ω , given 0.196 cm^2 of the contact area, the $64.1 \Omega \cdot \text{cm}^2$ resistance was 10 times higher than the MOF thin film grown on Au which was $6.4 \Omega \cdot \text{cm}^2$. The large resistance possibly came from the penetration of MOF into the pores of AAO which increased the overall film thickness.

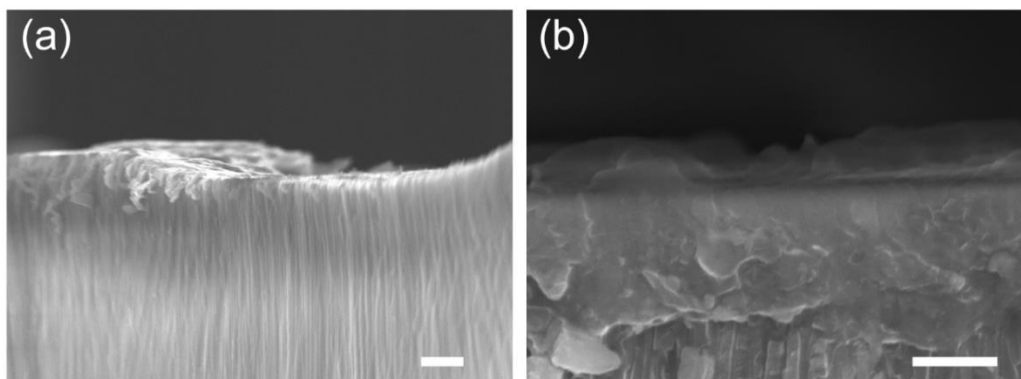


Figure 4-15. (a) Cross-sectional SEM images of bare AAO and (b)Mg-MOF-74 coated AAO. Scale bars: $1 \mu\text{m}$.

Next, we tested the capability of the Mg-MOF-74 thin film in blocking the two key species in a mixed-electrolyte battery system, namely the counter ions and the solvent molecules. Such a selectivity is critically important, especially for reduction-vulnerable compounds that are used to support the cathode chemistry but are not compatible with Mg (for example, TFSI⁻ or ClO₄⁻). To verify the solvent/ion blocking capability of the Mg-MOF-74 film, reduction-vulnerable electrolyte with 0.1 m Mg(TFSI)₂ in propylene carbonate (PC)⁵ was placed on one side of the Mg-MOF-74/AAO separator in an H-cell with an anode-compatible solvent, pure bis(2-methoxyethyl) ether (diglyme), on the other side. The amount of solvent (PC and Diglyme)/TFSI⁻ passing through Mg-MOF-74/AAO on both sides was measured by nuclear magnetic resonance (NMR) spectroscopy. As shown in **Figure 4-13 (b)**, the Mg-MOF-74/AAO separator blocked PC for 4 days with no PC signal detected in ¹H NMR spectra on the diglyme side; the mol ratio of PC to diglyme was 0.58 % after 28 days. By comparison, the ¹H NMR signal of PC was detected after only 30 min when bare AAO was used as the separator (**Figure 4-16(a)**), and the mol ratio of PC to diglyme quickly reached 50 % within 24 h. The TFSI⁻ anion blocking capability is shown in **Figure 4-16**, as well, where the ¹⁹F NMR data showed no detectable signals owing to TFSI⁻ for up to 28 days. Similar blocking capability for diglyme was also observed (**Figure 4-17 & 4-18**). It is surprising that the MOF-74 can block solvent and anions while allowing the transport of large size molecules, ferrocene. One possible explanation is that the abundant open metal sites could potentially play an important role, as they are able to bind to the Lewis basic sites on the solvent and anions, limiting their mobility.

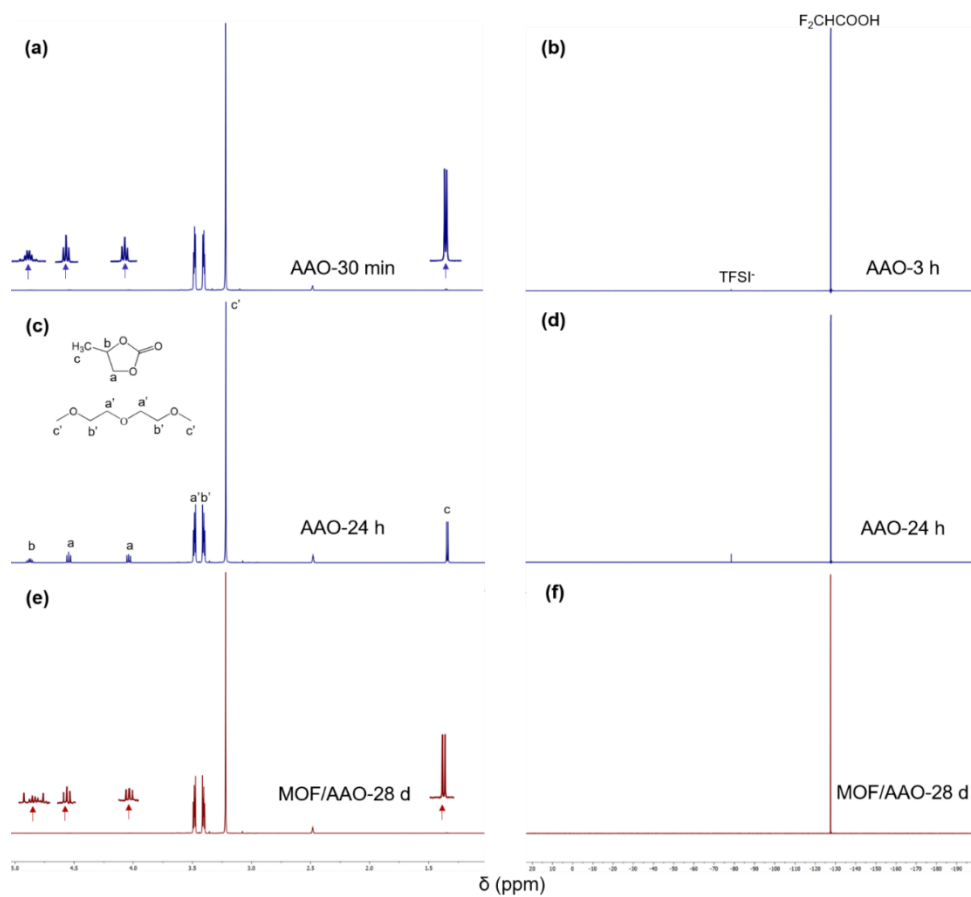


Figure 4-16. Selected regions of ^1H NMR (left side) and ^{19}F NMR (right side) spectra for the PC/TFSI $^-$ selectivity measurements of bare AAO (blue) and Mg-MOF-74/AAO (red) at (a), 30 min, (b), 3 h, (c) & (d), 24 h, and (e) & (f), 28 d.

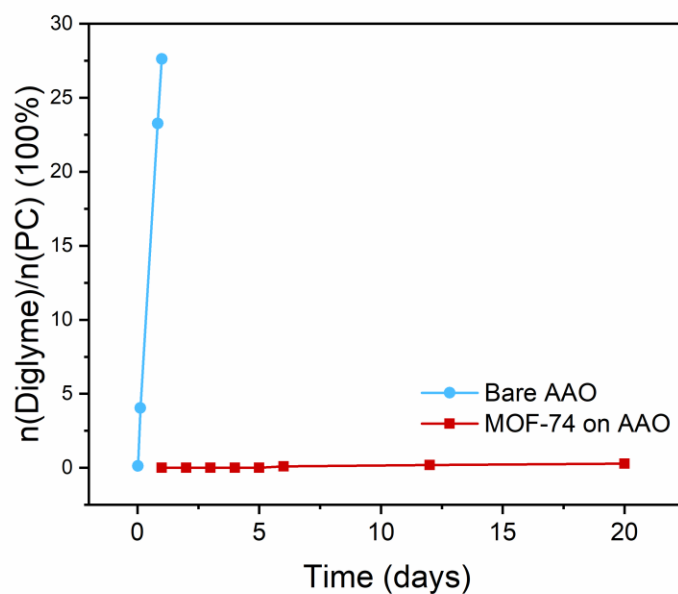


Figure 4-17. Blocking capability measurements for diglyme with bare AAO (blue line) and MOF-74 on AAO (red line) as separators in H-cell. Diglyme could be completely blocked by MOF-74 within 5 days. The mole ratio of diglyme to PC was only 0.27% after 20 days. As a sharp contrast, the mole ratio of diglyme to PC reached 28% within one day.

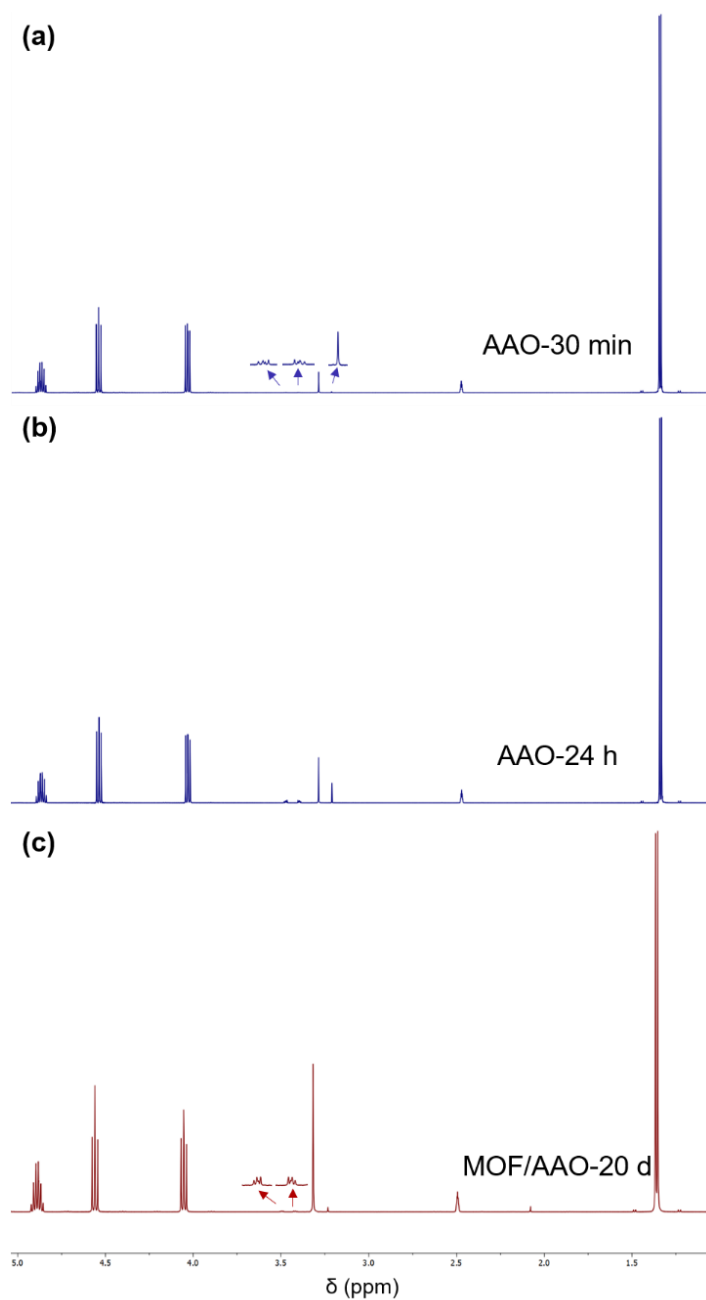


Figure 4-18. Selected regions of ^1H NMR spectra for the diglyme selectivity measurements of bare AAO (blue) and Mg-MOF-74/AAO (red) at (a), 30 min, (b), 3 h, (c) & (d), 24 h, and (e) & (f), 28 d.

4.3 Conclusion

In summary, we have demonstrated that Mg-MOF-74 thin films can be readily synthesized on different supports for selective Mg^{2+} transport. The thin film was confirmed to be electronically insulating but facile in allowing for Mg^{2+} transport. When directly grown on a Au blocking electrode, a room-temperature resistance of $6.4 \Omega \text{ cm}^2$ and an ionic conductivity of $3.17 \times 10^{-6} \text{ S cm}^{-1}$ were measured. When loaded onto an AAO support, the MOF/AAO could be used as a stand-alone membrane for electrochemical Mg stripping and plating in an asymmetric cell configuration. Successful cycling of over 100 cycles with a low overpotential ($<0.3 \text{ V}$) at a current density of 0.05 mA cm^{-2} was obtained. Control experiments proved that the Mg-MOF-74 thin films were effective in blocking the solvents (for example, PC) and the anions (for example, TFSI^-) from crossing over between the anolyte and the catholyte. Taken as a whole, this is a promising material for Mg-battery operations where incompatible chemicals are employed for the anode and chemical chemistries is demonstrated.

4.4 References

- (1) a) C. Ling, D. Banerjee, M. Matsui, *Electrochim. Acta* **2012**, *76*, 270-274; b) M. Matsui, *J. Power Sources* **2011**, *196*, 7048-7055; c) H. D. Yoo, I. Shterenberg, Y. Gofer, G. Gershinsky, N. Pour, D. Aurbach, *Energy Environ. Sci.* **2013**, *6*, 2265-2279.
- (2) a) H. D. Yoo, Y. Liang, H. Dong, J. Lin, H. Wang, Y. Liu, L. Ma, T. Wu, Y. Li, Q. Ru, Y. Jing, Q. An, W. Zhou, J. Guo, J. Lu, S. T. Pantelides, X. Qian, Y. Yao, *Nat. Commun.* **2017**, *8*, 339; b) T. Gao, S. Hou, F. Wang, Z. Ma, X. Li, K. Xu, C. Wang,

- Angew. Chem. Int. Ed.* **2017**, *129*, 13711-13715; c) X. Yao, J. Luo, Q. Dong, D. Wang, *Nano Energy* **2016**, *28*, 440-446; d) H. Tian, T. Gao, X. Li, X. Wang, C. Luo, X. Fan, C. Yang, L. Suo, Z. Ma, W. Han, C. Wang, *Nat. Commun.* **2017**, *8*, 14083; e) Q. Dong, X. Yao, J. Luo, X. Zhang, H. Hwang, D. Wang, *Chem. Commun.* **2016**, *52*, 13753-13756.
- (3) a) H. S. Kim, T. S. Arthur, G. D. Allred, J. Zajicek, J. G. Newman, A. E. Rodnyansky, A. G. Oliver, W. C. Boggess, J. Muldoon, *Nat Commun* **2011**, *2*, 427; b) J. Song, E. Sahadeo, M. Noked, S. B. Lee, *J Phys Chem Lett* **2016**, *7*, 1736-1749.
- (4) S.-Y. Ha, Y.-W. Lee, S. W. Woo, B. Koo, J.-S. Kim, J. Cho, K. T. Lee, N.-S. Choi, *ACS Appl. Mater. Interfaces* **2014**, *6*, 4063-4073.
- (5) S.-B. Son, T. Gao, S. P. Harvey, K. X. Steirer, A. Stokes, A. Norman, C. Wang, A. Cresce, K. Xu, C. Ban, *Nat. Chem.* **2018**, *10*, 532-539.
- (6) I. Shterenberg, M. Salama, H. D. Yoo, Y. Gofer, J.-B. Park, Y.-K. Sun, D. Aurbach, *J. Electrochem. Soc.* **2015**, *162*, A7118-A7128.
- (7) R. E. Doe, R. Han, J. Hwang, A. J. Gmitter, I. Shterenberg, H. D. Yoo, N. Pour, D. Aurbach, *Chem. Commun.* **2014**, *50*, 243-245.
- (8) C. Liao, N. Sa, B. Key, A. K. Burrell, L. Cheng, L. A. Curtiss, J. T. Vaughey, J.-J. Woo, L. Hu, B. Pan, Z. Zhang, *J. Mater. Chem. A* **2015**, *3*, 6082-6087.
- (9) a) S. Ikeda, M. Takahashi, J. Ishikawa, K. Ito, *Solid State Ionics* **1987**, *23*, 125-129; b) S. Higashi, K. Miwa, M. Aoki, K. Takechi, *Chem. Commun.* **2014**, *50*, 1320-1322; c) E. Roedern, R.-S. Kühnel, A. Remhof, C. Battaglia, *Sci. Rep.* **2017**, *7*, 46189.
- (10) M. Sundar, S. Selladurai, *Ionics* **2006**, *12*, 281-286.
- (11) F. Jeschull, M. J. Lacey, D. Brandell, *Electrochim. Acta* **2015**, *175*, 141-150.
- (12) J. L. C. Rowsell, O. M. Yaghi, *Microporous Mesoporous Mat.* **2004**, *73*, 3-14.
- (13) a) H. Furukawa, K. E. Cordova, M. O’Keeffe, O. M. Yaghi, *Science* **2013**, *341*, 1230444; b) S. Horike, D. Umeyama, S. Kitagawa, *Acc. Chem. Res.* **2013**, *46*, 2376-2384.
- (14) S. Wang, M. Wahiduzzaman, L. Davis, A. Tissot, W. Shepard, J. Marrot, C. Martineau-Corcus, D. Hamdane, G. Maurin, S. Devautour-Vinot, C. Serre, *Nat. Commun.* **2018**, *9*, 4937.
- (15) a) B. M. Wiers, M.-L. Foo, N. P. Balsara, J. R. Long, *J. Am. Chem. Soc.* **2011**, *133*, 14522-14525; b) L. Shen, H. B. Wu, F. Liu, J. L. Brosmer, G. Shen, X. Wang, J. I. Zink, Q. Xiao, M. Cai, G. Wang, Y. Lu, B. Dunn, *Adv. Mater.* **2018**, *30*, 1707476; c) E. M. Miner, S. S. Park, M. Dincă, *J. Am. Chem. Soc.* **2019**, *141*, 4422-4427; d) S. Bai, X. Liu, K. Zhu, S. Wu, H. Zhou, *Nat. Energy* **2016**, *1*, 16094; e) S. Bai, Y. Sun, J. Yi, Y. He, Y. Qiao, H. Zhou, *Joule* **2018**, *2*, 2117-2132.
- (16) R. Li, K. Li, G. Wang, L. Li, Q. Zhang, J. Yan, Y. Chen, Q. Zhang, C. Hou, Y. Li, H. Wang, *ACS Nano* **2018**, *12*, 3759-3768.
- (17) a) P. Ramaswamy, N. E. Wong, G. K. H. Shimizu, *Chem. Soc. Rev.* **2014**, *43*, 5913-5932; b) S. S. Park, Y. Tulchinsky, M. Dincă, *J. Am. Chem. Soc.* **2017**, *139*, 13260-13263.
- (18) M. L. Aubrey, R. Ameloot, B. M. Wiers, J. R. Long, *Energy Environ. Sci.* **2014**, *7*, 667-671.
- (19) a) Y. Guo, Y. Ying, Y. Mao, X. Peng, B. Chen, *Angew. Chem. Int. Ed.* **2016**, *55*, 15120-15124; b) R. Ameloot, M. Aubrey, B. M. Wiers, A. P. Gómora-Figueroa, S. N. Patel, N. P. Balsara, J. R. Long, *Chem. Eur. J.* **2013**, *19*, 5533-5536.

- (20) E. Virmani, J. M. Rotter, A. Mähringer, T. von Zons, A. Godt, T. Bein, S. Wuttke, D. D. Medina, *J. Am. Chem. Soc.* **2018**, *140*, 4812-4819.
- (21) H. Wu, W. Zhou, T. Yildirim, *J. Am. Chem. Soc.* **2009**, *131*, 4995-5000.
- (22) a) P. D. C. Dietzel, Y. Morita, R. Blom, H. Fjellvåg, *Angew. Chem. Int. Ed.* **2005**, *44*, 6354-6358; b) H. Deng, S. Grunder, K. E. Cordova, C. Valente, H. Furukawa, M. Hmadeh, F. Gándara, A. C. Whalley, Z. Liu, S. Asahina, H. Kazumori, M. O’Keeffe, O. Terasaki, J. F. Stoddart, O. M. Yaghi, *Science* **2012**, *336*, 1018-1023; c) D. Britt, H. Furukawa, B. Wang, T. G. Glover, O. M. Yaghi, *Proc. Natl. Acad. Sci. U.S.A.* **2009**, *106*, 20637-20640.
- (23) F. Buchner, in *STM investigation of molecular architectures of porphyrinoids on a Ag(111) surface: supramolecular ordering, electronic properties and reactivity*, Springer Berlin Heidelberg, Berlin, Heidelberg, **2010**, pp. 101-128.
- (24) C. E. D. Chidsey, C. R. Bertozzi, T. M. Putvinski, A. M. Mujsce, *J. Am. Chem. Soc.* **1990**, *112*, 4301-4306.
- (25) R. Mantravadi, P. R. Chinnam, D. A. Dikin, S. L. Wunder, *ACS Appl. Mater. Interfaces* **2016**, *8*, 13426-13436.
- (26) N. N. Rajput, X. Qu, N. Sa, A. K. Burrell, K. A. Persson, *J. Am. Chem. Soc.* **2015**, *137*, 3411-3420.
- (27) T. Gao, S. Hou, K. Huynh, F. Wang, N. Eidson, X. Fan, F. Han, C. Luo, M. Mao, X. Li, C. Wang, *ACS Appl. Mater. Interfaces* **2018**, *10*, 14767-14776.

Chapter 5. Summary

In summary, the thesis showed a clear path toward high energy density batteries through electrode and electrolyte design.

To enable the conversion-type O_2 cathode, we have investigated a new nitrogen-doped free-standing porous carbon material as a promising cathode material for Li- O_2 battery in the first part of this thesis. This material takes advantage of the spontaneously formed hierarchical porous structure derived from wood. The structure is expected to facilitate both mass transport and discharge product storage. Moreover, we introduced heteroatom (N) doping to further improve the catalytic activity of the carbon cathode for lower overpotential and higher capacity. We have unambiguously confirmed the initial electrochemical process to be the desired reactions of Li_2O_2 formation and decomposition. The free standing nature and mechanical strength of wood derived carbon makes it possible to eliminate the need for additional current collector and binders, improving the overall energy density and reducing possible parasitic chemical reactions. Also, the renewability of wood with this unique structure could potentially provide a cost-effective route as porous electrode for large-scale mass production.

In the second part of this thesis, we focused on the Li metal anode and came up with a strategy to resolve conflicts between the battery safety and high energy density. We demonstrated that O_2 as additives can enable Li metal anode operation in non-flammable TEP electrolyte. The significantly different cycling performance and deposited Li morphology results from the electrochemically induced chemical reaction between O_2 species and TEP solvent molecules, which leads the Li-compatible SEI formation and

effectively suppresses the TEP decomposition. When tested in a symmetric Li||Li cell, >300 cycles of repeated Li plating and stripping was achieved at a current density of 0.5 mA·cm⁻²; when tested in a Li-O₂ prototypical cell, the system showed comparable performance as in a flammable, ether-based electrolyte. Similar strategy worked equally well for Li-LFP batteries, too. The approach represents a new direction in addressing the critical safety concerns for high-capacity electrochemical energy storage technologies.

One alternative strategy to satisfy both the high energy density and the safety requirements is the utilization of dendrite-free Mg anode. In the third part of this thesis, we developed a thin film metal–organic framework (MOF) for selective Mg²⁺ transport to solve the incompatibility issues between the anode and the cathode chemistry for Mg batteries. We have demonstrated that Mg-MOF-74 thin films can be readily synthesized on different supports for selective Mg²⁺ transport. The thin film was confirmed to be electronically insulating but facile in allowing for Mg²⁺ transport. When directly grown on a Au blocking electrode, a room-temperature resistance of 6.4 Ω cm² and an ionic conductivity of 3.17×10⁻⁶ S cm⁻¹ were measured. When loaded onto an AAO support, the MOF/AAO could be used as a stand-alone membrane for electrochemical Mg stripping and plating in an asymmetric cell configuration. Successful cycling of over 100 cycles with a low overpotential (<0.3 V) at a current density of 0.05 mA cm⁻² was obtained. Control experiments proved that the Mg-MOF-74 thin films were effective in blocking the solvents (for example, PC) and the anions (for example, TFSI⁻) from crossing over between the anolyte and the catholyte. Taken as a whole, this is a promising material for Mg-battery operations where incompatible chemicals are employed for the anode and chemical chemistries is demonstrated.